

RICE UNIVERSITY

Engineered Nanomaterials for Energy Harvesting and Storage Applications

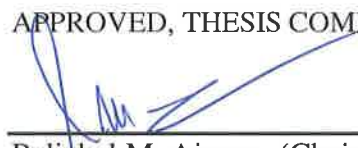
by

Hemtej Gullapalli

A THESIS SUBMITTED
IN PARTIAL FULFILLMENT OF THE
REQUIREMENTS FOR THE DEGREE

Doctor of Philosophy


APPROVED, THESIS COMMITTEE




Pulickel M. Ajayan, (Chair)
Benjamin M. and Mary Greenwood
Anderson Professor of Engineering



Robert Vajtai
Senior Faculty Fellow, Materials Science
and NanoEngineering



Sibani Lisa Biswal
Associate Professor, Chemical and
Biomolecular Engineering



Leela Mohana Reddy Arava
Assistant Professor, Mechanical Engineering
Department, Wayne State University

HOUSTON, TEXAS

August 2014

ABSTRACT

Engineered Nanomaterials for Energy Harvesting and Storage Applications

by

Hemtej Gullapalli

Energy harvesting and storage are independent mechanisms, each having their own significance in the energy cycle. Energy is generally harvested from temperature variations, mechanical vibrations and other phenomena which are inherently sporadic in nature, the harvested energy stands a better chance of efficient utilization if it can be stored and used later, depending on the demand. In essence a comprehensive device that can harness power from surrounding environment and provide a steady and reliable source of energy would be ideal. Towards realizing such a system, for the harvesting component, a piezoelectric nano-composite material consisting of ZnO nanostructures embedded into the matrix of 'Paper' has been developed. Providing a flexible backbone to a brittle material makes it a robust architecture. Energy harvesting by scavenging both mechanical and thermal fluctuations using this flexible nano-composite is discussed in this thesis. On the energy storage front, Graphene based materials developed with a focus towards realizing ultra-thin lithium ion batteries and supercapacitors are introduced. Efforts for enhancing the energy storage performance of such graphitic carbon are detailed. Increasing the rate capability by direct CVD synthesis of graphene on current collectors, enhancing its electrochemical capacity through doping and engineering 3D metallic structures to increase the areal energy density have been studied.

Acknowledgments

I would need to thank all the wonderful people who have stood with me throughout my graduate experience. As it was rather a bumpy ride, I could not have achieved my goals without all the helping hands. I would first like to thank Prof. Ajayan for his trust in me and for giving me this great opportunity. The freedom he has given me to explore my ideas (sometimes crazy ones) and also guiding me when I am doing so, has been the best part of my experience. The motivation he gives to try and solve the unknown challenges is truly inspirational. I have learnt a lot under his guidance, both personally and professionally, which I believe is the essence of being a doctorate. He has helped me through several difficult periods over my studies at Rice, and he was very considerate, for which I remain extremely grateful to him.

A special thanks goes to all the mentors who have guided me through my research. Leela has been a good friend and a wonderful guide. He shares a part of my success, and my humble gratitude to him. Dr. Ashvani Kumar needs to be thanked for training me on the science of piezoelectric engineering. I thank Dr. Robert Vajtai for all the guidance, discussions and his trust. Dr. Anchal Srivastava has been very patient in teaching me the CVD process for graphene growth. I am thankful to Prof. Satish Nagarajaiah for the guidance and support he had given me during several collaborative endeavors. I am also thankful to Prof. Sibani Lisa Biswal for agreeing to review my work and serve on the thesis committee.

My friends in the lab had made my experience a truly enjoyable one. The collaborative environment in the lab was very productive and a substantial part of my learning was

during the coffee breaks we had. Special thanks to Sanketh, Vishnu, Charu, Marco and Kaushik for working with me on several parts of my research. My thanks also goes to all the undergrads who have assisted me at several phases. I would also like to thank Dr. Shaijumon Manikoth, Dr. Kaushik Balakrishnan, Dr. Antony George and other current and past postdocs for all the great advices they have given me.

I would like to thank all the administrative staff of the mechanical engineering and material science department and the personal of Shared Equipment Authority for all the help they have given me. I would also need to thank Advanced Energy Consortium (AEC) and Rice University Scholarship Program for their financial support.

Finally, I would like to mention the biggest strength I have, my family. I would need to credit my success to my mother and father, for believing that I could do it, and supporting me all the while. My brothers had taken up a lot of responsibility, so I can chase my dreams and Rudra had made sure the smiles aren't faded. My wonderful wife, Radhika, has been my strength all along. She had been very patient and gave the motivation I needed many a times, I thank her for her confidence in me. You wonderful people made the effort painless.

Dedicated to Dad, he would have been very proud today.

Contents

Acknowledgments	iii
Contents	v
List of Figures.....	vii
Introduction.....	1
1.1. Material choice for Energy Harvesting	5
1.2. Energy storage mechanisms	9
1.2.1. Lithium ion batteries	10
1.2.2. Supercapacitors	15
1.2.3. Graphene - a new frontier carbon material	17
1.3. Scope of thesis.....	20
Developing flexible piezoelectric composite material	22
2.1. Fabrication of ZnO-paper composite	23
2.2. Characterization of ZnO-paper composite	25
2.3. Mechanical energy harvesting.....	32
2.3.1. Experimental details	33
2.3.2. Results and discussion	37
2.4. Thermal energy harvesting	39
2.4.1. Experimental details	39
2.4.2. Results and discussion	40
2.5. Strain Sensor for structural health monitoring	44
2.5.1. Experimental details	45
2.5.2. Results and discussion	47
2.6. Conclusions	53
Direct synthesis of graphene on metallic substrates	54
3.1. General Experimental Setup.....	59
3.2. Graphene growth on copper substrates using liquid precursor	65
3.2.1. Fabrication procedure	65
3.2.2. Characterization	66
3.3. Nitrogen doped Graphene on copper substrates	69

3.3.1. Fabrication procedure	69
3.3.2. Characterization	71
3.4. Graphene growth on stainless steel substrates	75
3.4.1. Fabrication procedure	79
3.4.2. Characterization	80
3.5. Direct synthesis of Graphene covered 3D metallic substrates	87
3.5.1. Fabrication procedure	87
3.5.2. Characterization	89
3.6. Conclusions	98
Graphene as a material of use in ultrathin energy storage devices.....	100
Interfacial resistance issue.....	101
Specific energy density issue	101
Areal energy enhancement issue.....	102
4.1. Lithium ion battery applications	104
4.1.1. Cell fabrication	104
4.1.2. Electrochemical properties of graphene grown on planar current collectors	104
4.1.3. Effect of nitrogen doping on the electrochemical properties of graphene.....	108
4.1.4. Graphene on 3D metallic substrates as anodes for Li-ion battery	111
4.1.5. 3D metallic substrates as current collectors for Li-ion.....	113
Deposition and Characterization of SiN _x	113
Electrochemical performance of SiN _x	117
4.2. Supercapacitor behavior of graphene based structures	119
4.3. Energy storage-Harvester integration.....	121
4.3.1. Design of experimental setup	122
4.3.2. Results and discussion	124
4.4. Conclusions	125
Summary.....	127
References.....	130

List of Figures

Figure 1-1: Schematic of the charge and discharge mechanisms in a lithium ion battery (adapted from ref [92])	11
Figure 1-2: (a) Storage mechanisms of Li ions in graphite. (b) Li storage in form of Li_2 covalent molecules¹⁰³ (c) Schematic model of Li storage in cavities and nano pores¹⁰⁴ (d) Dahn's model of Li adsorption on the two sides of an isolated graphene sheet¹⁰⁶. (Adapted from [101]).....	14
Figure 1-3: Schematic of the mechanism of charge and discharge in an EDLC showing the charge separation and recombination during charging and discharging process leading to the formation of double layer at the electrode.....	16
Figure 1-4: Structure of a 2D layer of graphene and depiction of molding it into 0-D Buckyball, 1-D CNT and 3-D graphite forms. (Adapted from ref [121])	18
Figure 2-1: Photographs of the ZnO-paper composite with gold coated on the surface	25
Figure 2-2: Scanning electron micrographs showing the structure of plain filter paper. Cellulose fibers are intermingled to form a porous network.....	26
Figure 2-3: (a-c) Scanning electron micrographs of ZnO-paper composite. (d) Schematic depicting the structure	27
Figure 2-4: Energy dispersive X-ray analysis used to detect the elemental composition of the surface of ZnO-paper	29
Figure 2-5: X-ray diffraction spectrum of the Zn-Paper composite. The peak position closely match with the wurtzite structure of ZnO.....	30
Figure 2-6: Transmission electron micrograph of a single ZnO nanorod extracted from the ZnO-paper composite. Highly uniform crystallinity is observed and confirmed with the diffraction pattern in the inset.....	31
Figure 2-7: Thermogravimetric analysis plots showing the weight loss of (A) plain filer paper and (B) ZnO-paper composite as they are heated in air. Comparing the trend, it can be deduced that the ZnO-paper has a 35% by weight of ZnO in it.....	32
Figure 2-8: Photograph of a device made of ZnO-paper composite. Schematic describes the cross section of the structure.....	34

Figure 2-9: Photographs of devices with interconnected ZnO-Paper patches. (a) 10 in series (b) 4 in parallel	35
Figure 2-10: Schematic depicting a (a) polycrystalline material with random dipole polarization (b) Polling with an external voltage bias (c) aligned polarity.....	36
Figure 2-11: Energy harvested from the ZnO-paper device. (a) Current output when one device (0.5cmX0.5cm) is vibrated (b) Output when terminals reversed (c) Current output with 4 patches in parallel (d) Voltage output with 4 devices in series	38
Figure 2-12: Plots of thermal energy harvested with the ZnO-paper device. (a) Current output as a result of repetitive heating cycles (b) Output when terminals are reversed (c & d) Voltage output of the same device.....	41
Figure 2-13: Current output of 4 cm² and 9 cm² size devices on thermal cycling	42
Figure 2-14: Voltage output from a device with 1cm² active material patch, subjected to a continuous thermal heating for 30 minutes	44
Figure 2-15: Schematic of test device for measuring strain experienced by a metal beam. (B) Photograph of the test setup to measure static strain loading	46
Figure 2-16: (A) I-V characteristic of the ZnO-paper sensor as a function of strain. (B) Response to tensile loading (C) Response to cyclic loading in which a load is cycled equally from compression to tension.	49
Figure 2-17: Response of the sensor as it is subjected to various static loads continuously.....	50
Figure 2-18: (a) Schematic diagram depicting the experimental setup for strain measurement under dynamic loading. (b-f) Dynamic response of the composite sensor on exciting the beam with frequencies (b) 0.1, (c) 2, (d & f) 2, and (e) 4 Hz..	52
Figure 3-1: Phase diagrams of (a) Nickel-Carbon system (b) Copper-Carbon system. Adapted from ref [165].....	56
Figure 3-2: Schematic diagrams of the distribution of Carbon isotopes based on different growth mechanisms (a) on nickel (b) on copper (adapted from ref [172])	58
Figure 3-3: (a)Photograph of the Chemical Vapor deposition setup. (b) Photographh of the tubing at the inlet side, multiple inputs can be independently controlled with the valves.....	61

Figure 3-4: Schematic blueprint of the chemical vapor deposition setup, equipped with a vacuum feature and has both liquid and gaseous inputs	62
Figure 3-5: Recipe for graphene growth on copper substrates. 4 minutes of hexane exposure at 950°C results in one layer graphene, while 8 minutes yields 2 to 3 layers	66
Figure 3-6: Schematic sketch of polymer liftoff technique used to transfer graphene from metallic substrates onto other substrates	68
Figure 3-7: Raman spectra of graphene grown on copper foils with Hexane vapors as the precursor using CVD technique	69
Figure 3-8: Recipe for nitrogen doped graphene growth on copper substrates. Ammonia is flown while cooling the chamber	71
Figure 3-9: Transmission electron micrograph image of a nitrogen doped graphene with 3 layers. The layers can be distinguished at the edge of the sample.	72
Figure 3-10: Raman spectra of nitrogen doped graphene. 4minutes growth yields 1 to 2 layers while 8minutes results in 2 to 3 layers	73
Figure 3-11: (a) Survey analysis of Nitrogen doped graphene, quantifying the chemical composition using X-ray photoemission spectroscopy (XPS) technique. (b) Higher resolution scan of carbon peak, with deconvoluted components. (c) Higher resolution scan of Nitrogen peak, with deconvoluted components (d) Schematic rebuild of the presumed structure as evident from the XPS results	75
Figure 3-12: Solubility of carbon in chromium-nickel austenite according to various investigators. (adapted from [182])	78
Figure 3-13: Recipe for graphene growth on 304 grade Stainless Steel substrates. The number of layers formed is dependent on the cooling rate	80
Figure 3-14: (a) Scanning electron micrograph of the surface of stainless steel foil. (b-d) various magnification images of the surface after graphene growth. A thin layer with wrinkles and grain boundaries can be clearly seen to blanket the metal.	82
Figure 3-15: (a and b) Transmission electron micrograph images of the 3 layered graphene grown on stainless steel substrates. (c) Diffraction pattern of the sample confirming the crystalline structure of graphene	83

Figure 3-16: Raman spectra of graphene grown on stainless steel substrates. The cooling rate dictates the number of layers that form on the surface. While a quenching the sample results in the carbon being locked in the lattice, controlled cooling would allow carbon precipitation and graphitize on the surface 85

Figure 3-17: Raman spectra of two samples with similar cooling rates, one with very long, 40 minute exposure to Hexane vapors during the growth process at 950°C and the other with 3 minutes exposure. The duration of carbon exposure does not define the number of layers formed in case of stainless steel substrates 86

Figure 3-18: Recipe for synthesis of graphene covered 3D etched metallic structures. Care is taken not to mix PFH vapors with hydrogen at high temperatures 89

Figure 3-19: schematic representation of the mechanism of formation of 3D patterns on metallic substrate. Fluorine ions in pyrolyzed PFH are responsible for etching while carbon atoms form graphene on the surface 91

Figure 3-20: Porous copper with graphene coating formed by CVD using PFH as the precursor 92

Figure 3-21: Raman spectra of graphene covered 3D copper substrate 93

Figure 3-22: X-ray photoemission spectroscopy analysis of the surface of 3D copper substrate 93

Figure 3-23: Scanning electron micrograph images of interlinked copper particles, formed as a byproduct while synthesizing 3D copper structures 95

Figure 3-24: Scanning electron micrographs of 3D porous stainless steel foils. (a-c) Surface profile (d) magnification of single pore with graphene visible on the surface (e) sample viewed at an angle (f) cross section of a cracked sample, the porous nature is observed until a depth of ~10 μm 97

Figure 3-25: Raman spectra of graphene on 3D stainless steel compared to that of graphene on planar stainless steel 98

Figure 4-1: (A) Charge discharge profiles of graphene directly grown on stainless steel substrates (B) Discharge capacity of the cell observed over a number of cycles 106

Figure 4-2: Rate capability studies of graphene on stainless steel 107

Figure 4-3: (A) Comparison of discharge capacities of nitrogen doped graphene and pristine graphene, directly grown on copper foils. (B) High rate capability test for Nitrogen doped graphene..... 110

Figure 4-4: (A) Rate-capability studies of graphene covered porous SS substrates. (B) Discharge capacity versus cycle number for various current rates. Good capacity retention is observed for high current rates and the nominal capacity is regained upon returning to lower current rates. 112

Figure 4-5: Scanning electron micrographs of SiN_x deposited (A,B) onto Planar stainless steel{an area scraped to identify the layer} (C-F) onto 3D stainless steel substrates 115

Figure 4-6: X-Ray Photoemission spectroscopy analysis of the SiN_x deposited onto the 3D stainless steel substrate. (A) Survey analysis with the major peaks labeled, atomic concentrations in the inset (B) Elemental analysis of Silicon, with the peak deconvoluted..... 116

Figure 4-7: (A) Charge discharge profiles of the SiN_x electrode on 3D stainless steel. (B) Comparison of discharge capacities of SiN_x deposited onto 3D stainless steel substrates and planar stainless steel..... 118

Figure 4-8: Cyclic voltammetry plots of supercapacitors fabricated out of graphene coated 2D and 3D stainless steel substrates. The capacitors were tested at different scan rates and at room temperature and 120 °C..... 120

Figure 4-9: (A) Schematic of experimental setup for testing the integration of harvesting and storage units. (B) Photograph of the setup 123

Figure 4-10: Voltage profile across the supercapacitor while charging it using the energy generated from the harvester, at various temperatures. The capacitor has a self-discharge mechanism once the vibration is turned off..... 125

Chapter 1

Introduction

Energy conversion from one form to the other has been one of the prime distinctive achievements of human race. With an ever increasing dependence on energy, the quest has always been to harvest it from reliable sources and store it until being used. Pioneering both these mechanisms has been evolutionary and has always been followed from the Stone Age to the Electronic Age.

Recent advancements in portable electronics have put up a demand for portable and reliable energy sources. With the electronic components shrinking by the day, low powered portable systems have been designed for various applications and have reached to the stage of micron scale. However, the advancement in energy storage technology is not as steep as compared to that of electronics. Today, bulk of the weight and volume in any commercial electronics device, from cellphones to hybrid cars is occupied by the battery that powers it. A US soldier in combat would carry about 45 pounds of batteries to power various devices such as communication electronics, night vision equipment,

computing equipment, ammunition etc., which adds to the other required load of about 100 pounds.¹ In today's technology driven battle field, power for a soldier has become as critical as ammunition and food. Carrying such heavy load not only limits their mobility in the battle field but also leads to long term muscular injuries. While there is no available mechanism to charge a battery when in the field, soldiers are often required to carry primary non rechargeable batteries with long lifetime. During a state of war, this also adds to the logistics issues as battery stockpiles should be sufficiently maintained and supplied. An article published in the national defense magazine² gives a glimpse of the challenges faced by the army during the Iraq war. The author reveals that battery supplies had reached a dangerously low level during the war and could have been exhausted if the war lasted a few weeks more. Also difficulty in supplying these batteries to the soldiers in the frontline on a regular basis was challenging.

On parallel lines, implantable medical devices and biomedical sensors have already shrunk in size while being more advanced and sophisticated. Most of these wireless devices are again limited by the energy source they carry. Many other applications from down-hole oil field sensors, to environmental and chemical sensors, have the need for wireless micro devices, limited by the size of the net device. Many an instant, it is not very practical or economical to replace the batteries in these kinds of devices. For example, changing batteries in a pacemaker would add to the patient discomfort, while changing a battery in a down-hole oil drilling equipment would incur huge operating costs. And in some applications such as micro devices, existing battery technologies at the miniature size scale cannot meet the energy demands for a prolonged duration, To solve this energy bottleneck, the quest has been to develop autonomous

energy sources, one that can provide uninterrupted energy without the need for physical intervention. This is envisioned to use locally available sources rather than transporting energy to the device. To realize such a system, the device would need to first convert the locally available energy into a usable form and store it in a reservoir for later use.

Towards building one such product, Kyminsis et al. (1998)³ have built an integrated power harvesting-storage component that has been integrated into the insole of a shoe, to parasitically tap the energy from its bending while the user walks. A concept of building the piezoelectric component in a unimorph design was introduced, by making a somewhat bent PZT crystal. To store the energy generated from the harvester, a commercial 47 mF electrolytic capacitor was used. Army research labs (ARL) has explored the usability of this concept for use by soldiers, but have lately stopped the project.⁴ Though an important concept of powering wearable electronics by human motion, certain caveats exist in this technology. One deterrent is the load it creates on the user as the weight and rigidity of the device results in user discomfort. Also, a bendable form of piezoelectric material is required and the crystal has to withstand the stress created by the weight of the user. A crack in this crystal would make the device incapable.

Integrated energy harvesters have also been the focus of interest for implantable medical devices. This area has been more critical than others, owing to the sensitivity of the usage. While a number of medical implants such as pacemakers, defibrillator, neural stimulators, and lab on a chip monitors & sensors have been developed, most of them being battery powered are dependent on its performance. The concept of using the natural processes in the human body to power these devices is an attractive option, and adds to

the reliability of such implants. Many research reports made progress in this direction, and have used both involuntary motions of the internal organs and the physical motion of the patient to harvest and power devices.⁵⁻⁹ Recently, Dagdeviren et al. (2014)¹⁰ have developed an efficient piezoelectric harvesting device, made out of a flexible design of PZT coated into a mesh like pattern. A complete system consisting of rectifiers and a micro battery has been built and its capability of harvesting energy from the natural contraction and relaxation motions of the heart, lung, and diaphragm has been demonstrated. This work stands the latest of a series of numerous similar efforts reported earlier.¹¹⁻¹⁵ Most of these works call for the piezoelectric material to be flexible. Having a flexible nature reduces the stress required to deform it and thereby reduces the encumbrance it has on the host. Also such implantable devices have serious size and weight limitations and hence micro scale engineering is required for their fabrication.

Another application of uninterrupted energy sources is in developing wireless micro sensor technologies. With the trend of electronics becoming smaller and energy efficient by the day, it has been envisioned that micro devices will soon find their place in areas such as targeted drug delivery,¹⁶⁻²⁰ sensors for oil and gas reservoir characterization,²¹⁻²⁵ geological surveys using micro swarms, environmental, chemical and biological detection. etc.²⁶⁻²⁸ Micro sensors are usually dormant for long periods of time until when a measurement is needed which is usually transient in nature. In such cases, the size of the energy storage device and its survival in harsh environmental conditions for extended periods of time is critical.

In every context of developing an autonomous energy source, the common characteristics to incorporate includes, a rather flexible and light weight nature for the

harvesting unit so as not to overload the host structure and a highly efficient energy storage unit that can be coupled to this harvester without overloading it in terms of space, weight and electronics. Though the field of developing autonomous energy sources has seen many revolutionary achievements, there is still a quest for materials that can design such a system effectively. A flexible, robust and efficient energy harvester that can also be made in an economical and scalable method is the need of the hour. Though many energy storage technologies are being developed with great success, to meet the energy compliance of micro scale autonomy, an ultralight and miniaturized device, yet capable of withstanding the rigorous atmospheric conditions is still in need. Material configurations hold the key for building such a tailored system.

1.1. Material choice for Energy Harvesting

Towards optimizing the concept of energy scavenging, cheap and reliable harvesters are needed. While many forms of stray energy sources exist, mechanical and thermal energies are the most common ones, and can be found in conditions where other efficient forms (example solar) cease to exist. Scavenging these two common energy forms has attained much research attention over the last decade.²⁹⁻³⁸

Converting mechanical energy into electrical charge can be achieved by either of three mechanisms, electrostatic,³⁹⁻⁴⁴ electromagnetic⁴⁵⁻⁵⁰ and piezoelectric.⁵¹⁻⁵⁴ Electrostatic mechanism uses a variable capacitor structure to generate charges from a relative motion between two plates, while electromagnetic devices are based on electromagnetic induction and ruled by Lenz's law. An electromotive force is generated from a relative motion between a coil and a magnet. Harvesting at the micro scale

involves Micro Electromechanical devices employing cantilever beam mechanisms which result in efficiency loss. Piezoelectric phenomenon is rather a straight forward one and involves special class of materials to achieve this.

In case of thermal energy, two forms of thermal excitations exist, one is the temperature gradient which can be tapped using the thermoelectric effect while the other is the fluctuations in temperature over time, harvested by a concept called the pyroelectric effect, also a material property of certain subclass of piezoelectric materials.⁵⁵

Piezoelectric materials are a set of crystalline materials, with a non-centrosymmetric crystal structure. Of all the 32 existing crystal classes, 21 lack center of symmetry and of which 20 are classified as piezoelectric in nature. When the piezoelectric crystal is mechanically strained, or when the crystal is deformed by the application of an external stress, electric charges appear on the crystal surfaces. Of these crystals, 10 crystal classes are polar in nature, i.e. they have a dipole in their crystal structure. These polar crystals exhibit pyroelectric behavior, meaning, the dipoles can be polarized and surface charges are created by thermal excitation. Of these pyroelectric materials are yet another subgroup of materials called the ferroelectrics which exhibit spontaneous polarization meaning the dipoles can be reoriented with an external electric field.^{56,57}

Though numerous materials fall under these crystal categories and in theory are piezoelectric in nature, only a few exhibit enhanced effects, useful for practical applications. The efficiency of a crystal to convert mechanical energy into electrical is

gauged by its piezoelectric constant. Both naturally occurring and manmade chemical structures have been shown to have substantial piezoelectric nature.⁵⁸

The piezoelectric effect of materials has been extensively used for sensor applications and found their place in devices such as microphones, accelerometers and sensors.⁵⁹⁻⁶⁴ Active energy harvesting from such materials has also been extensively studied and documented. Sodano and co-others have reported a series of reviews of the various significant contributions in the field.^{65,66} Several types of piezoelectric materials ranging from ceramics to polymers have already been shown to harvest multiple forms of energy such as thermal and mechanical.⁶⁷⁻⁷⁰ However the most efficient piezoelectric materials are ceramics and hence brittle in nature. Lack of structural stability and abuse tolerance hinders their performance.⁷¹⁻⁷⁵ To overcome this, composites of piezoelectric materials have also been explored in which the brittle materials are pooled to the mechanical compliance and flexibility of polymers. Furukawa et al.(1979)⁷⁶ have proposed early in the field, a series of composite systems consisting of PZT ceramics combined with various polymers. The piezoelectric activity of the composites was tested and documented. This concept though introduces a sense of robustness to the system, lacks efficiency as the energy transfer between the two constituents of the composite is not ideal.

Energy harvesting at small scales has also been taken up and has gained momentum in the last decade with the technological advancements seen in the field of nanotechnology. Particular mention would need to be given to the series of works done by Wang et al. group at Georgia tech institute.⁷⁷⁻⁸⁶ A report by Wang and Song (2006)⁸⁷ introduced the concept of nano-generator, where in they fabricated vertically aligned zinc

oxide (piezoelectric in nature) nanorods on various substrates using a vapor-liquid-solid process. These rods when deflected by a gold coated AFM tip would generate voltage which could be used to power nano devices. The interesting aspect of this work is the direct current output observed from the device. This is explained to be a result of the Schottky contact between the semiconductor ZnO and the gold coating on the AFM tip. This essentially eliminates the need of a rectifier circuit needed to smooth the bipolar output observed in a vibrational harvesting system. Extrapolating this novel concept, the research group went on to build various other configurations and devices, gearing towards realizing more practical designs. Of the several other reports branched out of this work, Yang et al. (2009)⁸⁴ and Zhu et al. (2010)⁸⁵ have increased the performance and introduced flexibility to the system by designing a laterally oriented ZnO rod array on a polymer substrate. Dong et al (2012)⁸⁶ went ahead and integrated it with a graphene based supercapacitor. Though this technology and others have set benchmarks for developing energy harvesting systems at the micro scale, they involve high level of complexity in making such devices. Synthesis of nanorods and positioning them in a patterned format using micromanipulators is a complex task, adding to the cost, effort and effectiveness. The structural integrity of devices with such microstructures is hard to stabilize and therefore scalability remains a factor.

Although these reports have made significant contributions and set benchmarks in the field of energy harvesting using nanoengineered materials, it is important to explore innovative, inexpensive, scalable technologies based on new materials and engineering approaches wherein a single device can be used to transform multiple sources of energy

1.2. Energy storage mechanisms

Energy storage would need to complement the energy harvesting component in the best way possible to avoid losses and capacity mismatch. As energy harvesting is often taken up in harsh environmental conditions, the storage component would need to withstand these conditions without losing its performance. For example, while harvesting thermal energy, the storage reservoir would need to be stable at high temperatures. Hence, in order to support the envisioned flexible, low cost - harvester unit, a customized energy tank needs to be developed with a matching form factor and electrical compatibility.

In the volumetric and gravimetric terms, energy storage technology is much efficient compared to that of energy harvesters. Hence for powering micro devices, without overloading the energy storage component, a miniature energy storage component is required. Though many different types of energy storage technologies exist, two classes of devices, batteries and capacitors dominate the micro scale arena. The choice between either is decided on the application. Branching out from these broader classes, various types of capacitors and batteries exist.

Capacitors, commonly employed for a short term energy supply range from miniature dielectric capacitors to large transmission scale oil filled ones.⁸⁸ However, the ideal one to support energy harvesting would have a high capacity packed in a very light weight miniature device. Supercapacitor is the term coined for capacitors with very high capacity and ideal for such a system.⁸⁹ Moreover, apart from capacitors, batteries are also an important alternative. While capacitors have the advantage of providing fast energy

required for applications like single shot sensors, batteries on the other hand provide a more robust uninterrupted energy for applications with continuous operation requirement. Numerous capacitor and battery choices exist and choosing one that is optimum for integration to the harvester has to be done wisely.

A comprehensive background about the current state of these two alternatives, viz. lithium ion batteries and electrochemical supercapacitors is taken up. In particular, electrochemical double layer supercapacitors and lithium ion batteries have been identified as the choice of technologies by understanding their working principle and performance characteristics.

1.2.1. Lithium ion batteries

The development and commercialization of lithium ion batteries have revolutionized the energy industry by making portable energy more efficient and robust.⁹⁰ However, the need for higher energy densities and cycle life along with being economically viable and environmentally benign requires constant research and development of new materials for each of the components of a battery. A typical lithium ion battery consists of two electrodes (cathode and anode) separated by an electronically insulating and ion permeable porous separator membrane, confined in an electrolyte containing lithium salt, most commonly, LiPF_6 in ethylene carbonate–diethyl carbonate. The charge and discharge of a lithium ion battery can be visualized as the tunneling of lithium ions through the electrolyte from cathode to anode and vice versa respectively, forcing electrons through the external circuit to maintain charge neutrality.⁹¹ Figure 1-1 illustrates the schematic of a typical lithium ion battery mechanism.⁹²

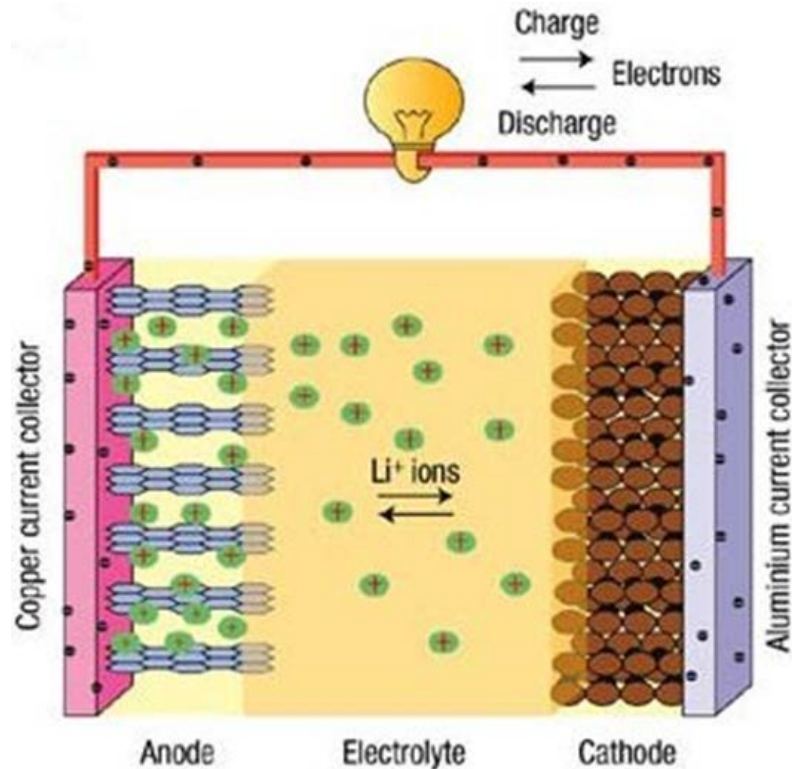


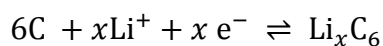
Figure 1-1: Schematic of the charge and discharge mechanisms in a lithium ion battery (adapted from ref [92])

The capacity of the battery is defined as the amount of reversible lithium that can be stored into either of the host electrodes. And, the net cell voltage is the difference between the lithiation potentials of the two electrodes. Often, to increase the net capacity of a lithium ion battery, the anode and cathode materials are chosen further apart in the electrochemical window. The process of intercalation and de-intercalation of lithium at the surface of the electrode is a solid state redox reaction and is followed by solid state diffusion of lithium atoms into the bulk of the material.⁹³ The penetration of a new atom into the bulk lattice of the electrode results in significant volume expansion and subsequently, changes in its crystal structure or phase. The conductivity of electrode is

critical in having a good electron transfer and conventionally, conductive additives are added to electrode materials to enhance electron transfer. Apart from the favorable reversible lithiation and de-lithiation reactions, any additional reactions that may occur between the electrodes and the electrolyte would result in the fading of capacity over cycling due to the loss of usable lithium in the system.

Research efforts in improving the performance of a lithium-ion battery are multipronged. Several challenges in the field are being explored separately, including material optimization for the electrodes, separators, electrolytes and current collectors; exploring different chemistries, optimizing packaging, improving the dynamics by innovative engineering mechanisms, and also building tailored batteries for specific applications.⁹⁴⁻⁹⁶ The scope of this thesis is limited to exploring carbon based materials for anodes, with specific focus towards ultrathin lithium ion batteries.

Various isomorphs of carbon have been commonly used as the choice for anodes in a lithium ion battery.^{97,98} Low lithiation potential, good conductivity and structural stability makes it an ideal candidate. Many reports have tried to increase the net capacity in carbon structures following various methods (reported in the ranges of 250-800 mAh g⁻¹).^{99,100} Su et al. (2010)¹⁰¹ have done a comprehensive review of various carbon based structures that have been reported for use in energy storage applications. The review conveys that in case of graphitic carbon, more than one form of lithium storage mechanisms exists. In general, the storage of Lithium ions in carbon has been described as:



The number of lithium ions accommodated by a host of carbon atoms is defined by the carbon state in the structure. The nominal form of intercalation between the layers of graphite (Figure 1-2a) results in a theoretical capacity of, 372 mAh/g, wherein $x=1$.¹⁰² Though in a practical scenario, the capacity observed is lower due to secondary irreversible reactions. Sato et al. (1994)¹⁰³ has proposed that by having a crystalline disorder in the carbon structure, the dynamics of carbon reaction with lithium changes and a mechanism of upto LiC_2 is possible (Figure 1-2b). Also, in case of graphite, the carbon atoms at the edges are more reactive than that of the once inside the crystal lattice. Hence it is hypothesised that having more edge defects, such as voids in the lattice would result in more lithium ions concentration at these sites (Figure 1-2c).¹⁰⁴ Also, Dahn et al.(1996)¹⁰² proposed a model that, if the graphene layers are exfoliated into individual layers, instead of stacking up, lithium ions can be physically adsorbed on both sides of the layer. Exploiting this mechanism, a high stable capacity of 540 mAh g⁻¹ was reported with chemically exfoliated graphene nanosheets.¹⁰⁵

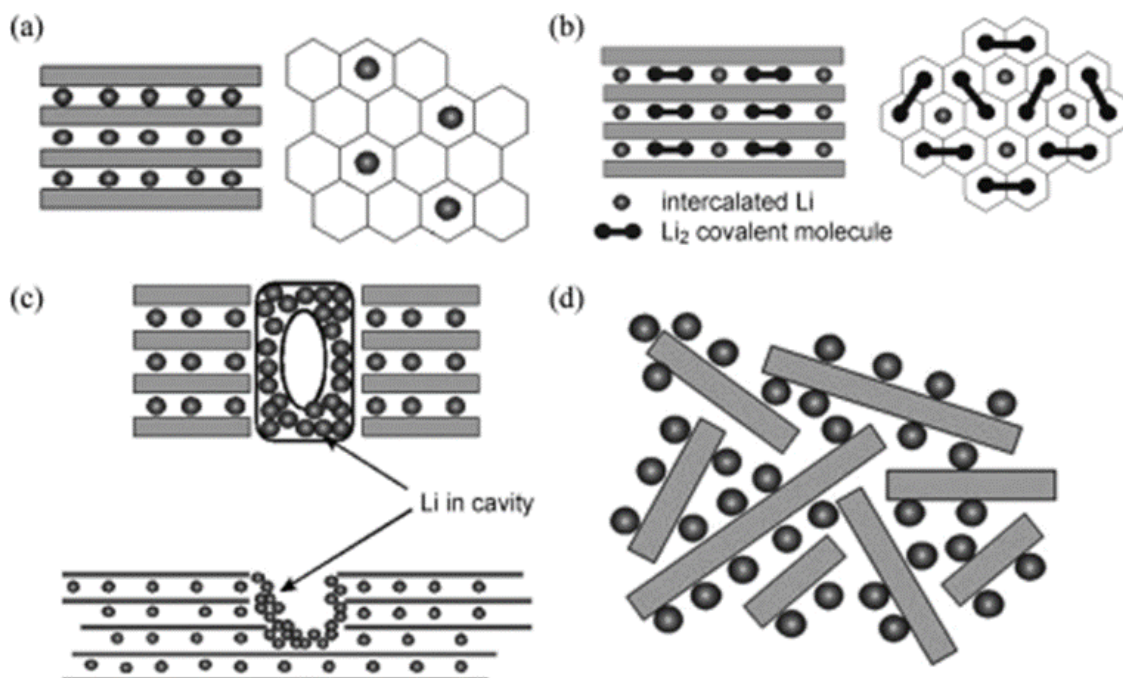


Figure 1-2: (a) Storage mechanisms of Li ions in graphite. (b) Li storage in form of Li_2 covalent molecules¹⁰³ (c) Schematic model of Li storage in cavities and nano pores¹⁰⁴ (d) Dahn's model of Li adsorption on the two sides of an isolated graphene sheet¹⁰⁶. (Adapted from [101])

Many challenges exist in using carbon materials in a lithium ion battery.

Formation of a solid electrolyte interphase (SEI), which is a result of decomposition of organic compounds present in the electrolyte onto the surface of the electrode, is prevalent with the carbon electrode. The SEI film formation is a self-limiting process and is often observed only during the first discharge of the battery. If this film is not stabilized, a loss in reversible capacity over cycling would be seen, as new lithium ions are needed to form a fresh SEI.¹⁰⁷ Another concern with the carbon electrodes is that a proper contact between the electrode and the current collector is essential for realizing its full efficiency. Nevertheless, a number of research efforts have been taken up to explore all the hypotheses of increasing the capacity of graphitic carbon by nanostructuring it.

Extensive research has been conducted on carbon nanotubes, with several benchmark publications reporting remarkable performance.¹⁰⁸⁻¹¹²

Apart from using carbon as an electrode material, it has also been used as a secondary support for other high capacity materials. Numerous studies have been undertaken to use carbon nanostructures as a matrix to provide an electrical and structural support to both anodic and cathodic materials.¹¹³⁻¹¹⁶ One such example is the use of coaxial nanostructures of CNT- MnO₂ by Reddy et al (2009).¹¹⁶ By jacketing a CNT with a layer of active electrode material, electron transfer to it is maximized, resulting in a high rate capability and electrode stability over cycling.

1.2.2. Supercapacitors

Supercapacitors, the common name used for Electric double layer capacitor (EDLC), are a class of energy storage devices capable of rapid charging and discharging, producing large energy in short intervals of time. They exhibit large cycle life of over thousands of cycles and high cyclic efficiency. An EDLC consists of two identical electrodes, typically carbon based, separated by an ion permeable membrane, and immersed in an ionic electrolyte. Energy storage in a supercapacitor occurs by the formation of an electrochemical double layer by the accumulation of charges onto active surface areas. The charge separation and recombination define the charging and discharging of a supercapacitor.⁸⁹ Figure 1-3 is a schematic of the charge discharge mechanisms in a conventional double layer supercapacitor.

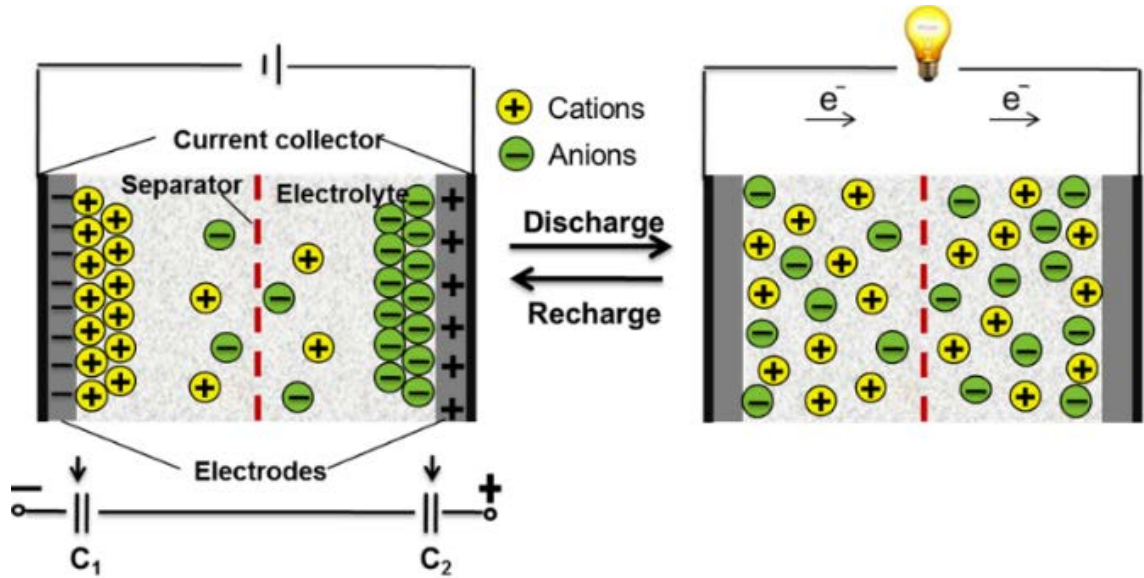


Figure 1-3: Schematic of the mechanism of charge and discharge in an EDLC showing the charge separation and recombination during charging and discharging process leading to the formation of double layer at the electrode.

The net capacitance of the capacitor is the sum of capacitances of the two double layers formed on the surface of the electrodes. At these interfaces, the capacitance is similar to that of a parallel-plate capacitor and governed by the relation,

$$C = \frac{\epsilon_r \epsilon_0}{d} A$$

The capacity is directly proportional to the surface area of the electrode (A) and inversely proportional to the separation between the charges (d – Debye length). As the charges in the double layer are separated by an atomic scale separation, and as a result the net capacity is very high (hundreds of farads per gram) compared to dielectric capacitors.

Also, EDLCs have been reported to exhibit long cycle life, as the mechanism is non-faradaic and no chemical degradation occurs to the electrode, with high power

densities of up to 1 kW kg^{-1} .¹¹⁷ Use of carbon as electrodes for supercapacitors has been a well explored field, owing to its several advantages such as high specific surface area, large specific capacitances ($100\text{--}300\text{ F g}^{-1}$), low material costs, etc.¹¹⁸ The energy density of the device depends on the amount of active surface area available per unit mass of the electrode. Use of nanomaterials or nanostructured materials result in active materials with very high specific surface areas.¹¹⁹ For example, use of graphene instead of graphite enhances the energy density by orders of magnitude for the same weight of the electrode as more surfaces are exposed to the electrolyte. Specific capacitances of about 115 F g^{-1} and power densities of about 30 W kg^{-1} have been reported by the use of reduced graphene oxide which is otherwise a few W kg^{-1} for conventional EDLCs.¹²⁰ The following section discusses this interesting structure and its properties in more detail.

1.2.3. Graphene - a new frontier carbon material

Graphene is defined as a single layer of carbon atoms bound into a 2-Dimensional, $\text{sp}^2\text{-sp}^3$ hybridized honeycomb lattice. It can be seen as peeling off a single sheet out of layered graphite. It has received great excitement from the scientific community, especially after uncovering some of its astonishing properties by many researchers over time and notably by A. K. Geim and K. S. Novoselov.¹²¹ It is termed as the “mother of all graphite forms”, as this base structure when introduced with defects, can be molded into any of the 0 to 3 dimensional carbon structures, the schematic depiction by Geim et.al shown in Figure 1-4 postulates this hypothesis.¹²¹ It is considered as a very promising material by fields across the board ranging from physics, chemistry, material science and even bio-technology.¹²² Particular interest on this 2D material

comes from the fact that it possesses a package of astounding properties.¹²³ Theoretically, it has a large gravimetric specific surface area ($2630 \text{ m}^2\text{g}^{-1}$), high intrinsic mobility ($200,000 \text{ cm}^2 \text{ v}^{-1}\text{s}^{-1}$)^{124,125}, high Young's modulus ($\sim 1.0 \text{ TPa}$)¹²⁶, thermal conductivity ($\sim 5000 \text{ Wm}^{-1}\text{K}^{-1}$)¹²⁷, and optical transmittance ($\sim 97.7\%$)¹²⁸.

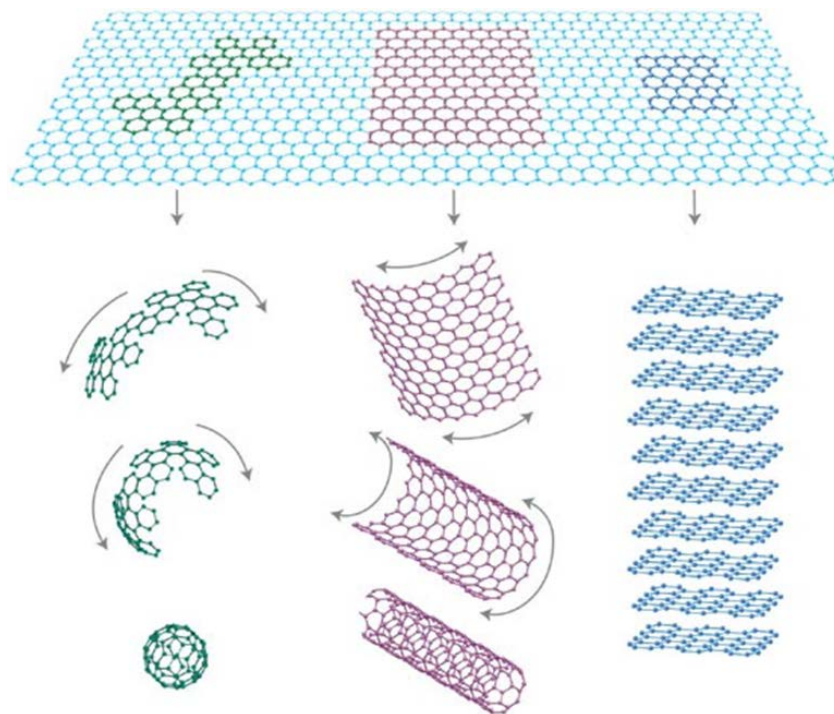


Figure 1-4: Structure of a 2D layer of graphene and depiction of molding it into 0-D Buckyball, 1-D CNT and 3-D graphite forms. (Adapted from ref [121])

While graphite is a naturally occurring form of carbon, synthesizing graphene has been a scientific achievement to mention. Various routes have been employed to make different types of graphene based structures. While chemical synthesis protocols have been developed to exfoliate individual layers out of graphite, chemical dopants in the final structure is almost always unavoidable.¹²⁹ Thermal, mechanical and high energy

exfoliation techniques have also been reported, with considerable success in realizing pure carbon graphite.^{130,131} However, all the exfoliation methods result in graphene flakes in a powder form factor which, if required to be used in any application, pose challenges of assembly. Moreover, graphene being a 2D structure, electrical conductivity between these individual flakes is not as high as that of the flake itself and as a result significant electrical losses are inevitable.

Synthesis of large area continuous graphene with controlled number of layers has been first achieved in 2009, reported by two separate groups.^{132,133} Kim et al., (2009) have reported a CVD process for depositing few layer graphene onto metallic Nickel and Li et al.,(2009) have reported a procedure for self-limiting deposition of one to two layered structures on copper. These two reports have opened up the possibility of controlled deposition, patterning and usability of graphene at the device scale.

Tapping on the superior properties, many innovative applications have been proposed for graphene. The exceptionally high mobility in the structure has promise in electronic applications as conductors and interconnects.¹³⁴ Being a zero band gap semiconductor, has prospects of FET.¹³⁵ Optical transparency is key to using graphene in optoelectronic applications such as LED displays and solar cells.¹³⁶ In this front, Samsung has already started to explore the feasibility of developing bendable displays using graphene grown on very large areas.¹³⁷ This could eventually pave way for flexibility in wearable electronics. The chemical inertness and high Young's modulus have made graphene an attractive material for surface coatings. Protecting the surface from corrosion without substantial addition to the weight and volume is an attractive proposition.¹³⁸ Moreover, it has also been shown that a single layer of graphene, in some

cases, is transparent in terms of wettability. Surfaces where hydrogen bonding is not dominant, presence of one layer of graphene does not change its hydrophobic or hydrophilic nature.¹³⁹ The high gravimetric surface area makes it a candidate for high capacity batteries and supercapacitors, aimed at packing of more energy per unit weight of the device.¹⁴⁰

To use graphene in an electrochemical device, the choice of the underlying metallic substrate needs to be taken care of, as not all metals sustain the rigorous chemical reactions in a cell, especially at elevated environmental conditions such as high temperatures. Moreover the mechanical integrity and electronic conductivity of the electrode would need to be preserved under strong agitations expected to be witnessed by the battery/supercapacitor. CVD deposited graphene on to metallic substrates would be an ideal choice for such an application, if suitable metallic substrate can be identified that is stable for such applications. Directed towards energy storage applications, this thesis deals with first developing variations of graphene based materials, directly onto stable metallic substrates and later testing their efficiency in energy storage.

1.3. Scope of thesis

This thesis deals with exploring material configurations for energy harvesting and storage devices which are geared towards ultimately building an integrated energy self-sufficient system. Chapter 1 introduces the need of such energy self-sufficient devices and provides a comprehensive literature survey of the relevant research topics. Chapter 2 deals with synthesising a novel piezoelectric composite material, consisting of ceramic Zinc Oxide embedded into the matrix of ‘paper’. The chapter also goes on to fabricate

devices and using them for energy harvesting from multiple sources of excitations.

Additionally, its use as an efficient candidate for strain sensing is also discussed. In order to effectively use the energy generated from an energy harvester, the power generated needs to be built up and stored for later use. Chapter 3 deals with the development of synthesis protocols for direct growth of graphene based materials onto metallic substrates. While chapter 4 deals with exploring their use in energy storage application. A systematic study of increasing the performance of graphene as an electrode material in lithium ion batteries and supercapacitors is taken up. Combining the piezoelectric harvester described in chapters 2 with a graphene based supercapacitor is also discussed in chapter 4. Finally, chapter 5 summarizes the key findings and benchmarks of this thesis.

Chapter 2

Developing flexible piezoelectric composite material

Piezoelectric materials have the capability of converting energy from the surroundings, often from more than one form, into surface electric charge. Among many of the proposed piezoelectric materials, Zinc oxide (ZnO) is a unique one as it has both semiconductor and piezoelectric properties¹⁴¹ and has an added advantage of low cost and easy synthesis of pure crystalline phase.¹⁴²⁻¹⁴⁵ Being a crystalline ceramic in nature, ZnO does not have mechanical flexibility and abuse tolerance to strains. This hinders the materials performance in active piezoelectric applications.

On the other hand, cellulose (main constituent of paper) has been used as a flexible platform for various applications including energy storage devices such as batteries and supercapacitors. Being light weight, abundant, environmentally benign, recyclable, and economically viable, cellulose has various advantages.¹⁴⁶⁻¹⁴⁹ The scope

of this thesis is aimed at using this ‘paper’ as a flexible medium to support ceramic form of piezoelectric ZnO, thereby forming a composite material.

Such a flexible piezoelectrically active material can be envisioned to have multitude of applications. ZnO being a pyroelectric material (a subgroup of piezoelectric class of materials) can convert thermal fluctuations, apart from mechanical stress, into surface charge. If these properties of bulk ZnO are preserved in the composite form, it can be used as a robust, flexible system to convert both mechanical and thermal energies into electrical. Energy harvesting from the ambient is a straight forward application and has been explored as part of this thesis. Sensitivity to strain can make this material a candidate for sensory applications, which is also evaluated in this chapter. The findings of this chapter have been reported in two publications, Gullapalli et al. (2010)¹⁵⁰ and Kumar et al. (2011)¹⁵¹

2.1. Fabrication of ZnO-paper composite

Using Paper as a matrix for integrating ceramic piezoelectric materials has several advantages to it. However the major hurdle in realizing this is its instability at high temperatures. The cellulose structures in the paper would decay at temperatures greater than 170°C in air. This limits the use of any high temperature reactions in the synthesis protocol. Ceramic materials generally require high temperature annealing to achieve good crystallinity. As an alternative, low temperature methods have been employed in this work for the growth of ZnO in a paper matrix. The choice of ZnO as the piezoelectric material is seconded by the many reports of synthesizing highly crystalline structures using low temperature protocols.^{152–157}

Sol gel synthesis technique which is one of the standard type of chemical synthesis methods had been used. The idea behind sol-gel synthesis is to “dissolve” the constituent compounds in a liquid medium and react them in a suitable condition to form the final sol. A Sol is defined as a stable dispersion of colloidal particles or polymers in a solvent. Chemical reactions at the atomic scale are performed by either mixing two or more Sol's in a controlled fashion or by subjecting the Sol to other energetic excitations such as heating.¹⁵⁸

For synthesis of ZnO, two solutions were prepared. The first solution (Sol-1) consists of 0.1M Zinc acetate dihydrate (purchased from Sigma Aldrich, used as received and stored in a moisture free desiccator) dissolved in 200 proof ethanol. The solution was heated at 60°C while stirring with a magnetic stir bar for 1 hour, to obtain a clear transparent solution. The second sol (Sol-2) is a 1M sodium hydroxide (NaOH) in 200 proof ethanol. Sol-2 was also slightly heated and stirred to obtain a clear transparent solution. Filter paper (Whatman, grade- 41 Ashless, with 20-25µm pores) was taken in a glass petri dish. The filter paper was first washed with pure Ethanol and dried in a vacuum oven at 100°C for 30 minutes. It was then soaked with Sol-1 by drop wise coating the solvent using a pipette. The soaked paper was dried again in the vacuum oven at 100°C. Soaking and drying of the paper with Sol-1 was repeated again for 3 to 4 times, until the paper is saturated and is unable to absorb any more solvent. Once saturated, the paper is then soaked with Sol-2 and dried, and the process repeated twice. After soaking in Sol-2, the paper is washed with pure De-ionized Water and dried for 30 minutes. The entire process of soaking with Sol-1, Sol-2 and washing with DI water is repeated 5 times. Once done, the net increase in the weight of the filter paper is about 30%. The

mechanism of formation of the final ZnO nanostructures involves first formation of ZnO nanoparticles due to hydrolysis of zinc acetate using sodium hydroxide. As the concentration of zinc oxide nanoparticles increases, it becomes a quasi-continuous film, which then serves as the seed for growth of zinc oxide nanorods. The quality of the final ZnO structure critically depends on the quality and adhesion of the first seed layer deposited on the paper, and hence proper homogeneous coating and drying during the initial cycles is critical.

2.2. Characterization of ZnO-paper composite

Photographs of thus formed ZnO-paper composite with gold sputtered on the surface are shown in Figure 2-1. The composite remains flexible and bending it does not damage its mechanical structure and the deformation is fully recoverable.

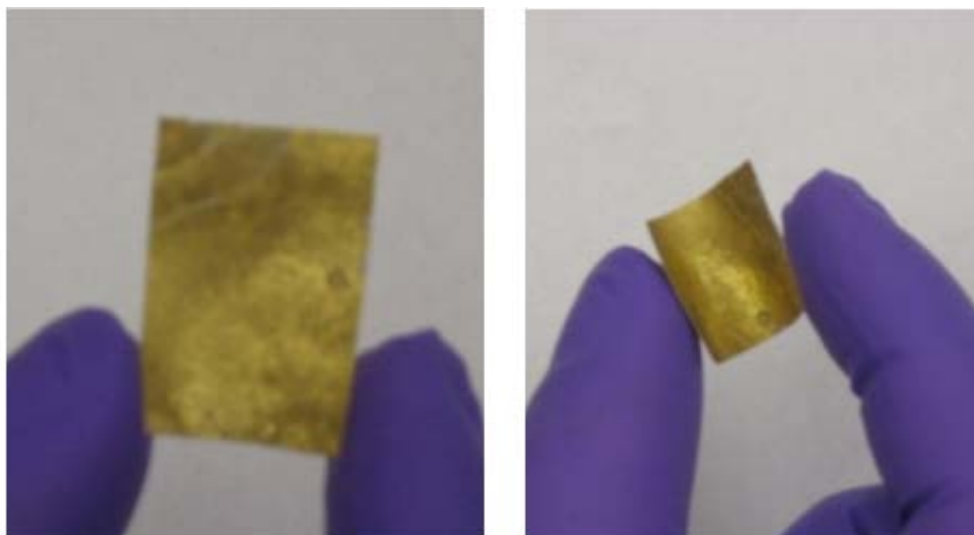


Figure 2-1: Photographs of the ZnO-paper composite with gold coated on the surface

The morphology of the ZnO-paper is observed by scanning electron microscope (FEI Quanta 400, operated at 20 kV and equipped with an energy-dispersive X-ray spectrometry (EDS) detector). The micrographs of plain filter paper are shown in Figure 2-2. The microstructure of paper consists of intermingled fibers which in turn are made up of finer cellulose fibers. It is clearly visible that most of the volume in the paper structure is void and consists of both macro and micro pores. This porous structure can accommodate considerable mass of ceramic without losing its mechanical integrity.

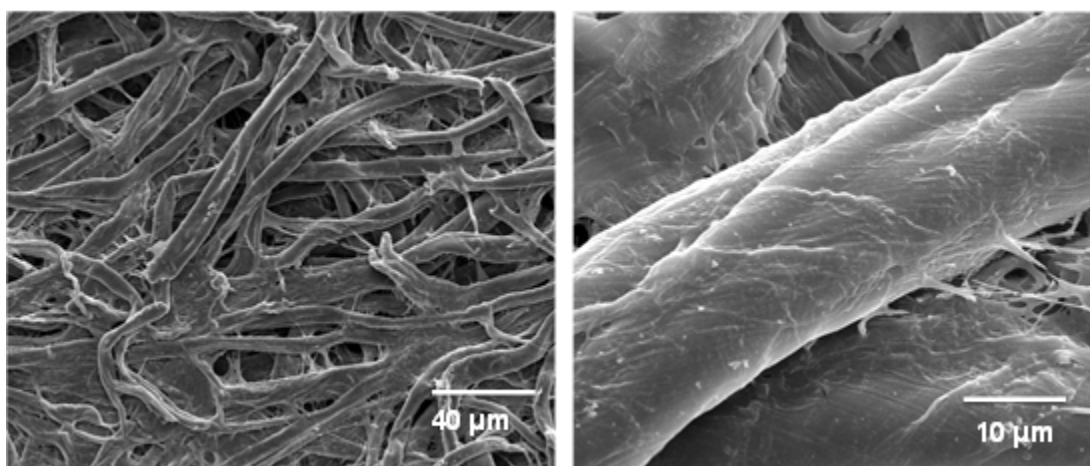


Figure 2-2: Scanning electron micrographs showing the structure of plain filter paper. Cellulose fibers are intermingled to form a porous network

The images in Figure 2-3 show the SEM images of the microstructure of ZnO infused paper. The cellulose fibers in the paper are conformally coated with ZnO thin film and also nanorods protrude out from this crystalline film. The structure of the composite paper is schematically depicted in Figure 2-3 (d). The ZnO nanorods have a typical diameter in the range of 40-100 nm and lengths between 500-1000 nm. It can be

seen from the SEM images that even after loading the paper with 30% by weight with ZnO, the macro structure still has considerable porosity, making the composite very flexible and mechanically robust.

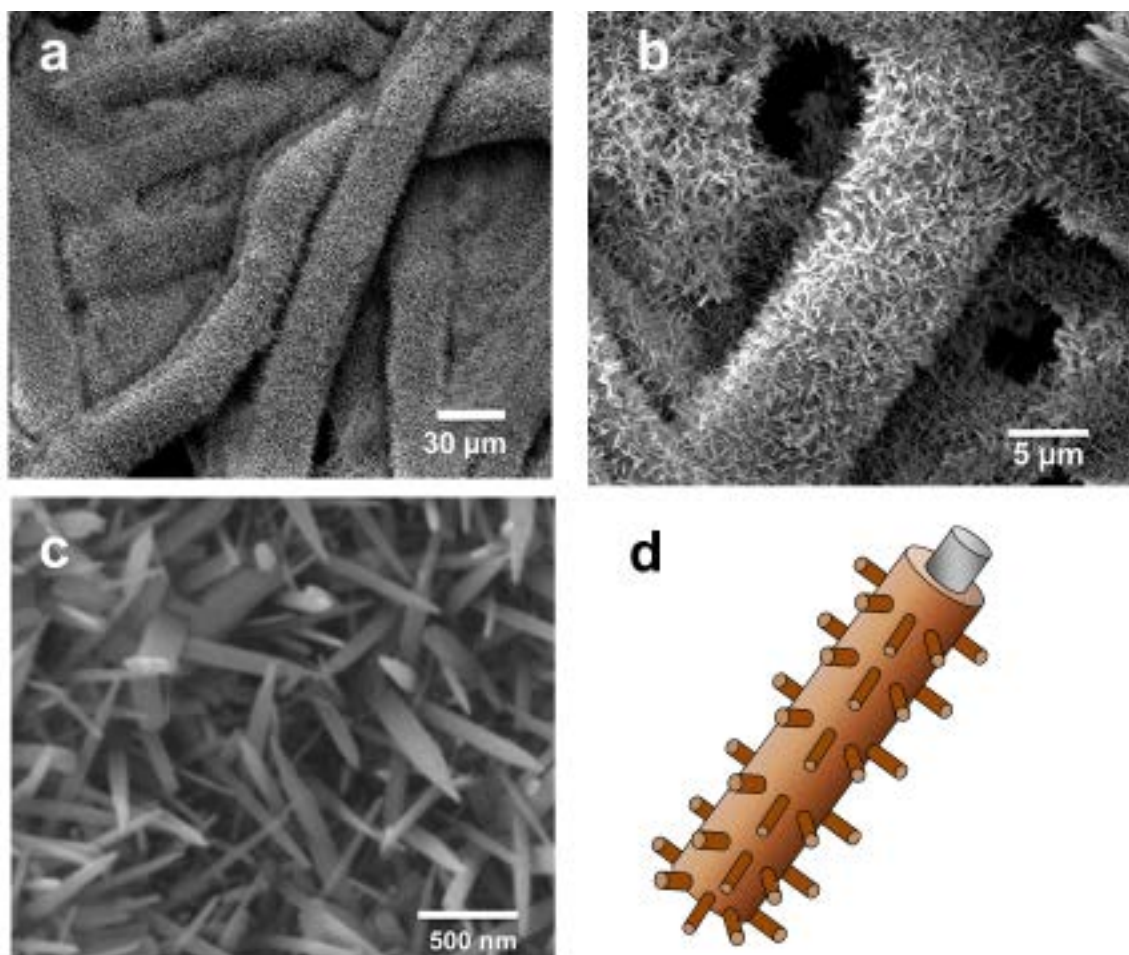


Figure 2-3: (a-c) Scanning electron micrographs of ZnO-paper composite. (d) Schematic depicting the structure

Energy dispersive X-ray analysis (EDAX) done on the composite, confirms its chemical build-up. The survey analysis done on the surface, is shown in Figure 2-4, with the prominent peaks labeled with their corresponding elements. The peak corresponding

to gold on the surface is a result of the thin layer sputter coated on to it to make the sample conductive. The other three prominent peaks correspond to Zinc, Oxygen and Carbon. The important aspect of this measurement is that there is no substantial presence of Sodium in the composite, ruling out any remaining contaminant or secondary products from the sodium hydroxide used during the synthesis process. The crystallinity of the ZnO in the composite is studied using an X-ray diffractometer (Rigaku D/Max Ultima II) operated at 40kV and using CuK α radiation. Figure 2-5 shows the diffraction spectrum of the composite. The peak positions have been mapped to their corresponding compounds using the Jade reference software with elemental database. The first three prominent peaks below 40° in the spectrum correspond to the cellulose matrix, while the angles of the other prominent peaks clearly coincide with the Wurtzite structure of ZnO, confirming its crystal structure. Also, no other secondary phases have been detected, implying the crystalline purity in the system.

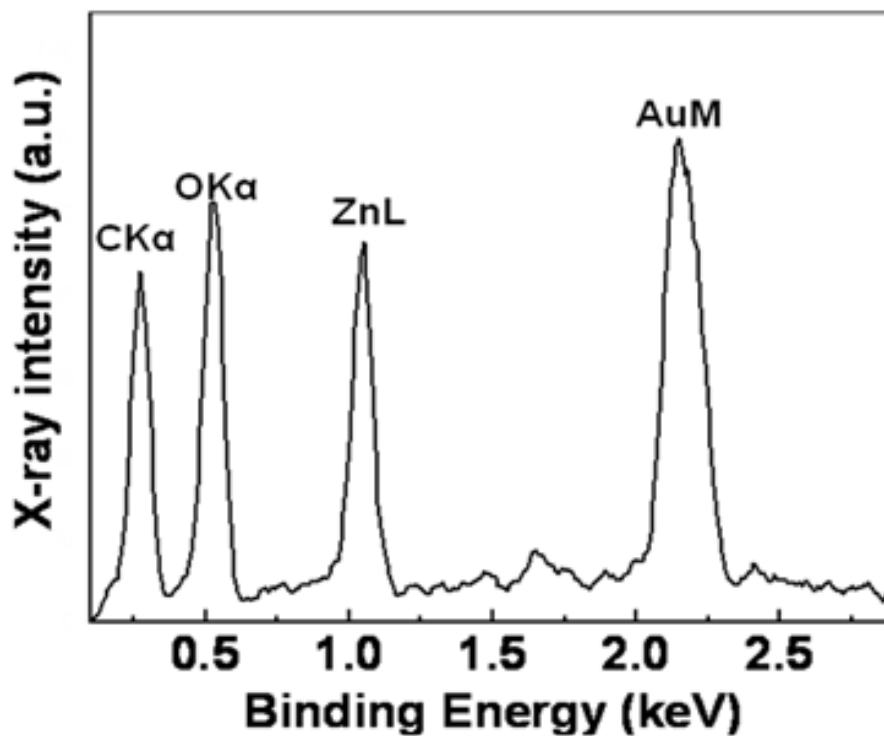


Figure 2-4: Energy dispersive X-ray analysis used to detect the elemental composition of the surface of ZnO-paper

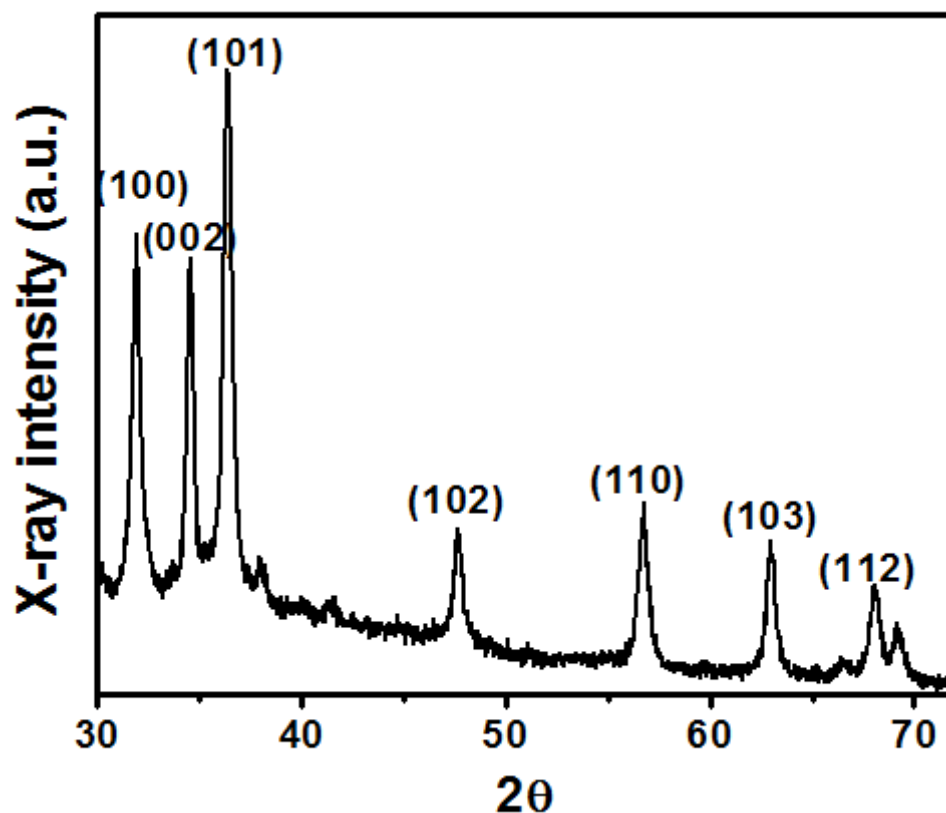


Figure 2-5: X-ray diffraction spectrum of the Zn-Paper composite. The peak position closely match with the wurtzite structure of ZnO

The ZnO rods grown on cellulose paper was further characterized by Transmission electron microscopy. The ZnO–paper was sonicated in ethanol and the dispersion dropped on a carbon coated copper grid. The rods were observed to be uniform and discrete with a diameter $\sim 20\text{nm}$. High-resolution TEM image shown in Figure 2-6 reveals the uniform crystalline nature of one of the rods, with the FFT diffraction patterning in the inset confirming the [002] crystal plane of ZnO crystal.

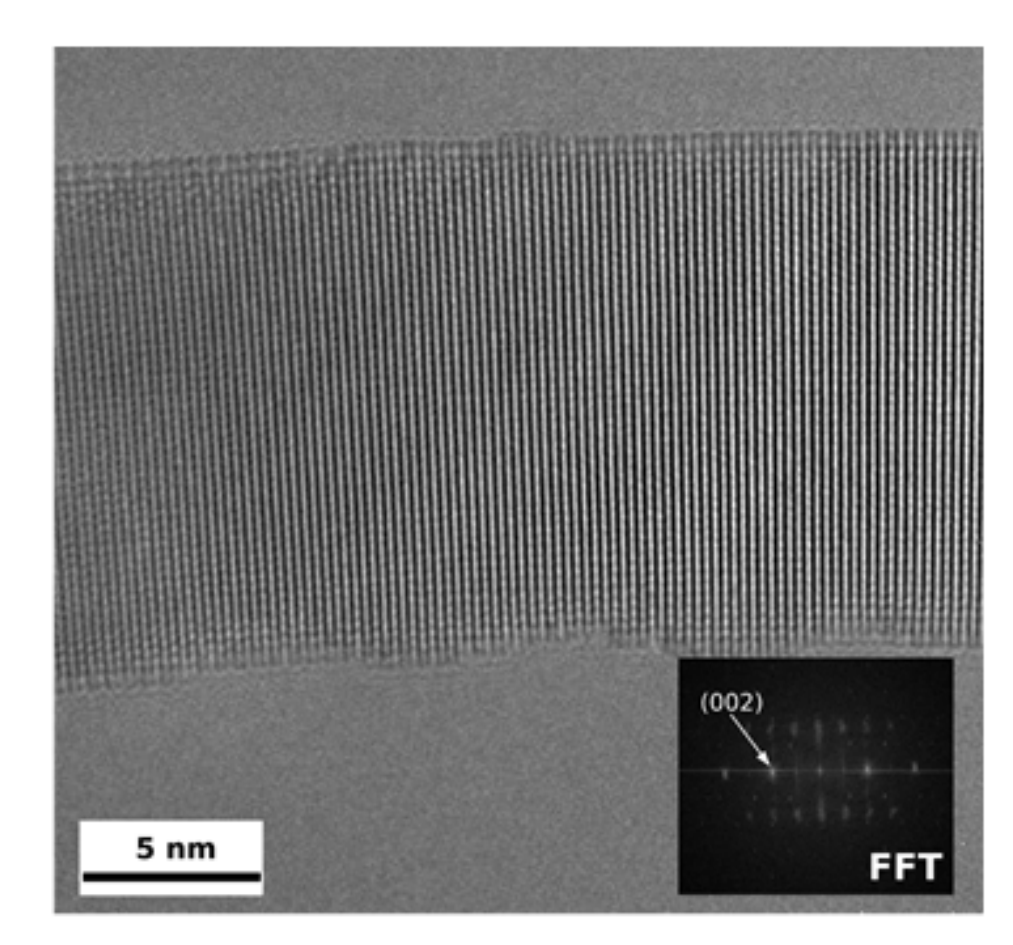


Figure 2-6: Transmission electron micrograph of a single ZnO nanorod extracted from the ZnO-paper composite. Highly uniform crystallinity is observed and confirmed with the diffraction pattern in the inset

To quantify the amount of ZnO present in the composite structure, Thermogravimetric analysis (TGA) was employed. The thermal analysis plots of plain paper and the composite, with the weight measured against a continuously ramped temperature up to 800°C in air, is shown in Figure 2-7 (a) and (b) respectively. It can be seen from the plot in Figure 2-7 (a) that there is no considerable weight loss until about 300°C, proving the stability of the structure. There is about 90% drop in the weight after 300°C, which

can be attributed to the decomposition of cellulose. When comparing this to that of the weight profile of the composite in Figure 2-7 (b), the composite loses 55% of its weight after 200 °C. ZnO being ceramic, can withstand much higher temperature, the reduction in weight can be safely attributed to the decomposition of cellulose matrix. By comparing these two results, the net gravimetric composition of the ZnO-paper can be deduced to be of ~35 wt% ZnO and 65wt% paper matrix.

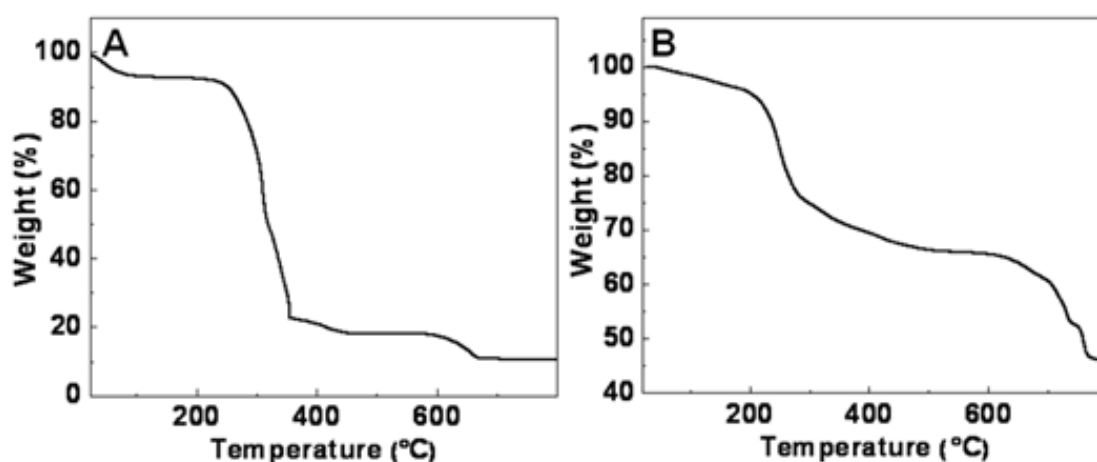


Figure 2-7: Thermogravimetric analysis plots showing the weight loss of (A) plain filter paper and (B) ZnO-paper composite as they are heated in air. Comparing the trend, it can be deduced that the ZnO-paper has a 35% by weight of ZnO in it.

2.3. Mechanical energy harvesting

Piezoelectric devices are designed to use piezoelectric materials that have the ability to generate charges when they are under stress/strain, as described in Section 1.1. Conventional piezoelectric harvesters are expensive as a high crystalline purity and defect free nature is required. Flexibility of the piezoelectric component is required for

many applications and also increases the efficiency. The applicability of ZnO-paper as a cheaper and robust alternative for harvesting mechanical vibrations is taken up here.

2.3.1. Experimental details

To test the mechanical energy harvesting capabilities of the ZnO-paper composite material, a test device had been fabricated. As mechanical excitations to the composite would result in charge accumulation on its surface, a conductive current collector is required to collect them. In order to have a good electrical contact with the microscopically rough surface, gold was sputtered (100nm thick) on to either surfaces of the ZnO-paper. This gold coating also acts as a diode, as it is known that gold-ZnO have a schottky contact, allowing current to flow only in one direction.¹⁵⁹ The gold coated ZnO-paper is then cut into required sizes (typically 1cm X 1cm in area) and sandwiched between two copper current collectors and laminated using a commercial ID card laminator. The final device is shown in Figure 2-8 along with a schematic depiction of the cross-section. This lamination helps in keeping the components tightly packed and also protects them from exposure to harsh environmental conditions. Even exposure of ZnO-paper to atmosphere for a prolonged time is vicious, as the highly porous structure absorbs moisture which in turn dampens the piezoelectric nature.

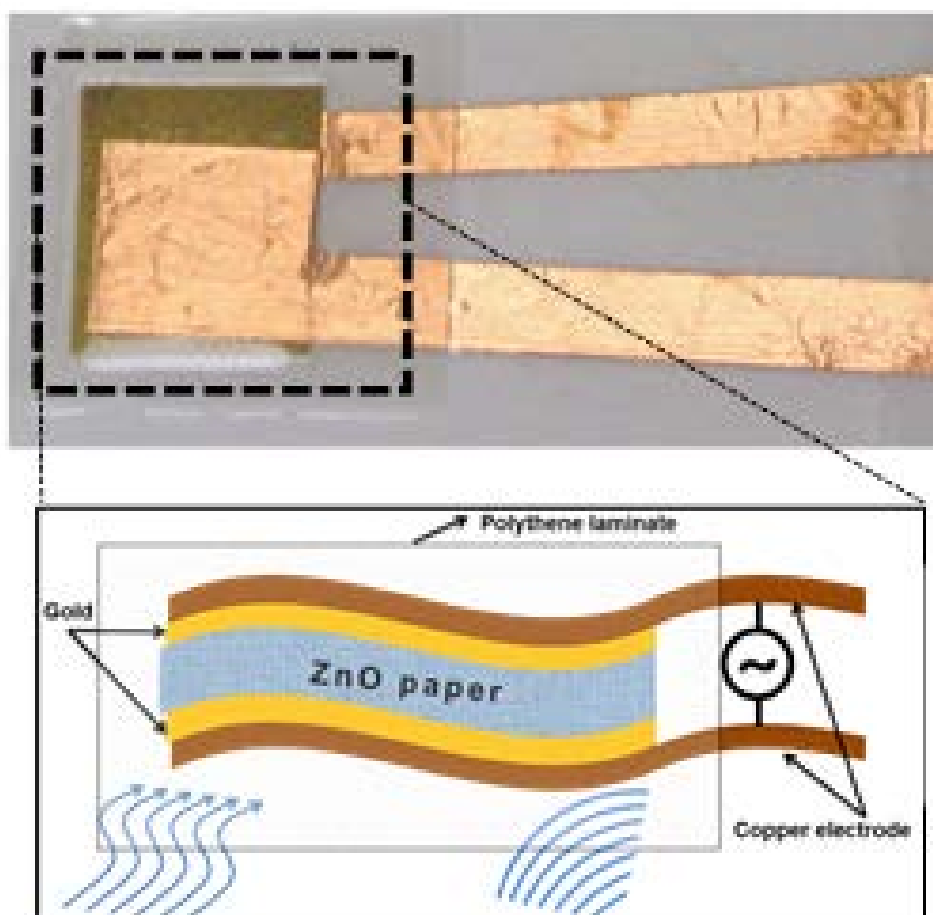
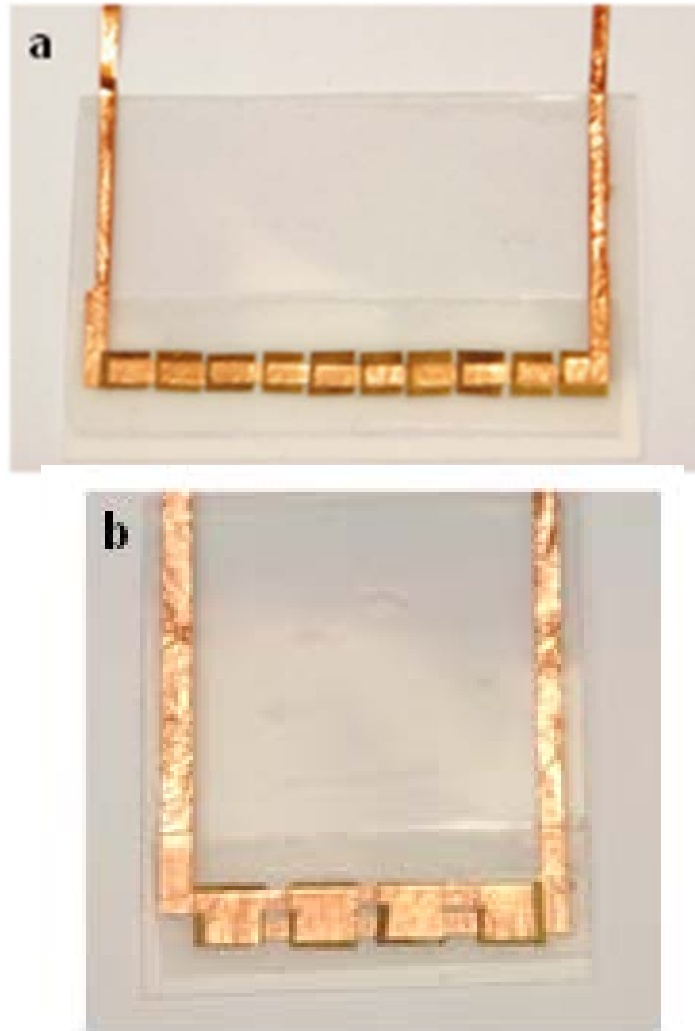


Figure 2-8: Photograph of a device made of ZnO-paper composite. Schematic describes the cross section of the structure

In order to test convoluted effects of energy harvesting, multiple pieces of the composite can be connected in series, parallel or a combination thereof in a single packaging. Photographs of some of these interconnected devices are shown in Figure 2-9.



**Figure 2-9: Photographs of devices with interconnected ZnO-Paper patches.
(a) 10 in series (b) 4 in parallel**

Before any measurements are done, the device needs to be poled. This is required as the ZnO structure in the composite is polycrystalline in nature and has randomly oriented dipole orientation in each crystal domain. To have a convoluted piezoelectric effect, these dipoles in the crystal structure need to be aligned (schematically depicted in Figure 2-10).⁶⁶ This is achieved by applying a voltage of $20\text{V}/\text{cm}^2$ across the terminals

for 30 minutes. After this, a residual capacitive voltage is observed in the device which is removed by short circuiting the two terminals for 30 minutes. The device is used for energy harvesting measurements only after the open circuit voltage and current are close to zero.

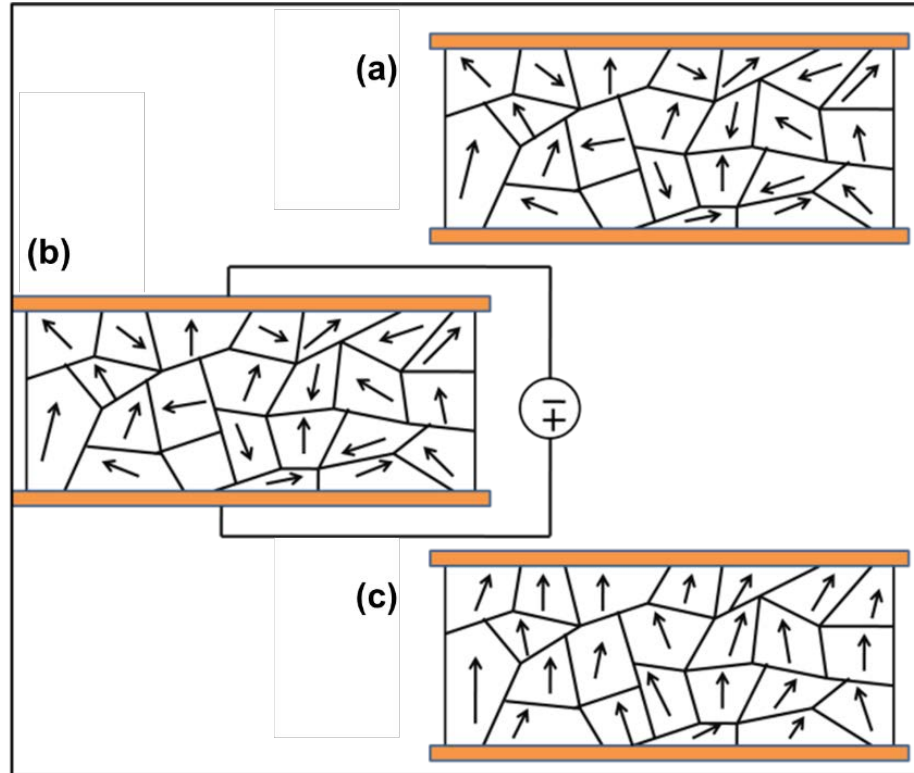


Figure 2-10: Schematic depicting (a) polycrystalline material with random dipole polarization (b) Polling with an external voltage bias (c) aligned polarity

To mechanically excite the device, it is submerged in a sonication bath. The vibrations from the sonicator are Gaussian in frequency and as a result the device sees a randomized high frequency mechanical energy. Electrical output from the device is measured across the two terminals. The current output from the device is measured using a current meter (model: Keithley 2400, with a sensitivity of 10pA and a sampling rate of

100 samples per second), while the voltage output is measured across a $1\mu\text{F}$ connected in parallel to the device. The Keithley is connected to a computer and is controlled and read through a Labview program.

2.3.2. Results and discussion

The current output from a device made out of a patch of 0.5 cm^2 ZnO-paper is shown in Figure 2-11(a). The output current from the device is continuously measured while it was immersed in the sonicator water bath for certain time and then removed. The current output reaches a peak value of about 350nA when the device is immersed in the bath and it quickly drops to zero when removed out of it. The output is not instantaneous and is stable as long as the device is under mechanical agitation. To scale up the current, multiple pieces of ZnO-paper can be connected in parallel. One such device with 4 pieces of 0.5 cm^2 area each connected in parallel is tested under similar conditions. The output current profile from this device upon cycled mechanical excitation is shown in Figure 2-11(c). A current of close to $0.7\mu\text{A}$ has been observed from this device. The current output does not linearly scale with the number of patches present in the device, owing to losses in interconnects between them.

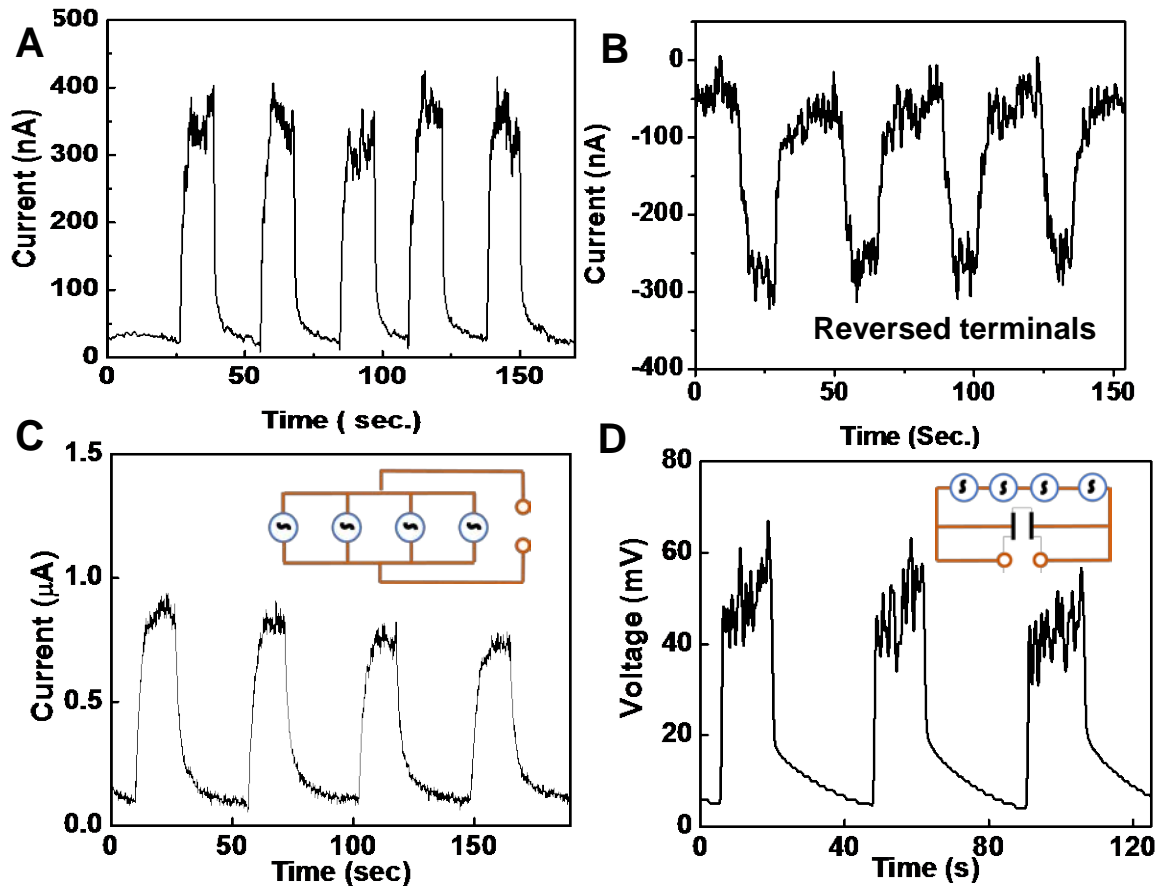


Figure 2-11: Energy harvested from the ZnO-paper device. (a) Current output when one device (0.5cmX0.5cm) is vibrated (b) Output when terminals reversed (c) Current output with 4 patches in parallel (d) Voltage output with 4 devices in series

The vibrational response in the ZnO-paper can be explained as follows. The strain transferred from the vibration creates two types of stresses on the ZnO coated paper: a) as the cellulose fibers are deformed, the nanorods on their surfaces get rubbed against each other, causing them to deflect, and generating a potential difference (or piezoelectric potential) along the nanowire diameter; and b) since the fibers are coated with a ZnO thin film, there is a strain due to the deformation of the fibers. The ion displacement due to this strain creates a difference of potential along the thin film. The potential difference

that drives the current from one electrode to the other is in the ZnO thin film and the difference of potential within individual nanorods barely contributes.

2.4. Thermal energy harvesting

Thermal energy in the ambient is present in two different forms. Thermal gradient between two regions and thermal fluctuations involving change in temperature of a region over time. While thermal gradients are harvested using thermoelectric effects, temperature fluctuations can be harvested using pyroelectric materials. Alternatively, secondary piezoelectric effects are also observed due to the strains created by the thermal gradient. ZnO being a pyroelectric and semiconducting material, its use in harvesting thermal energy is explored here.

2.4.1. Experimental details

The device fabricated by sandwiching the ZnO-paper composite between metallic current collectors can be used for harvesting thermal energy. The device was similar to the one used for mechanical energy harvesting. A probe thermocouple is attached next to the ZnO-paper and is connected to a temperature readout, which in turn is connected to a computer. A Lab view program is developed which can simultaneously read data from the temperature controller and the Keithley meter with a synchronized timestamp.

To test the effect of thermal energy on the device, it is placed on a ceramic topped hotplate maintained at 150°C. Cycling between hot and cold zones is done by manually removing the device from the hotplate while still continuously measuring the temperature and current from the device.

2.4.2. Results and discussion

The open circuit current measured while cycling the device, made out of a 1cm^2 ZnO-paper, between heating on a hotplate and cooling naturally is shown in Figure 2-12(a). The temperature profile has also been plotted along with the measured current. It can be clearly observed that a current is observed at the output when the device heats up and reaches a maximum value of $\sim 1.25\ \mu\text{A}$. The current profile follows the temperature seen by the device and clearly depicts the thermal energy harvesting nature of the ZnO-paper ceramic composite. To rule out any artefacts during the measurement the terminals on the device have been interchanged and the measurements repeated. The current profile from the device with the terminals reversed has been plotted in Figure 2-12(b). The current observed still follows the duty cycle of the temperature but with a negative polarity, confirming that the observed current is in fact a result of energy harvesting and not due to any stray electromagnetic fields that may result in an artefact. In a similar way, the voltage generated across the terminals is also measured and the output profile upon thermal cycling is plotted. Both cases of measurements taken with forward and reversed terminals have been shown in Figure 2-12(c) and (d) respectively. A peak voltage of $\sim 80\ \text{mV}$ has been observed in this case with the device of 1cm^2 active material.

To test the scalability of the harvesting nature of ZnO-paper, devices with larger active material have been tested. Higher output currents of $\sim 18\ \mu\text{A}$ and $\sim 45\ \mu\text{A}$ were achieved using $4\ \text{cm}^2$ and $9\ \text{cm}^2$ size devices, respectively and plotted in Figure 2-13

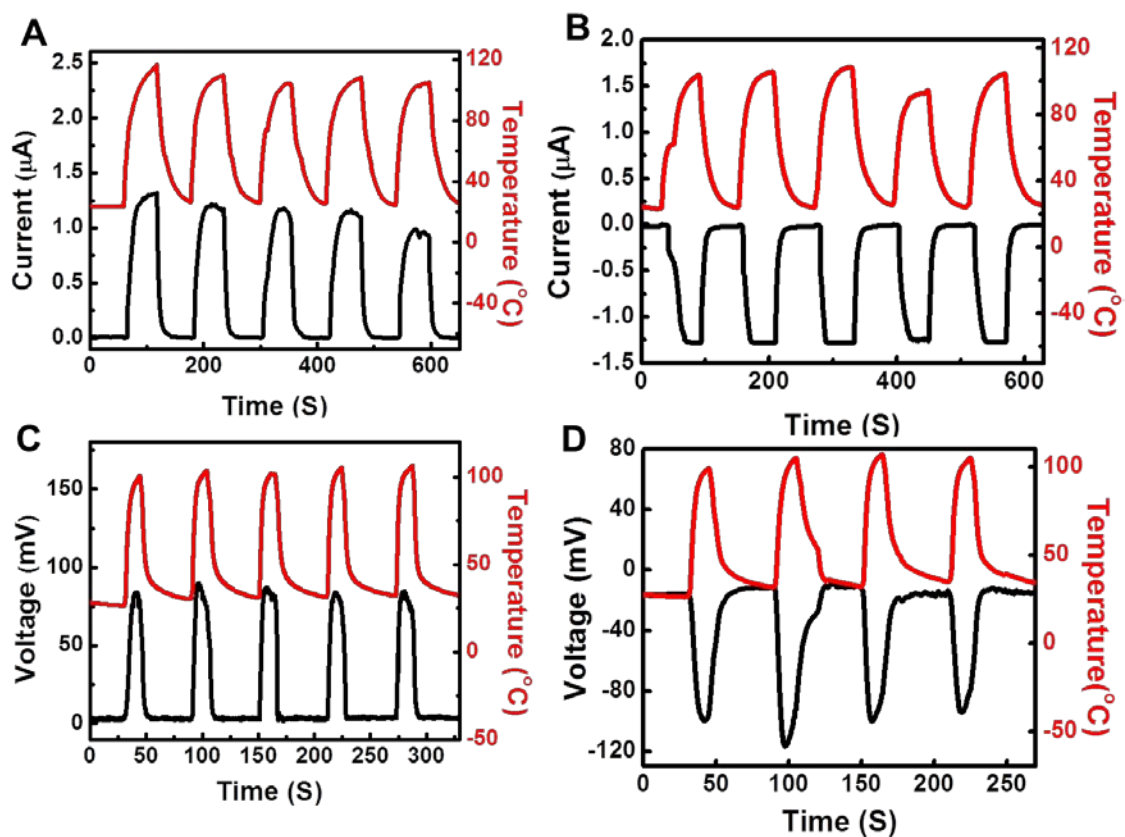


Figure 2-12: Plots of thermal energy harvested with the ZnO-paper device. (a) Current output as a result of repetitive heating cycles (b) Output when terminals are reversed (c & d) Voltage output of the same device

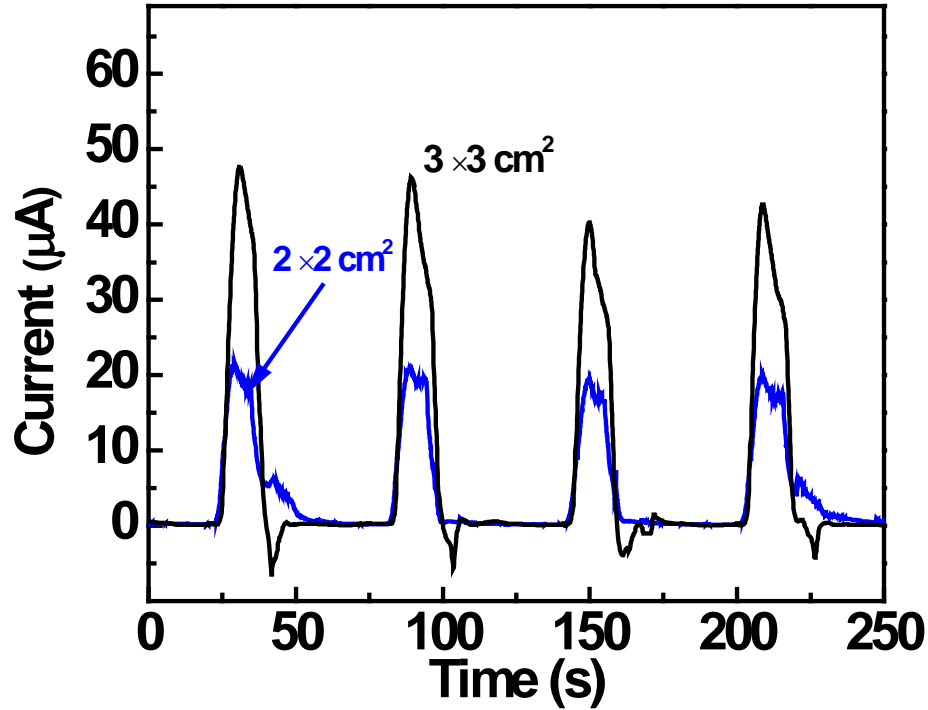


Figure 2-13: Current output of 4 cm² and 9 cm² size devices on thermal cycling

The maximum power output for a single layer (1 cm²) device presented in this work is ~50 nW/cm² when subjected to a temperature difference of around 80 °C at a rate of approximately 5.8 °Cs⁻¹. The response of the composite can be attributed to be a convolution of three different mechanisms. Firstly, the initial increase in the voltage can be attributed to the pyroelectric behavior of ZnO since there was a steep change in temperature. Whereas the stable output after the sample is heated is believed to be essentially due to the other two corresponding factors. First being the temperature gradient between the two terminals; as one side of the harvester is in contact with the hot plate, while the other is exposed to air. The other predominant factor is the local strains created due to the unequal expansion of cellulose and ZnO when the composite is heated.

This results in local strains acting radially outwards in the fibers thereby causing piezoelectric currents from the ZnO thin film.

To confirm that indeed two convoluting effects are responsible for this effect, a long time harvesting test was done. As in real-time applications, instantaneous energy harvesting is not very useful and a continuous power output is always required. To test the device for such applicability, a device with 1cm^2 active material was heated for 30 minutes and the voltage across the terminals measured throughout. The voltage and temperature profile of the result has been plotted in Figure 2-14. It has been observed that as the device is placed on the hotplate, an instant spike in the voltage is observed which can be attributed to the pyroelectric effect as a change in temperature is seen by the composite. After the temperature stabilizes, the voltage drops instantly by $\sim 20\%$ and then the loss in voltage is gradual but slow. The loss in the voltage can be attributed to the system relaxing and also due to resistive losses in the device. After 30 minutes of continuous energy harvesting, the voltage drops by about 30%. The voltage falls to zero when heating is stopped and the device is moved to a cool zone.

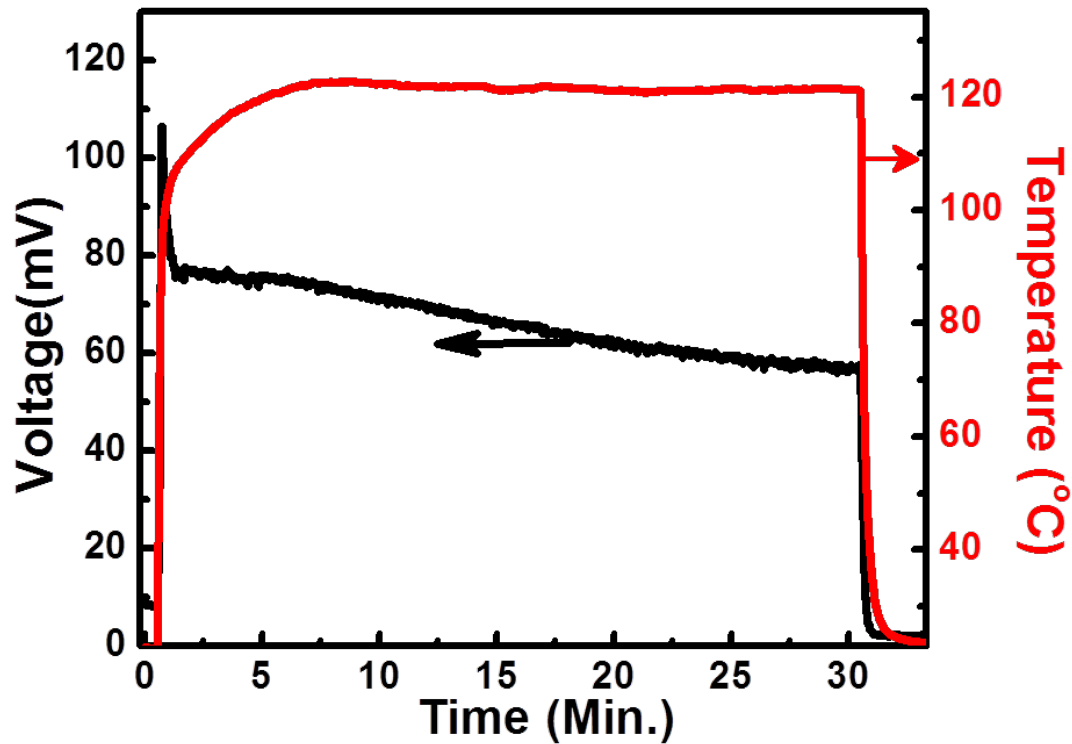


Figure 2-14: Voltage output from a device with 1cm² active material patch, subjected to a continuous thermal heating for 30 minutes

2.5. Strain Sensor for structural health monitoring

In addition to their ability to harvest energy from locally available energy sources, piezoelectric materials can also serve the purpose of detecting change in the mechanical strain. Mechanical strain is a direct and most reliable measure of the mechanical state of the equipment that endure stress and strain during their operational course of action such as down-hole drilling. The ability of the sensor to measure strain along any given direction at any specific location of the equipment and the flexibility of the sensor to

confirm to the contours of the equipment are important desired characteristics in sensors. Being able to accomplish the above mentioned tasks without the need for any power input serves to enhance the reach of the sensors to locations where power accessibility is limited or restricted altogether. Such abilities to detect and monitor real time changes in mechanical strain enables to accomplish tasks such as monitoring drilling conditions^{160,161} and also enables to address more complicated problems pertaining to other industries such as aeronautical, civil infrastructure etc. by aiding in fatigue detection, crack detection and so on.

2.5.1. Experimental details

For the fabrication of a typical composite sensor specimen, a piece of the ZnO-paper ($2\text{ cm} \times 0.5\text{ cm}$) was coated with two gold electrodes, on the surface, separated by a distance of $\sim 0.3\text{ mm}$. For static strain measurements, the specimen was attached to a brass beam (cross sectional area $3.17\text{ cm} \times 0.635\text{ cm}$ with Young's Modulus of 166 GPa) using a thin coat of insulating epoxy. A conventional, commercial grade foil strain gage (Vishay Intertechnology Inc., PA, with a Gage Factor of 2.1) was also attached onto the beam for comparison. Both the strain gage and the composite sensor were oriented along the length of the beam. The brass beam was mounted in an MTS hydraulic testing machine and an axial load was applied to it along its length. Figure 2-15 shows a schematic of the device assembly and a photograph of the brass specimen loaded onto the hydraulic testing machine.

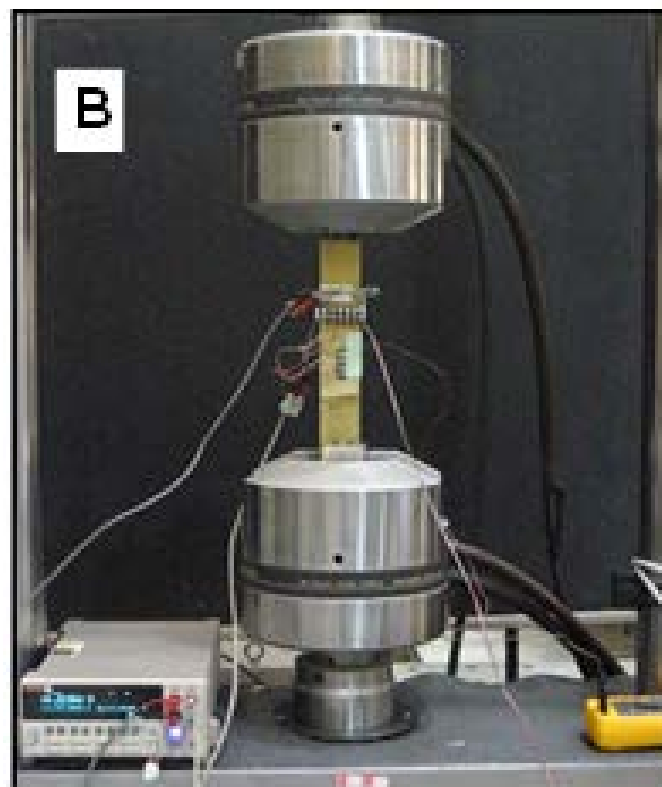
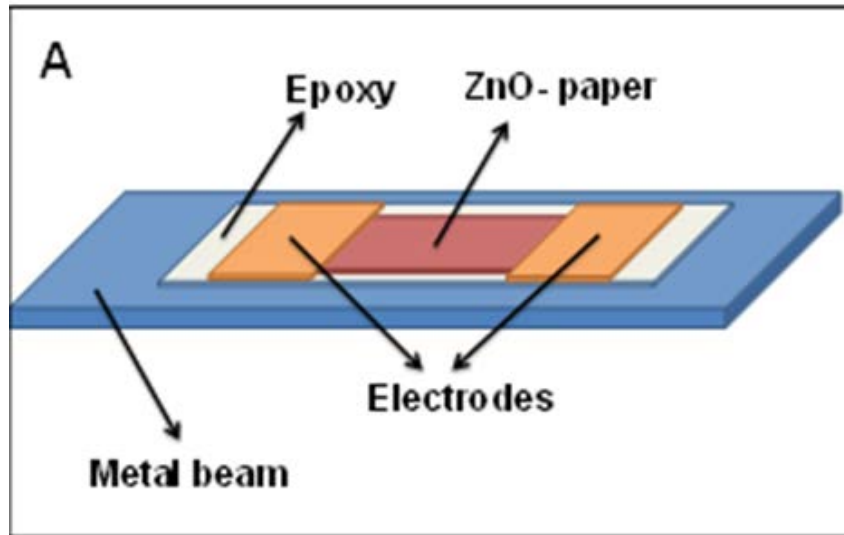


Figure 2-15: Schematic of test device for measuring strain experienced by a metal beam. (B) Photograph of the test setup to measure static strain loading

For dynamical testing and measurement, the ZnO-paper is attached to a 50×0.7 mm² cross-section aluminium strip having a Young's modulus of 69 GPa using superglue as shown in Figure 2-18(a). Another commercial metallic foil strain gauge is attached on the opposite side of the aluminium specimen for strain measurement comparisons. A piezoelectric actuator (from Mide Technology Corporation, MA) is attached to the aluminium specimen to excite the beam at different frequencies for a fixed duration of time. The piezoelectric actuator was actuated using a dSPACE Data Acquisition and control unit in conjunction with a power amplifier. The beam was excited with the external actuator for a range of frequencies.

The performance of the composite sensor to both applied static and dynamic loads were evaluated by measuring its output current using a Keithley Series 2400 Digital Source Meter (with a sensitivity of 10pA and a sampling rate of 100 samples per second) and compared with the strain measured using a commercial foil strain gage. The measurements from the composite sensor was done using insulated/sheathed cables taking care to minimize the influence of surrounding noise on the measurements.

2.5.2. Results and discussion

The I-V characteristic curves of the nanocomposite sensor at different strains indicate a shift with increasing tension and shown in Figure 2-16(A). Figure 2-16 (B) shows the current response from the nanocomposite sensor and the strain reading from the commercial strain gauge for a stepped tensile loading. The behavior of the nanocomposite sensor as it is subjected to constant load is tested by applying tensile load to the specimen in increments of 44.48 kN. It is evident from the electrical response that

the nanocomposite sensor demonstrates a stable response similar to the commercial one. The nanocomposite sensor was tested under cyclic loading in both compression and tension as shown in Figure 2-16 (C). The loading was done at a very low rate and hence, no dynamic effects of the brass beam are observed in the response. A voltage bias of 0.1V was applied to the sensor for the results presented in Figure 2-16. The electrical response from the nanocomposite sensor is found to be in good agreement with the strain measured from foil strain gage for static loading. The nanocomposite sensor behaves in a similar manner in both compression and tension as demonstrated from the response of the sensor for cyclic loading and it is observed that even after repeated cycles, no drift is observed in the response.

The signal to noise ratio is also very high for the response observed. Gage Factor of the nanocomposite sensor can be calculated using the modified formula^[19] as follows:

$$GF = \frac{\frac{\Delta R}{R}}{\varepsilon} = \frac{\frac{\Delta i}{i_f}}{\varepsilon} = \frac{(i_o - i_f)}{i_f \times \varepsilon}$$

Where, ε is the strain applied to the sensor, i_o is the initial current at zero strain, and i_f is the final current at ε strain. From the observed results the gage factor of the nanocomposite sensor was found to be ~21.12 which is comparable to the generally recorded values for commercial strain gauges. The long-time response of the sensor when it is subjected to various static load tests is presented in Figure 2-17, from the response it is clearly evident that the sensors shows consistent performance without any remnant drifts at the end of each successive load test. It is clear indicator of the stable response of the sensor.

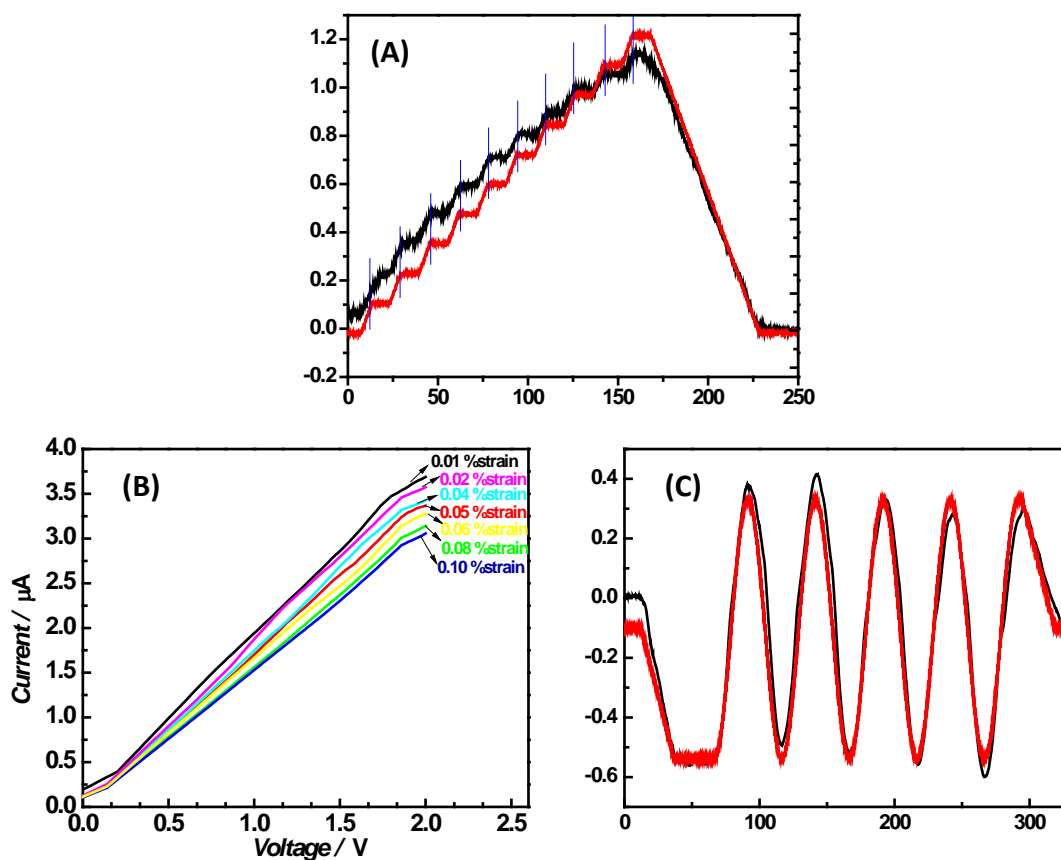


Figure 2-16: (A) I-V characteristic of the ZnO-paper sensor as a function of strain. (B) Response to tensile loading (C) Response to cyclic loading in which a load is cycled equally from compression to tension.

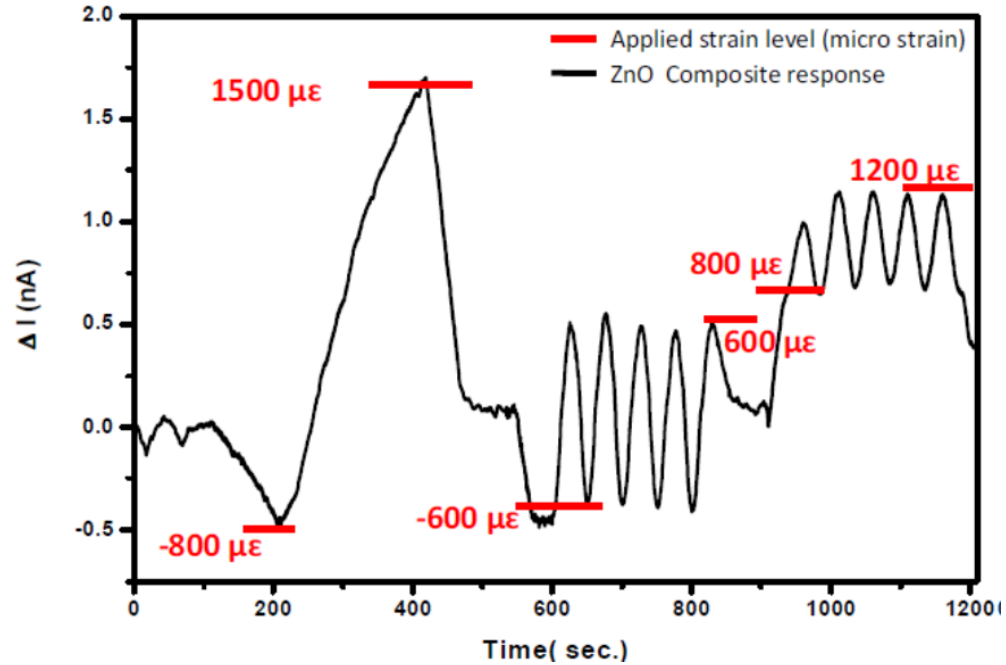


Figure 2-17: Response of the sensor as it is subjected to various static loads continuously

The response of the sensor is also studied for dynamic loading. Figure 2-18 (a) depicts the experimental setup used for such testing. The actuator was excited at various frequencies keeping the excitation amplitude constant and the response of the composite sensor was measured without giving any input voltage to it. The measured response from the sensor at frequencies 0.1, 1, 2 and 4 Hz is presented in Figure 2-18 (b), (c), (d) and (e) respectively. The excitation was given in repeated sets of cycles of sinusoidal waves. The frequency of the response corresponds well with the frequency of excitation; a consistent behavior in the response of the sensor is observed for different frequencies. Figure 2-18 (f) shows a closer view of the response and illustrates the reproducibility under cyclic loading. Also, no drift was observed in the response at the end of each cycle of excitation. The amplitude of the response of the sensor is observed to be increasing with increase in

frequencies because the amplitude of vibration of the beam increases with increasing input frequencies. The first resonant frequency of the beam was observed to be at a value higher than 4 Hz.

The nanocomposite sensor shows good strain sensitivity for deformations in both tension and compression corresponding to the positive and negative peaks of the response. Due to the piezoelectric nature of the nanocomposite, it can be operated without any source power as demonstrated in this test, opening the possibility of self-powered sensors.

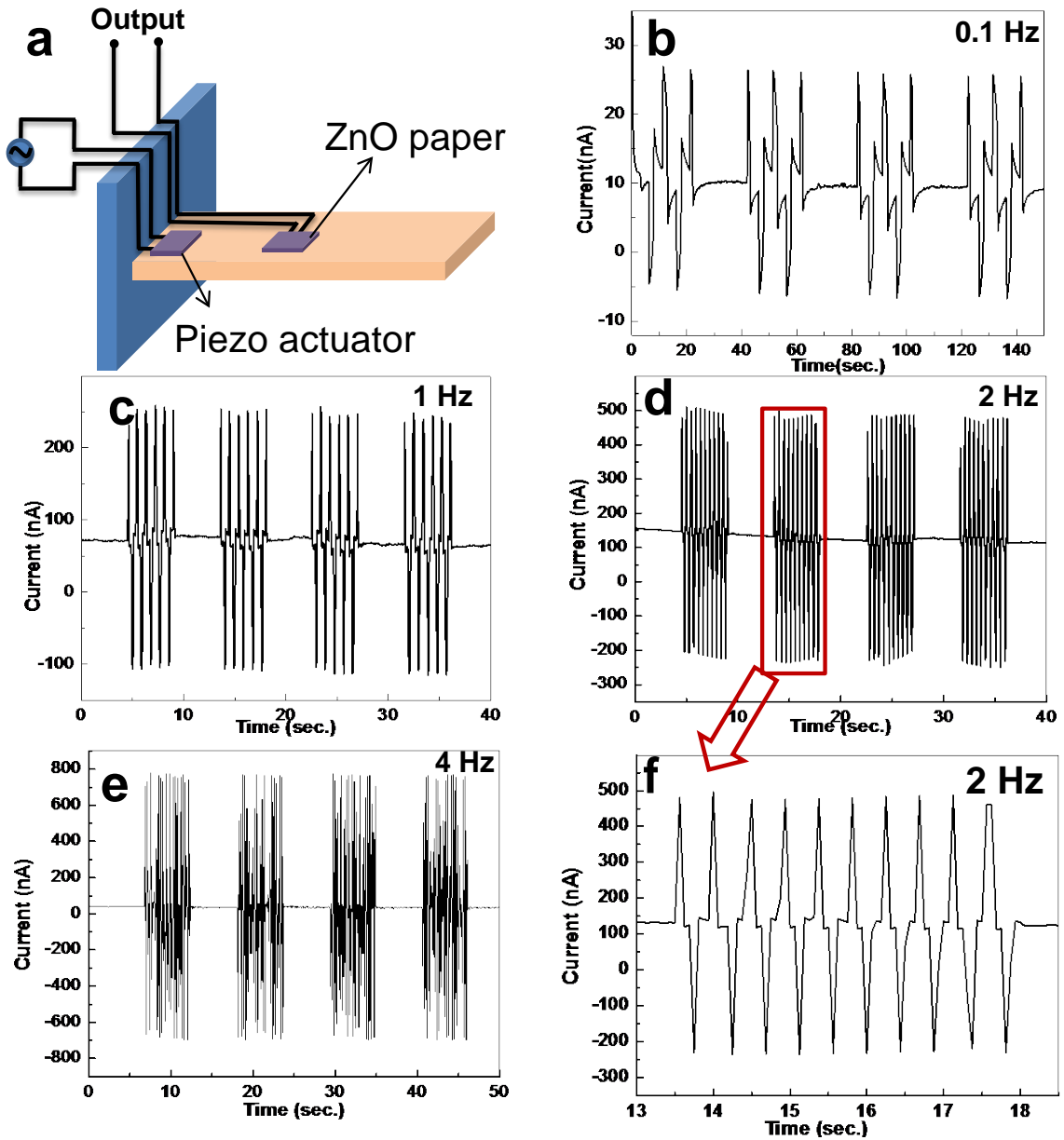


Figure 2-18: (a) Schematic diagram depicting the experimental setup for strain measurement under dynamic loading. (b-f) Dynamic response of the composite sensor on exciting the beam with frequencies (b) 0.1, (c) 2, (d & f) 2, and (e) 4 Hz

2.6. Conclusions

In summary, a simple, scalable system has been developed to synthesise a truly flexible form of piezoelectric composite material. By using the matrix of 'paper' as the structural backbone, ZnO nanostructures were fabricated completely encapsulating the cellulose fibers while still leaving behind the porous nature. The composite material has the convoluted piezoelectric property, like a bulk ceramic material, yet has the retained flexibility from the paper. Energy harvesting from multiple sources has been demonstrated using this material. Harvesting from mechanical vibrations and thermal fluctuations has been studied. Also the use of this ZnO-paper for strain sensing applications is demonstrated. The material is capable of measuring the strain experienced by a host structure when subjected to both static as well as dynamic loading.

Chapter 3

Direct synthesis of graphene on metallic substrates

Recent advancements in Chemical Vapor Deposition (CVD) techniques had facilitated growth of graphene on various metallic substrates such as Ni,¹³² Cu,¹³³ Pd,¹⁶² Ru,¹⁶³ and Ir¹⁶⁴. The nature and crystal structure of the metal determines the growth mechanism and properties of the resulting graphene. Growing graphene on different metallic substrates and understanding its physical and chemical properties is very fascinating. Mattevi et al.(2010)¹⁶⁵ has done a comprehensive review of various reported variations. The CVD technique typically involves heating the substrate at high temperatures under a flow of hydrogen gas and once a set temperature is reached, exposing it to carbon atoms by pyrolysing a hydrocarbon.

The mechanism of graphene growth is dependent on the catalytic substrate it is being deposited on to. Many transition metals have been identified to have catalytic

activity towards carbon, and have been used for the very reason in the synthesis of carbon nanotubes.¹⁶⁶⁻¹⁶⁸ The mechanism of nanotube synthesis involves dissolution of carbon atoms into the crystal structure of metal particles, forming a solid solution. As the concentration of carbon increases, a supersaturated state is reached and the carbon is precipitated out, thereby graphitizing into nanostructures.¹⁶⁹ The essential characteristic of the catalyst is its ability to have sufficient solubility of carbon. While Iron has high solubility of carbon due to its ability to form various phases of stable carbides, it has been the prime choice for CNT growth. Cobalt and Nickel follow next in solubility while copper has negligible solubility, as it does not form any carbides.¹⁷⁰ However copper can form weak π bonding on its surface with carbon atoms at high temperatures.^{165,171}

For applications involving graphene, the most sought after properties are layer control and continuity over large area. Extrapolating the process of CNT growth, controlled fabrication of graphene has been first reported on Nickel substrates.¹³² The solubility of carbon in nickel is temperature dependent and the phase diagram of carbon-nickel system is shown in Figure 3-1(a). While the solubility is rather high at temperatures greater than 1360 (melting temperature), it is linear until about 800 °C and is under 0.6%. The solubility sharply drops at lower temperatures. Nickel forms carbides at high temperature which when cooled down separates back to pure metal and carbon. If a smooth surface of nickel is heated in a carbon rich environment, a solid solution is formed and during cooling, carbon would precipitated out. By controlling the cooling rate, the amount of carbon that surfaces out can be limited thereby forming continuous graphene on the surface. The layer control in such a process is however very difficult as

the rate of diffusion of carbon is hard to control. Single layered continuous graphene is therefore challenging to achieve using such an approach.

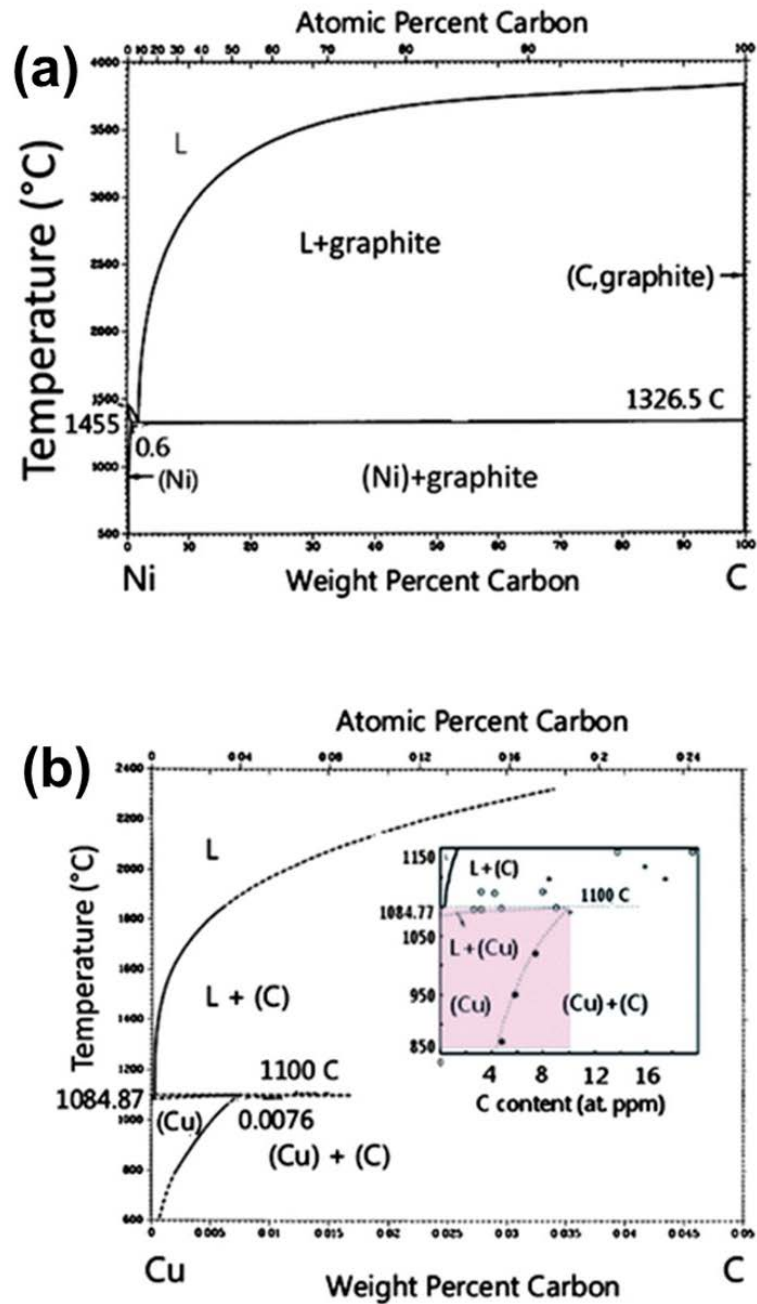


Figure 3-1: Phase diagrams of (a) Nickel-Carbon system (b) Copper-Carbon system.
Adapted from ref [165]

On the contrary, Copper has negligible solubility of carbon as seen from the phase diagram in Figure 3-1 (b), but does have a weak π interaction on the surface. Exploiting this property, large area single layer graphene has been realized thru CVD deposition onto copper foils.¹³³ Since the interaction between copper and carbon is surface a mitigated one, the growth is a self-limiting process.

Li et al(2009)¹⁷² have conducted a comprehensive study on the growth mechanism of graphene through carbon isotope labelling, which helps in better understanding of the process. By using Raman spectroscopy as a tool for identifying the different energies possessed by the isotopes of carbon, they have mapped the process of graphene formation in both copper and nickel substrates. By passing two different isotopes, ^{12}C and ^{13}C , in sequence during the growth of graphene, they have time mapped their presence in the structure. It was revealed that in the case of nickel, due to the solid solution and perspiration mechanism, the isotopes are dispersed in a random fashion in the graphene structure. However, in case of copper, the two isotopes have been identified to be concentrated in regions. While the first introduced ^{12}C atoms occupy the nucleation sites, mostly at the centers of the grain boundaries the later introduced ^{13}C atoms are concentrated on the edges of the grains. This confirms that the mechanism indeed is a surface phenomenon, and follows a nucleation and growth process. The schematic representation of the observation is shown in Figure 3-2, reiterated from the manuscript.¹⁷² This elegant experiment evidently proves the two varying processes for graphene formation.

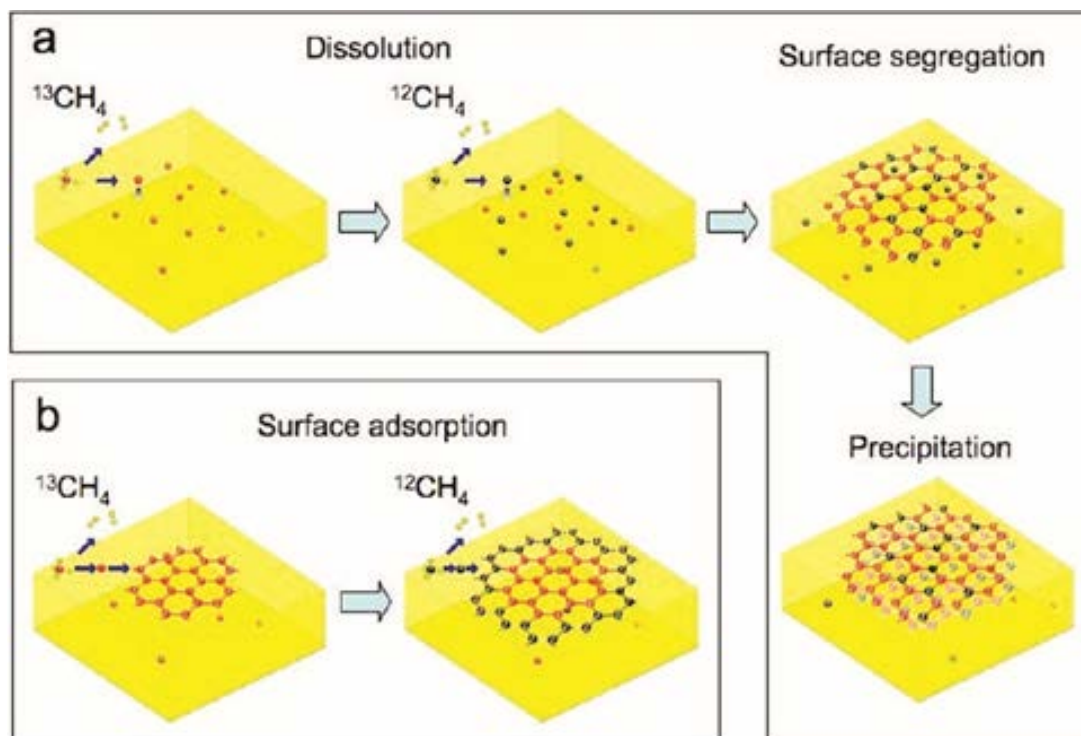


Figure 3-2: Schematic diagrams of the distribution of Carbon isotopes based on different growth mechanisms (a) on nickel (b) on copper (adapted from ref [172])

While most of the initial reports of CVD process for graphene have employed gaseous precursors, liquid and solid carbon sources have also been explored.^{173,174} While gas has an advantage of avoiding contaminants and ease of measuring the flow, selectively modifying its ingredients to explore possibilities such as doping would be difficult, complete pyrolysis also needs temperatures upwards of 1000°C. Liquid based precursors have been used as an alternative and have advantages such as lower pyrolysing temperatures and ease of mixing dopants into the system. A formulation for use of Hexane as the carbon source has been developed and reported by Srivastava et al.(2010)¹⁷³ where in graphene growth onto copper foils has been achieved at a temperature of 950°C. While all reports using gases such as methane or acetylene have a

growth temperature of 1000°C, which is close to the melting point of copper, lowering the temperature in case of liquids adds robustness to the system. Employing this technique and using different types of liquid organic substances as carbon precursors, different variations of graphene based structures on catalytic substrates have been realized and discussed in this thesis.

An experimental setup equipped with the flexibility to change the type of source and substrates has been built and optimized. Building on the reported technique of liquid precursor pristine graphene growth, as it gives the flexibility of introducing dopants in the system, nitrogen doping of graphene has been explored. The lower temperature required for pyrolysis of liquid precursor also opens up doors for using other substrates which might otherwise cannot be used. Alternative to pure metals, metallic alloys have been reported to form graphene using this liquid source CVD. Finally, while conventional CVD synthesis techniques do not modify the structure of the substrate, by employing suitable chemical groups, the substrate has been engineered into useful structures, while still forming graphene on the surface. Parts of this chapter have been reported in two publications, Reddy et al. (2010)¹⁷⁵, and Gullapalli et al. (2011)¹⁷⁶

3.1. General Experimental Setup

Liquid source Chemical Vapor Deposition (CVD) technique has been employed for developing graphene materials on various metallic foils. The photograph of the experimental setup is shown in Figure 3-3 and the corresponding schematic depicting the drawing of the tubing and the various fittings is shown in Figure 3-4. Split-Hinge Tube Furnaces with a single zone heating element capable of heating up to 1200°C was used,

along with a programmable temperature control module (from Thermo Scientific/Lindberg Blue). Quartz tube of dimensions 50mm OD, 47mm ID and 4 feet in length was fitted at its ends with vacuum sealed flanges and used as the heating chamber in the furnace. One end of the tube was attached to a vacuum pump (oil rotary type, ultimate pressure rating of 6.7×10^{-2} Pa). An inline pirani pressure gauge and a cut off valve (V6) are also attached between the pump and the quartz tube.

On the other end of the quartz tube, gas tubing inputs were attached. Two independent tube lines are attached to the quartz tube, one of which is connected to inert gas inlets through an on/off valve V1 and a regulator needle valve R1. A switch valve S1 is connected which can be switched between either ultra-high purity argon connected to inlet I1 or 15% mixture of hydrogen in argon connected to inlet I2.

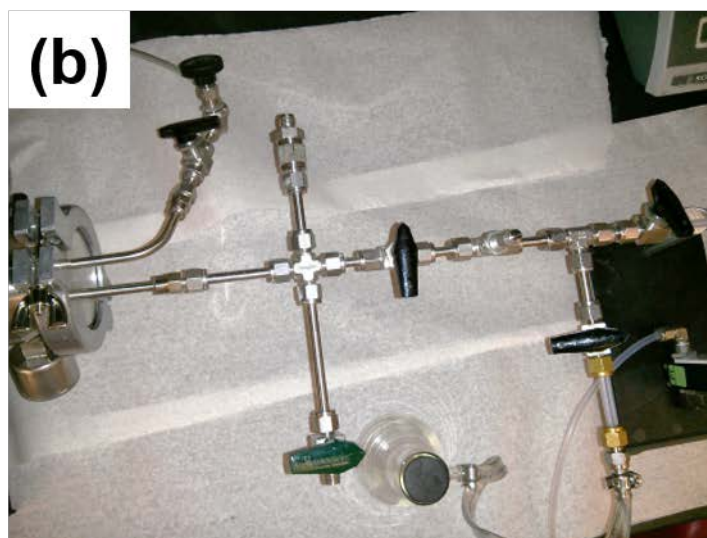


Figure 3-3: (a)Photograph of the Chemical Vapor deposition setup. (b) Photographh of the tubing at the inlet side, multiple inputs can be independently controlled with the valves

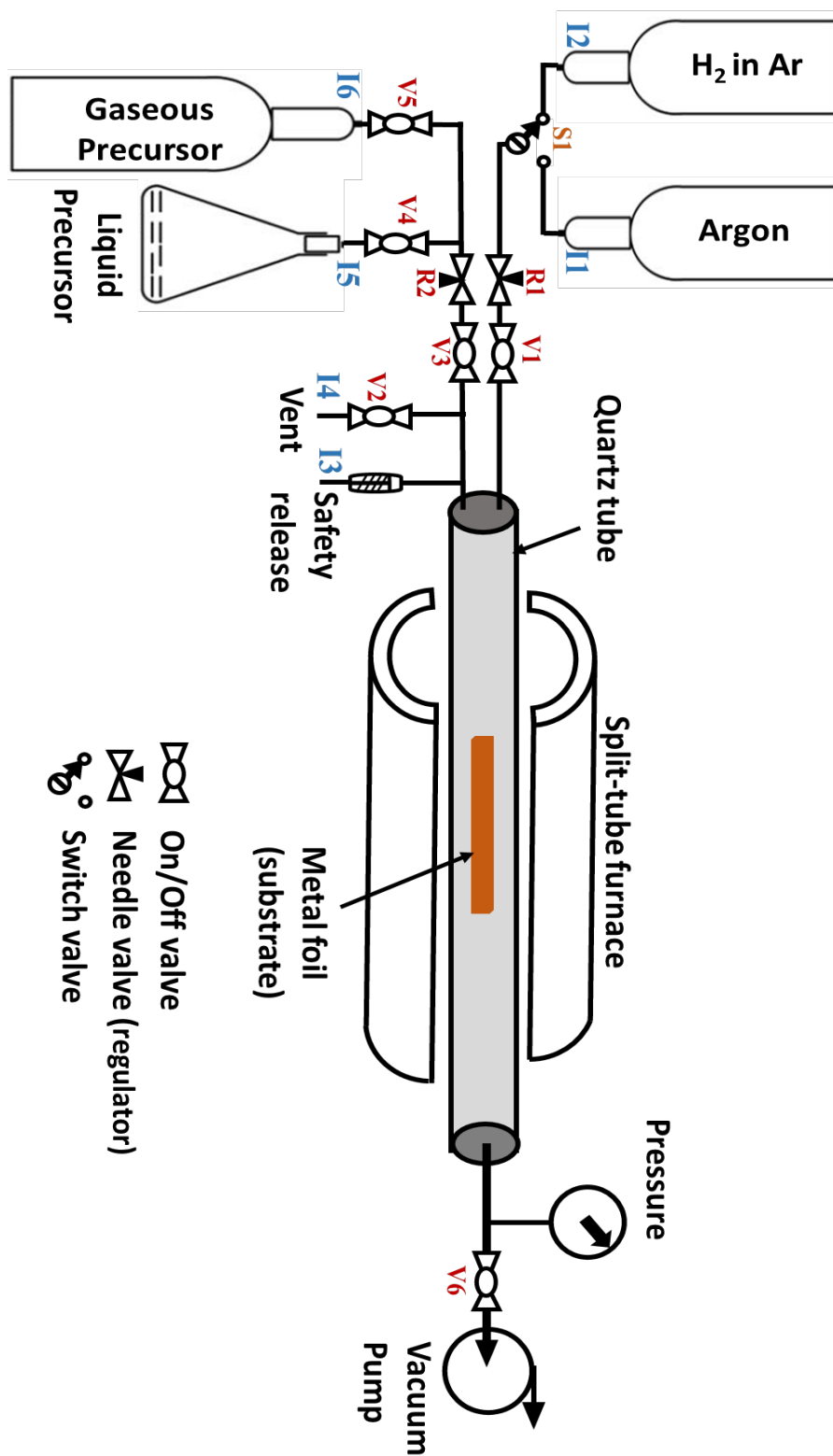


Figure 3-4: Schematic blueprint of the chemical vapor deposition setup, equipped with a vacuum feature and has both liquid and gaseous inputs

The second gas line, called the source line, has four inlets connected in series, each inlet can be independently turned on or off. The first inlet (I3) is connected to a safety pressure release fitting which is set to trigger and vent the tube in case of accidental over pressurization the second inlet (I4) is the vent/purge provision, controlled through an on/off valve V2. The third input (I5) is used as a liquid source input connected to a 1L capacity Büchner flask containing a few ml of appropriate chemical solution with its mouth closed using a rubber stopper. The last input (I6) is reserved for gas inputs connected to appropriate cylinders through a mass flow meter. The last two inputs (I5 and I6) are connected through an on/off valve (V2) and a high precision regulator needle valve (R2). The setup is planned in such a way that the inert gas input is not contaminated by the chemicals in the source line. And the last two inputs in the source line can be used either independently, sequentially or mixed together as demanded by the process. The vent connection can also be converted into an additional source input if need be.

Before the setup could be commissioned, a leak proof test has been conducted. First, all the valves and regulators have been closed and the vacuum pump turned ON. The valves starting from the vacuum pump are opened in sequence towards the inlets, while monitoring the pressure reading in the pirani gauge. V6 is first opened slowly and the pressure is allowed to reach the base value of about 2×10^{-2} Torr, if the pressure is not reached, any plausible leaks are checked for. Valves R1, R2, V1 and V2 are then opened to check for any leaks in the tubing. It has to be noted that R2 being a high precision needle valve, should not be completely closed and is not advisable to be exposed to high vacuum while closed. Hence to protect it, it is opened first before V3. As the base pressure is reached again, the chamber is purged with all the gases from inputs I1, I2 and

I6 one after the other, so as to remove any trapped oxygen in the lines. Finally, the flask at input I5 is evacuated by opening valve V4. As any liquid precursor would contain dissolved gases in it, the flask is pumped down until the pressure is stabilized in the chamber. A stable pressure indicates the vapor pressure of the liquid. Though not used in the context of this thesis, the contents in the flask can be slightly heater or stirred using a magnetic stir bar, if any recipe calls for. This adds to the flexibility of the system, where customizations in the precursor can be done using chemical routes. Once every stage of the system has been checked for leaks, recipes involving heating cycles, exposure times and cooling rates can be run on it.

In a typical fabrication process, a desired substrate is inserted into the quartz tube and the ends are closed. The tube is first evacuated to its base pressure, care needs to be taken not to expose the setup to any sudden pressure shocks. For that reason, the vent valve V2 is set to open and the vacuum valve V6 on the outlet side is set to close before the vacuum pump is turned on. Once the pump is turned on and running, valve V6 is opened and then V2 is closed slowly. This process avoids any sudden movements in the tube, avoiding damage to both the samples inside and the quartz tube itself. To ensure that the setup is leak free, the tube is pumped down to the base pressure with all the input source valves (V1 to V5) closed. The typical base pressure observed after pumping down for 10 minutes is in the order of 8×10^{-3} Torr to 1×10^{-2} Torr. Once the base pressure is reached, the growth recipe is followed depending on the required structure and described in subsequent sections. To vent the chamber, valves V1 and V3 are first turned close followed by V6. The valve V2 is opened slowly to vent through Input I4.

3.2. Graphene growth on copper substrates using liquid precursor

The process for using liquid precursors for the growth of graphene was first developed and reported by a team of colleagues, Srivastava et al.(2010).¹⁷³ To perform a comparative study of various other forms of graphene developed in the scope of this thesis, the reported procedure has been followed to synthesize pristine one to two layer graphene samples onto copper foils using the setup described in section 3.1.

3.2.1. Fabrication procedure

Hexane was taken as the carbon precursor in the flask at input I5. High purity hexane (HPCL grade, mixture of isomers) has been used to avoid any contamination. No precursor was used at Input I6 and the valve V5 was kept closed at all times. Copper foil (Basic copper Inc., 1 mil thick) cut into a size of about 3cm x 5cm has been inserted into the quartz tube and ends closed. After the quartz tube has been evacuated, the hexane flask was also pumped down until a stable pressure of about 7×10^{-1} Torr has been reached. The heating profile and corresponding gas flows have been followed according to the recipe depicted in Figure 3-5. The furnace was heated to 950°C in 30 minutes, while flowing H₂-Argon mixture gas. The inputs I5 and I6 have been isolated during the heating by closing valve V3, while the pressure in the tube was controlled to be at 10Torr using the regulator valve R1 with valve V1 kept open. Once the set temperature is reached, Ar/H₂ flow was cut off by closing valve V1 and hexane vapors were passed by opening valves V4 and V3. The flow was regulated using needle valve R2 so that the pressure in the chamber is maintained at 0.5 Torr. After 4 to 8 minutes of hexane flow, the furnace was turned off, and allowed to cool by opening slightly the top half of the

furnace and wedging it. Once the temperature falls to 800°C, hexane flow was stopped using valve V3 and Ar/H₂ flow reinstated by opening Valve V1, until completely cooled.

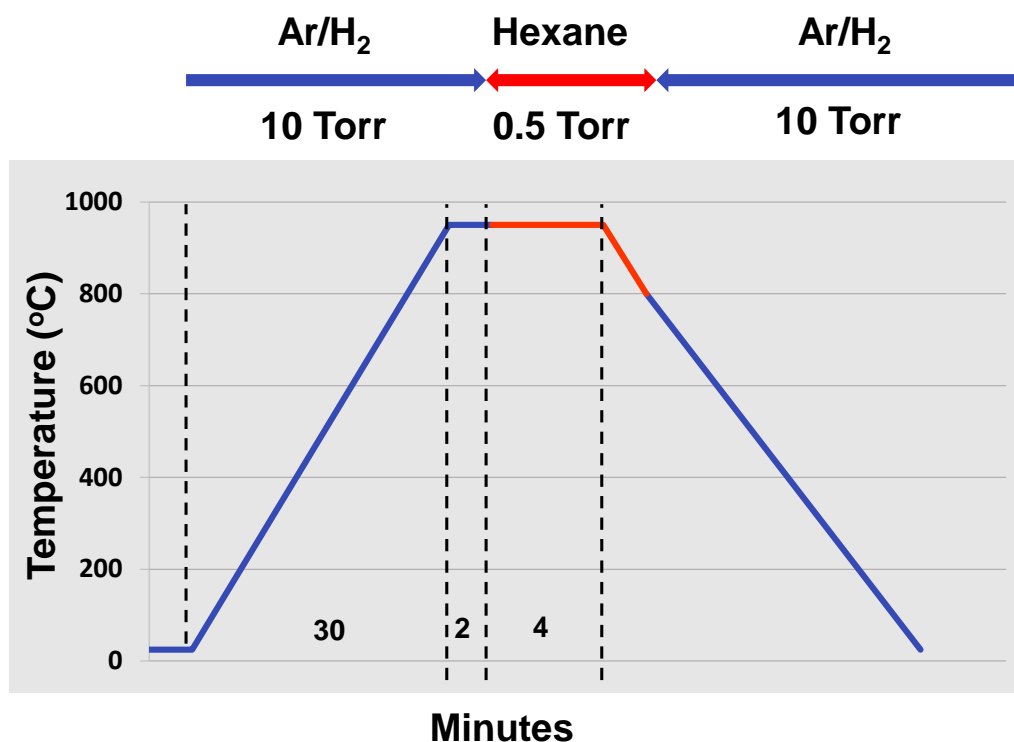


Figure 3-5: Recipe for graphene growth on copper substrates. 4 minutes of hexane exposure at 950°C results in one layer graphene, while 8 minutes yields 2 to 3 layers

3.2.2. Characterization

In order to characterize the quality of graphene, the thin two dimensional structure needs to be transferred on to other substrates without damaging its physical structure. For doing so, a convolution of reported procedures,^{133,177} involving polymer lift-off technique has been used. The process involved is schematically described in Figure 3-6 and starts with spin coating onto the graphene coated copper foil, a thin layer of

polymethyl methacrylate (A4 grade PMMA from Microchem) using a spin coater at 2000 rpm for 30 sec. the sample is then baked on a hot plate at 80°C for 30 seconds. Once dry, the other side of the copper foil is cleaned by gently wiping it with an IPA soaked tissue paper. The foils are then floated, with the PMMA facing up, on to diluted Marbles reagent (10g CuSO₄, 50ml Hydrochloric acid and 100ml Water) for 6 hours. Once the copper completely dissolves, the floating graphene-PMMA is carefully lifted using a clean glass slide and transferred into a bath of DI water. The graphene is then lifted on to the required substrate and allowed to dry. Proper cleaning of the substrate is critical for good adhesion of graphene. For substrates like silicon or glass, a Piranha cleaning procedure or even slight plasma cleaning greatly increases the adhesion.¹⁷⁷ The substrate is heated on a hot plate set to 120°C for 5 minutes to remove any traces of water. The sample is then dropped with a drop of fresh PMMA to soften the existing PMMA, this step helps in flattening the wrinkles formed due to the physical transfer and during water evaporation. The PMMA is then washed with drop wise dripping of acetone on to it. A final wash with Isopropanol Alcohol removes traces of dissolved polymer.

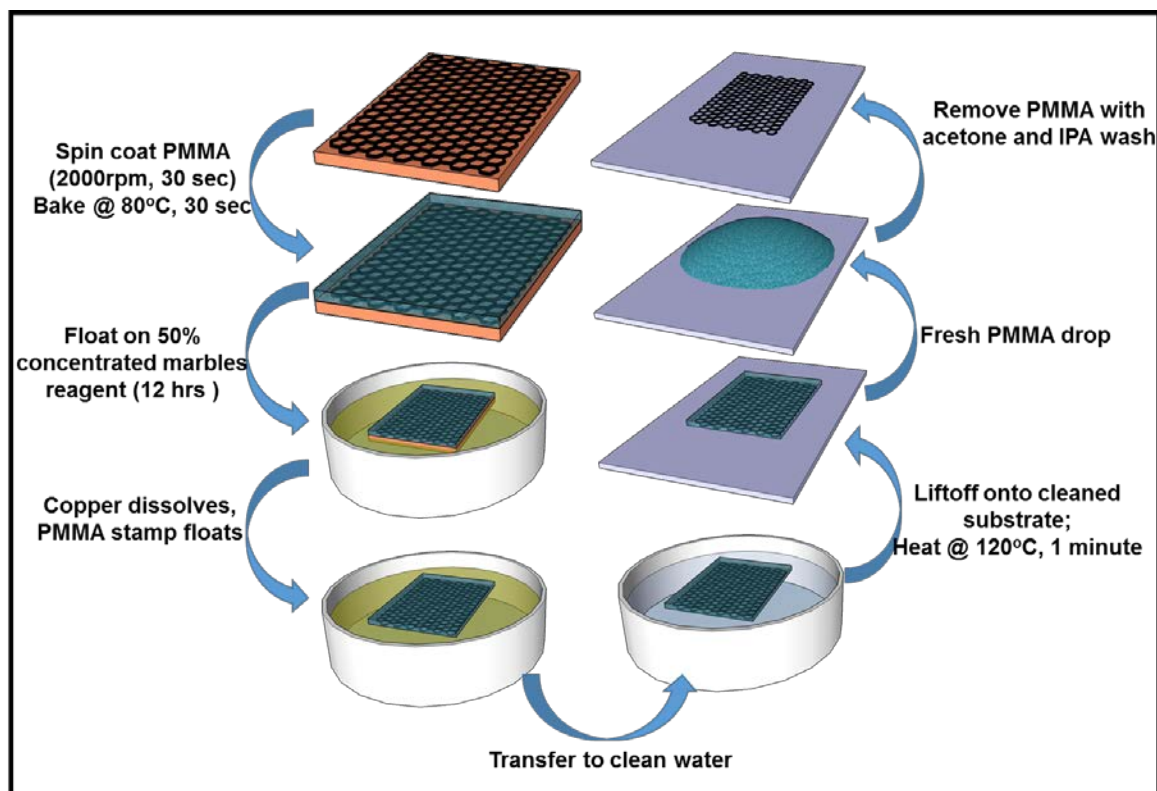


Figure 3-6: Schematic sketch of polymer lift-off technique used to transfer graphene from metallic substrates onto other substrates

Graphene fabricated with an exposure of 4 minutes and 6 minutes of hexane vapors on to copper foils has been transferred on to Silicon wafers with 300nm of thermal oxide on the surface. Raman spectra of the two samples is plotted in Figure 3-7.

Negligible intensity of D peak centered at ~1250 confirms the graphene to have minimal defects in the crystal structure. By comparing the ratios of G peak centered at ~ 1600 and the 2D peak at ~ 2700, the number of layers in the samples can be deduced. With a G: 2D ratio of 0.28, the sample fabricated with 4 minutes of hexane exposure can be deduced to have a single layer graphene. The sample made with 6 minutes of exposure has 2 layers as the G to 2D ratio observed is 0.56.

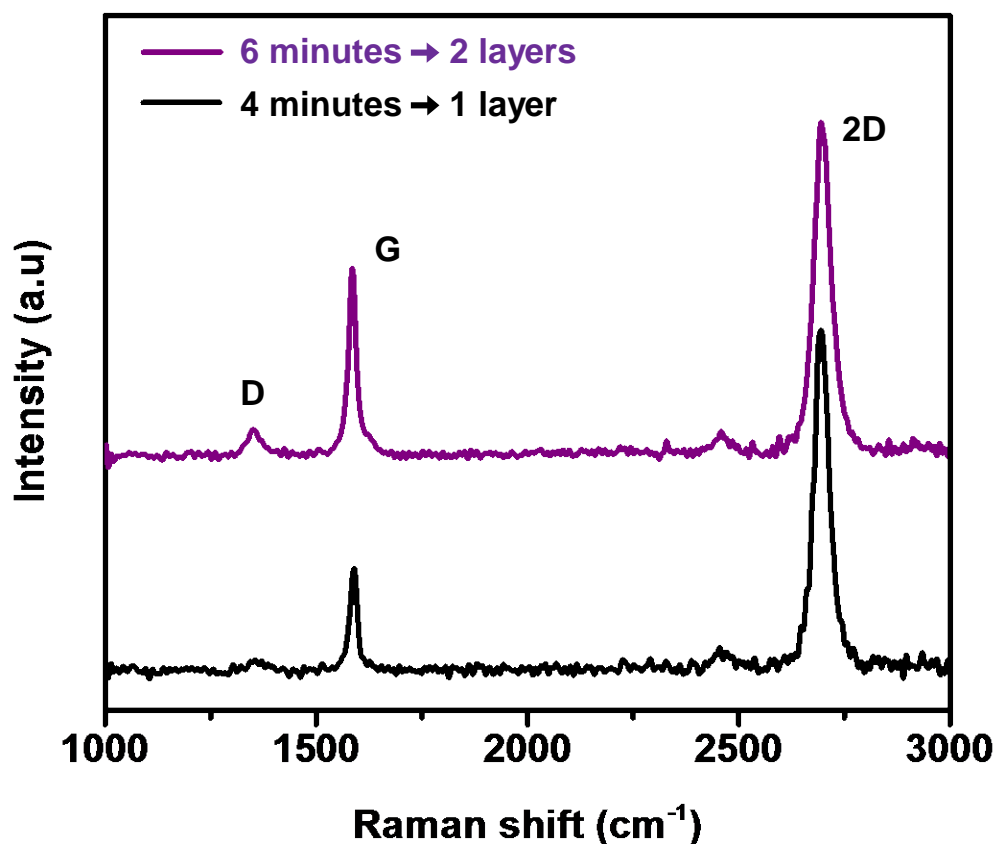


Figure 3-7: Raman spectra of graphene grown on copper foils with Hexane vapors as the precursor using CVD technique

3.3. Nitrogen doped Graphene on copper substrates

3.3.1. Fabrication procedure

For synthesis of Nitrogen doped graphene, the CVD system was connected with 5% ammonia mixture in argon gas to the input I6 and acetonitrile was used as the source precursor in the Büchner flask at input I5. Copper foil of 1mil thickness was cut into a piece of 2cmX5cm. Care was taken to avoid any wrinkles and obvious contaminations

on the surface, if required, the samples were cleaned with IPA and blow dried with dry air. The copper piece was inserted into the quartz tube of the CVD furnace which was then evacuated to its base pressure. The flask, and all the tubing were also evacuated by opening the appropriate valves until a stable pressure reading is observed in the pressure gauge. The stable pressure is a result of the vapor pressure of acetonitrile which confirms the removal of most of the soluble gasses in the liquid. Once the system was pumped down, the source line is isolated by closing the valve V2 and Ar/H₂ mixture was passed by turning S1 to I2 and opening V1 and . The flow was adjusted using valve R1, so that the pressure in the chamber reads 10Torr. The furnace was then heated to 950°C in 30 minutes. As the copper has an intrinsic oxide layer on it, hydrogen gas and high temperature would reduce it and this also anneals the sample. After the temperature is stabilized, Ar/H₂ was stopped (close V1) and acetonitrile vapors were allowed to pass (open V3 and V4) while maintaining a pressure of 500mT. Control over the flow of vapors is achieved through the high precision needle valve R2. The duration of vapor flow dictates the number of graphene layers present in the resultant structure. One to few layer graphene is generally obtained with a flow time of 3 to 15 minutes. After the desired time, the precursor flow is stopped by closing valve V4 and the ammonia gas was flown at a pressure of 5 to 10 Torr by opening valve V5. The furnace was then turned off and allowed to cool. The growth parameters (temperature profile, Precursor and ammonia gas flow rates and system pressure) is graphically shown in Figure 3-8.

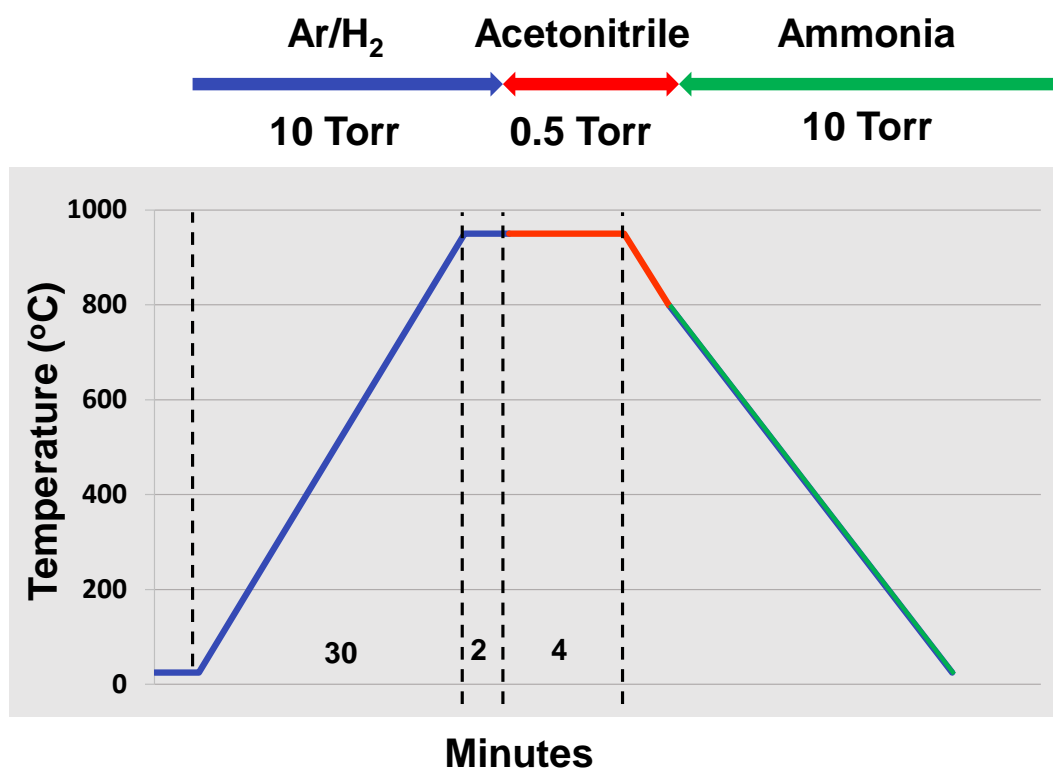


Figure 3-8: Recipe for nitrogen doped graphene growth on copper substrates. Ammonia is flown while cooling the chamber

3.3.2. Characterization

The layered structure of the N-doped graphene has been observed using Transmission Electron Microscope after transferring it onto a holey carbon coated gold grids. The micrograph in Figure 3-9 shows the edge of one of the samples. The layered structure of the graphene with three crystalline layers can be clearly observed. Raman spectra of the graphene transferred on to a silicon substrate is used to characterize its atomic structure and the corresponding plots for different growth durations are plotted in Figure 3-10. The D peak at 1356cm^{-1} is associate with the defects in the otherwise perfect

structure of graphene. The noticeable D peak and the shoulder in the G peak in the plots here is a result of the Nitrogen doping in the structure. Moreover, the peaks at about 1587 cm^{-1} (G-band) and 2697 cm^{-1} (the 2D band) are characteristic to graphitic carbon and their intensity ratios defines the number of layers present in the graphitic structure.¹⁷⁸

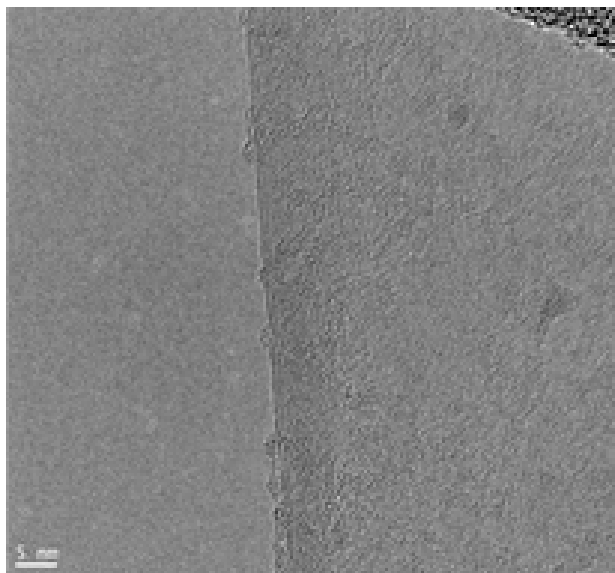


Figure 3-9: Transmission electron micrograph image of a nitrogen doped graphene with 3 layers. The layers can be distinguished at the edge of the sample.

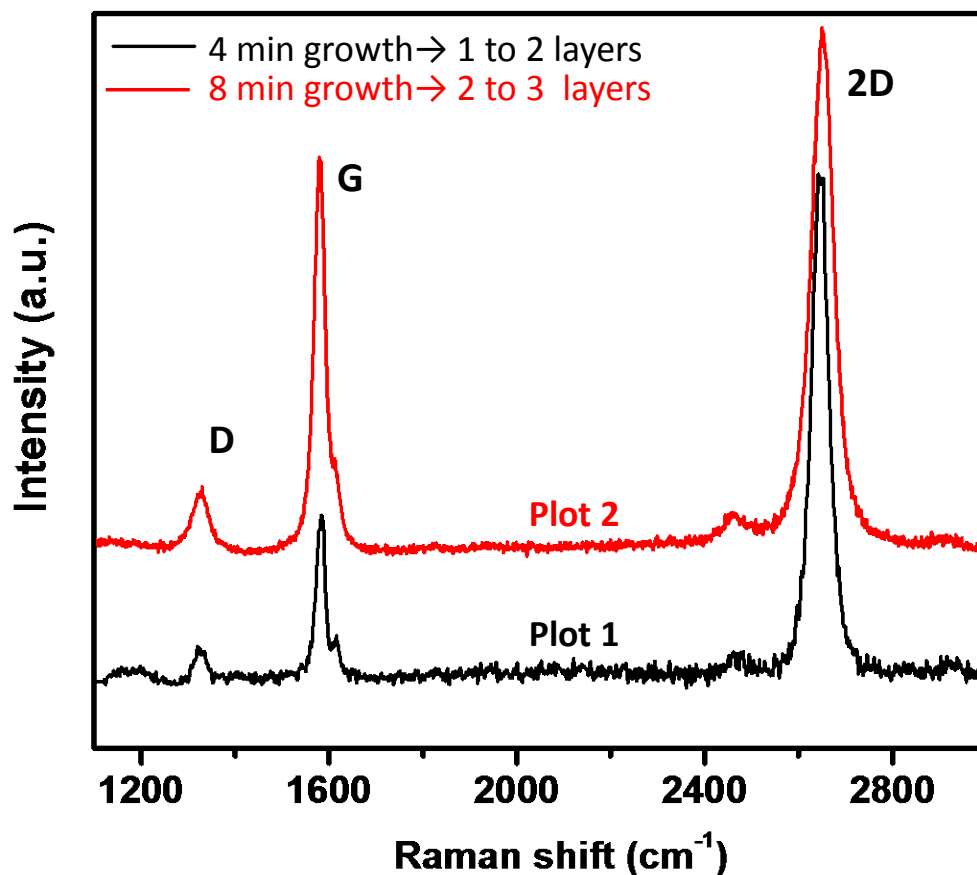


Figure 3-10: Raman spectra of nitrogen doped graphene. 4minutes growth yields 1 to 2 layers while 8minutes results in 2 to 3 layers

By calculating the intensity ratios of the G and 2D peaks, sample with 4 minutes growth shown in Figure 3-10(Plot-1) can be deduced to have just one layers as the intensity of G is less than $1/3^{\text{rd}}$ to that of 2D. The sample with 8 minutes growth and shown in Figure 3-10(Plot-2) has 2 to 3 layers in it corresponding to an intensity ratio in between $1/2$ to $2/3$. This confirms the layer dependence on the duration of precursor exposure during the fabrication process.

To confirm the N-doping of graphene and evaluate the nature of the dopants, X-ray photoemission spectroscopy (XPS) studies were carried out. The survey scan spectrum from XPS analysis showed the presence of the principal C1s, O1s, and N1s core levels with no evidence of impurities (Figure 3-11 (a)) and atomic percentage of nitrogen doping was measured to be about 5%. The spectrum was corrected for any background signals using the Shirley algorithm¹⁷⁹ prior to curve resolution.

The elemental scan of C1s core level peak is shown in Figure 3-11(b) this peak can be resolved into three components centered at ~284.9, 285.5, and 286.5 eV represents sp²C-sp²C, N-sp²C and N-sp³C bonds respectively. Similarly N1s peak shown in Figure 3-11 (c) can also be resolved into three components centered at 399.1, 401.2 and 402.7 eV representing pyridinic, pyrrolic and graphitic type of N atoms doped in the graphene structure, the intensity ratios of these peaks further indicate having higher concentration of pyridinic nitrogen followed by pyrrolic and then graphitic nitrogen. Following these characterization, the structure of the nitrogen doped graphene has been schematically represented in Figure 3-11 (d). The grey spheres represent carbon atoms, blue spheres graphitic N atoms, orange spheres pyridinic N atoms and pink spheres represent pyrrolic N atoms.

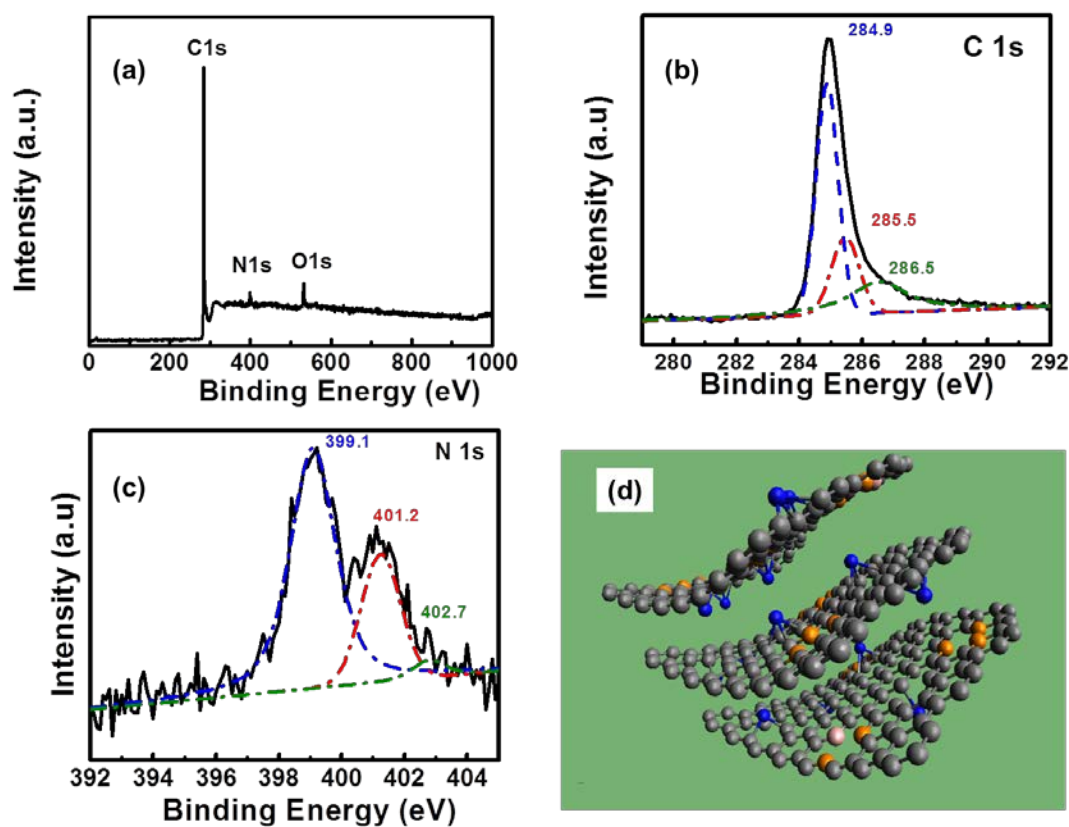


Figure 3-11: (a) Survey analysis of Nitrogen doped graphene, quantifying the chemical composition using X-ray photoemission spectroscopy (XPS) technique. (b) Higher resolution scan of carbon peak, with deconvoluted components. (c) Higher resolution scan of Nitrogen peak, with deconvoluted components (d) Schematic rebuild of the presumed structure as evident from the XPS results

3.4. Graphene growth on stainless steel substrates

As described above (page 58), the growth of graphene on metallic substrates has been identified as either of two processes, depending on the metallic substrate used. One being, physical adsorption on the metallic substrate as the case in copper while the other being diffusion into the bulk of the solid and later precipitation during cooling, as is the case in Nickel substrate. However, both copper and nickel not being stable either

thermally, chemically or electrochemically, certain applications require transferring graphene onto other stable metallic substrates. This always results in physical defects and contact resistance. Direct growth on stable substrates can overcome this problem and can be favorable for many applications, such as energy storage, where good electrical contact is essential for better performance. The major problem with controlling the number of graphene layers during the growth on metallic substrates like nickel is its high carbon solubility and rapid segregation from the nickel carbide during cooling. By exploring other substrates with lower carbon solubility, control on the rate of graphene growth can be achieved. All transition metals which exhibit catalytic activity have either a minimal solubility close to that of Nickel or are inert towards carbon as the case of copper and gold. Substrates having solubility in between these extremes would facilitate a better layer control of graphene growth. Moreover, lattice mismatch between the metal catalyst would need to be $<1\%$ to that of graphene. However, intermetallic alloys which have better properties than pure metals and having the required solubility have not been explored as candidates until now and explored here.

Steel is formed by alloying Iron and carbon. Different grades of steel, each with different chemical and mechanical properties, are realized by controlling the amount of carbon in the structure and depends on the cold work conditions. The carbon content is often considered as the reason for corrosive nature of steels. However all forms of steel have high solubility of carbon in them with an exception of stainless steel grades. Stainless steel differs from carbon steel by the amount of chromium present in them. By alloying iron with a combination of chromium, nickel and molybdenum, different types of stainless steels have been realized.¹⁸⁰ Of these, Austenitic stainless steels are of a

special class in which the face-centered cubic structure is stabilized by adding sufficient ratio of nickel to the structure. These highly durable structures have a maximum solubility of 0.15% of carbon which can be advantageous if explored for graphene growth.

Carburizing is a well-known process developed decades ago in the steel industry and is used to case harden steel using a low quantity of carbon. In this process, steel is introduced to a carbon rich environment at elevated temperatures for a certain amount of time and then quenched so that the carbon is locked in the crystal structure. It will be of fundamental interest if the dynamics of this carbon atom diffusion and kinetics can be slightly modified in order to achieve few layers of graphene on stainless steel substrates. Though the carburization process is similar to chemical vapor deposition (CVD) technique which is generally used for the growth of graphene on metals such as copper, the duration of heating, diffusion and cooling steps are the key in determining the carbon structure that finally forms on the substrate.¹⁸¹

The solubility of carbon in austenitic stainless steel has been well studied and documented. Since these steels were specifically designed to have low carbon content, are usually soft. Various compositions of stainless steels exists, primarily with a varying ratios of Cr and Ni content in them. Rosenberg and Irish (1952)¹⁸² have compared three reports¹⁸³⁻¹⁸⁵ from early studies on the solubility of carbon in austenitic stainless steel with 18% Chromium and 10% Nickel content. Figure 3-12 is an extract from the article which tabulates the reported values of carbon solubility as a function of temperature, according to various investigators.

Temperature ° F	Percentage of carbon soluble in austenite—			
	18-percent- Cr-8-per- cent-Ni ^[183]	18-percent- Cr-8-per- cent-Ni ^[184]	18-percent- Cr-9-per- cent-Ni ^[185]	18-percent- Cr-12-per- cent-Ni ^[184]
1,400-----	<0.02	-----	-----	-----
1,500-----	.025	-----	-----	-----
1,600-----	.045	-----	-----	-----
1,700-----	.075	0.05	0.07	-----
1,800-----	.12	.10	.12	0.08
1,900-----	.18	.17	.17	.16
2,000-----	.23	.26	.24	.25
2,100-----	-----	.38	.32	.38
2,200-----	-----	-----	.41	-----

Figure 3-12: Solubility of carbon in chromium-nickel austenite according to various investigators. (adapted from [182])

From these reports, it can be inferred that the solubility of carbon is very low (< 0.07%) until a temperature of 1700°F in all the reports. Also, steels with a larger concentration of Ni (12%) had slightly lower solubility. It should be noted that these reported values are for conditions where the steel was exposed to carbon atmosphere for a prolonged time, usually weeks so as to saturate the solid. In case for graphene growth, the exposure time can be minimum as the interest is only for the surface. Since the solubility of carbon almost doubles between 1700°F and 1800°F, lower temperatures would be more suitable for greater layer control on the resultant graphene. Liquid precursor technique would hence be ideal as it has been successfully used for graphene growth at 950°C (1742°F).

3.4.1. Fabrication procedure

304 grade stainless steel foil (0.25mm thick, from Alfa Aesar) has been cut into a small piece (2cmX5cm) and used as the substrate for the growth. Care has been taken to avoid any major wrinkles and obvious contaminants. The experimental setup is the same described in section 3.1 (Figure 3-4). Hexane was taken as the liquid source in the flask at input I5 and input I6 is not used. The substrate is inserted into the quartz tube and the ends closed. The recipe followed has been graphically depicted in Figure 3-12 and is as follows. After sufficiently pumping down the chamber and tubing, the substrate was heated to 950°C with a flow of Ar/H₂ (S1 to I2, V1, R1 open and V2, V3 closed). Once the temperature is stabilized, Ar/H₂ is closed (V1) and hexane vapors are flown (V3, V4 open) while maintaining the pressure in the chamber to be 500mTorr (controlled with R2). An exposure time of 5 minutes is used, irrespective of the number of layers needed in the final graphene structure. Unlike the case of pristine graphene and N-doped graphene grown on copper substrates described in sections 3.2 and 3.3, the growth of graphene on stainless steel is a solution-perspiration process. Hence, the cooling rate is crucial in defining the number of layers formed on the surface. Depending on the number of layers desired, the cooling rate is changed by either opening the split tube furnace partially or fully. Once the temperature falls to 800°C, hexane vapors are cut off (V3 close) and Ar/H₂ flow resumed (V1 open) until cooled.

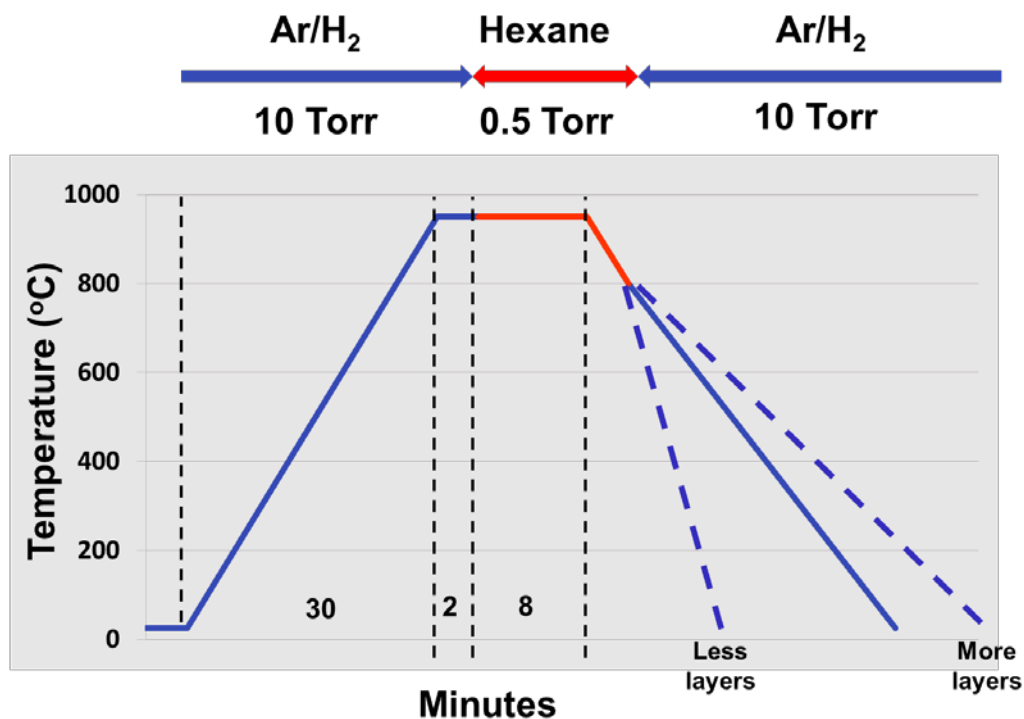


Figure 3-13: Recipe for graphene growth on 304 grade Stainless Steel substrates. The number of layers formed is dependent on the cooling rate

3.4.2. Characterization

Scanning electron images of the surface of stainless steel before graphene growth is shown in Figure 3-13 (a). It can be observed that the surface is relatively smooth and has ridges and groves as a result of rolling process employed industrially while making thin foils. The resulting structure after graphene growth is shown in Figure 3-13 (b to d). The presence of a thin continuous film of graphene with wrinkles at places is clearly visible. It can be seen that the grain boundaries in the stainless steel structure have been heightened after the high temperature processing. The structure of graphene however does not limit itself to the grain boundaries and is continuous across annealed consecutive

grains. Though atomic scale imperfections in the crystal structure of graphene are obvious and dependent on the grain structure of substrate, on a larger scale it is not prominent.

To confirm the crystal structure of the graphene, the structure has been observed using a Transmission electron microscope. As Stainless steel, is chemically inert, it is not easy to separate the graphene on the surface without seriously damaging it. So in order to get a sample with minimum physical damage, a small piece of stainless steel substrate with graphene grown on it is first soaked in dilute marbles reagent for few hours, transferred into water and sonicated for 30 minutes. The solution was then dropped on a TEM grid and dried. Graphene flakes which have come loose from the sample would be deposited on the grid and can be observed. Figure 3-14 (a) and (b) show the high resolution images of such a sample, clearly identified to have 3 graphitic layers stacked. The diffraction patterns shown in Figure 3-14 (c) Confirms the crystalline nature of the sample, as the discretely spaced points can be referenced to graphitic carbon.

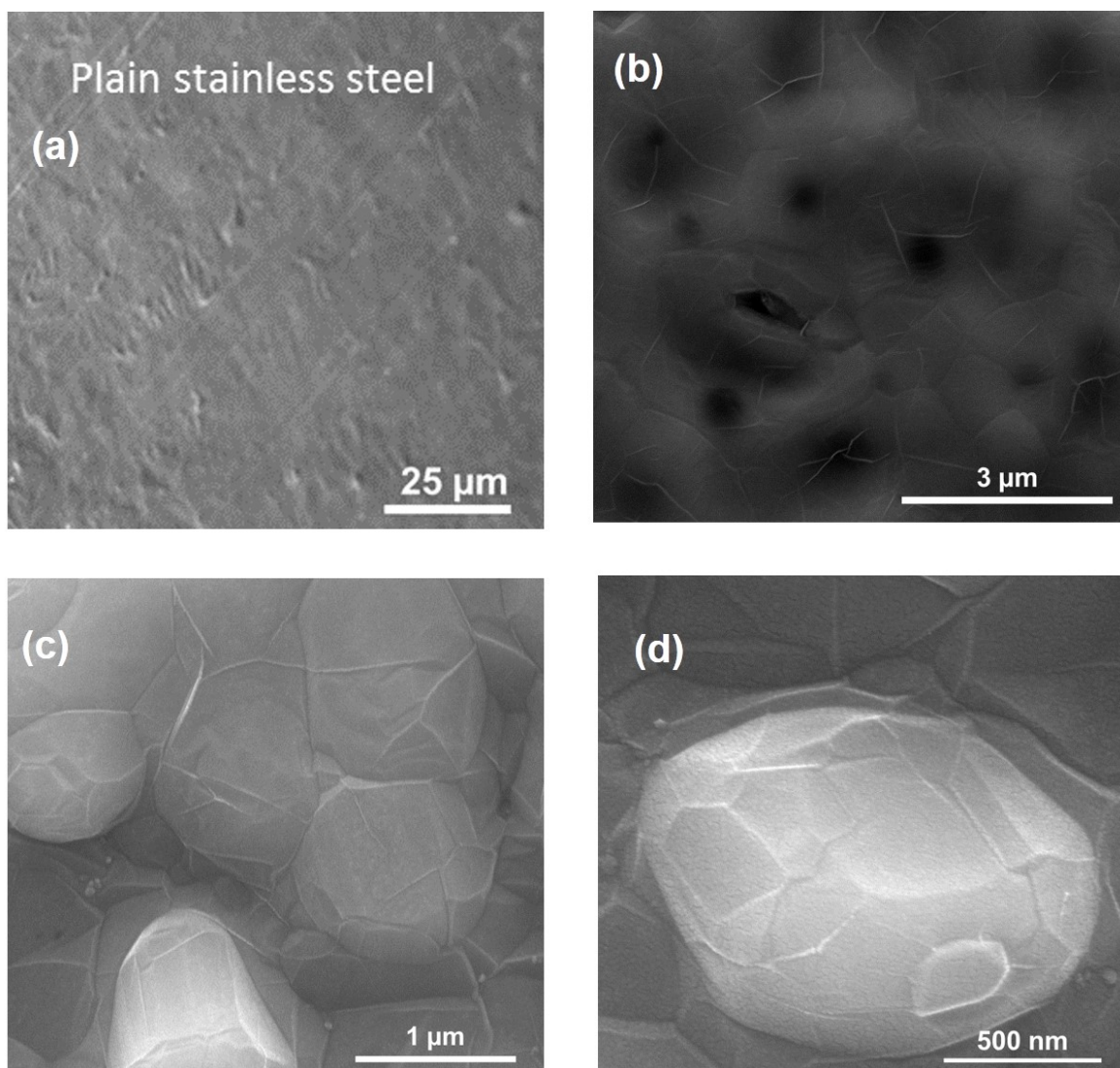


Figure 3-14: (a) Scanning electron micrograph of the surface of stainless steel foil. (b-d) various magnification images of the surface after graphene growth. A thin layer with wrinkles and grain boundaries can be clearly seen to blanket the metal.

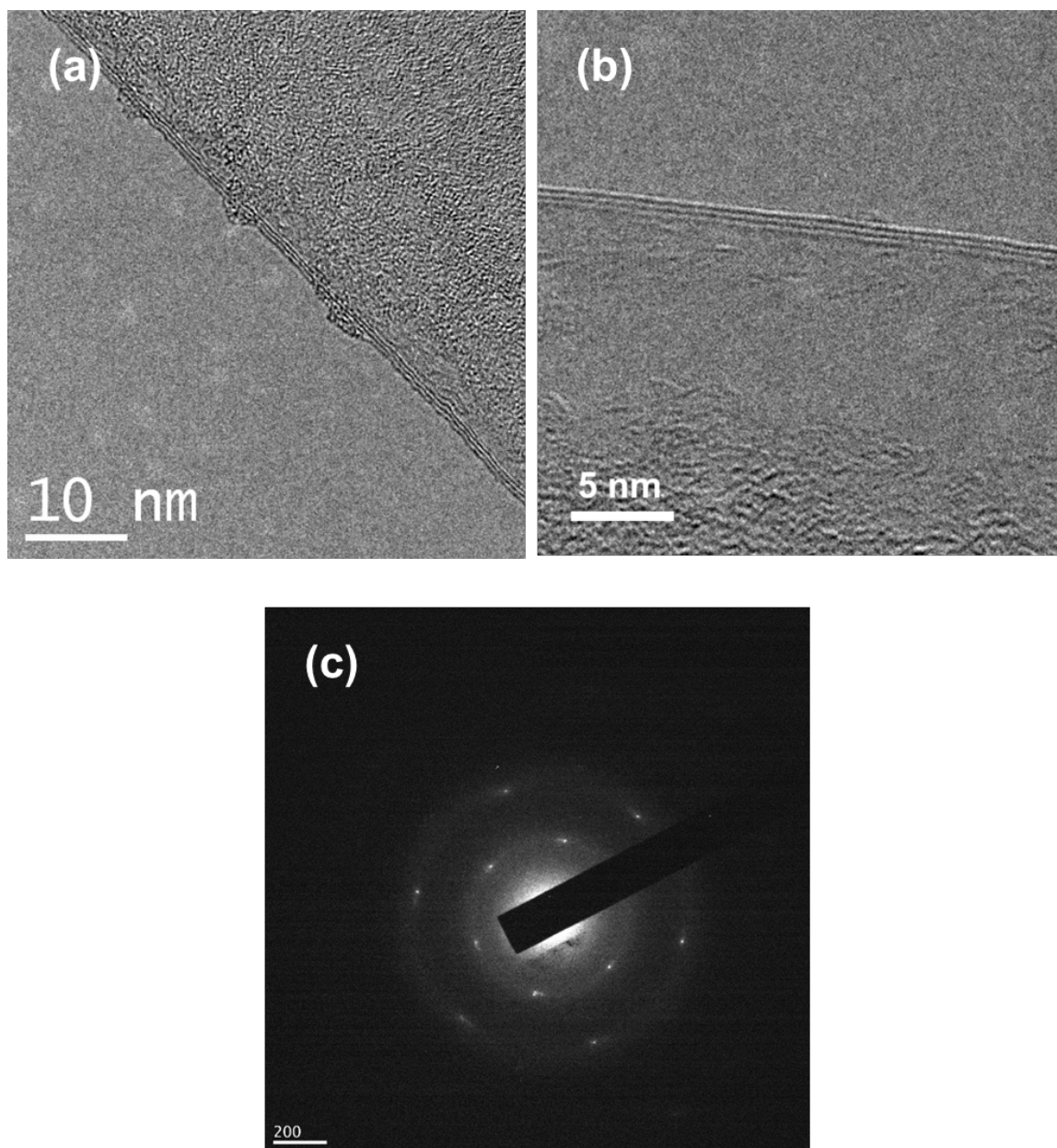


Figure 3-15: (a and b) Transmission electron micrograph images of the 3 layered graphene grown on stainless steel substrates. (c) Diffraction pattern of the sample confirming the crystalline structure of graphene

As mentioned above, the number of layers in the graphene grown on stainless steel cannot be controlled by the duration of carbon exposure. The cooling rate in turn dictates the number of layers present in the resultant structure. To quantify this mechanism, a controlled experiment has been conducted. A stainless steel sample is quenched after heat treating it with carbon source (obtained from a commercial manufacturer), it results in carburized steel for which the Raman spectra is shown in Figure 3-15(plot labelled Quenched). The spectrum has a disorder-induced 1D band centered at 1368 cm^{-1} and, a very low intense symmetry-allowed graphite band (G-band) at $\sim 1585\text{ cm}^{-1}$. This is due to the formation of highly disordered graphitic carbon as a result of dissolved carbon atoms in the steel lattice not having enough time to escape to the surface. However if the heat treated steel is cooled slowly, sufficient carbon atoms are diffused to the surface thereby forming graphitic layers. Raman spectra of such samples cooled at a rate of $15^\circ\text{C}/\text{sec}$, $2^\circ\text{C}/\text{sec}$ and $0.7^\circ\text{C}/\text{sec}$ from 950°C to 800°C are shown in the respective plots of Figure 3-15. These samples are characterized to have one, two and few(>3) layers of graphene respectively as deduced from the intensity ratios of G peak at $\sim 1585\text{ cm}^{-1}$ and the 2D peak at $\sim 2700\text{ cm}^{-1}$.¹⁷⁸ The absence of defect induced 1D peak at 1368 cm^{-1} in these samples indicates that defects in the graphene are significantly less.

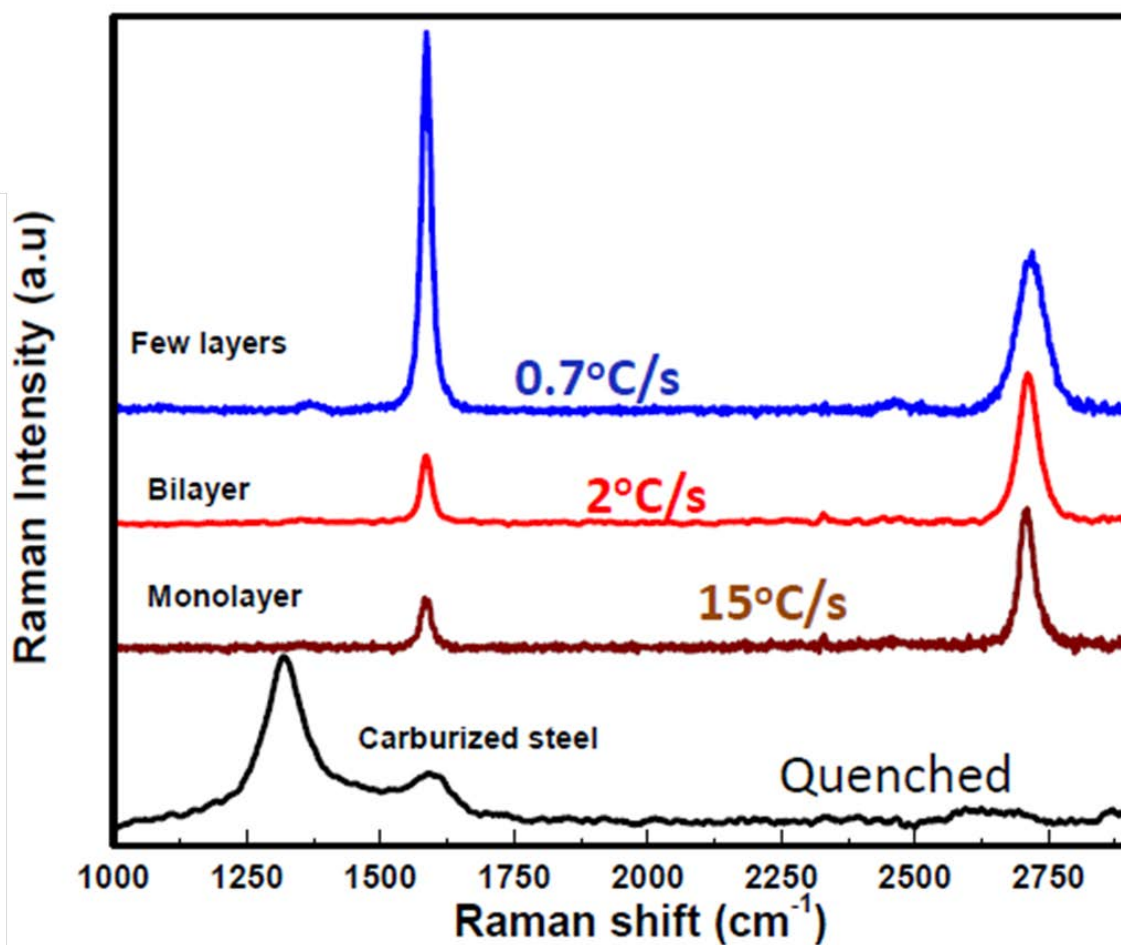


Figure 3-16: Raman spectra of graphene grown on stainless steel substrates. The cooling rate dictates the number of layers that form on the surface. While a quenching the sample results in the carbon being locked in the lattice, controlled cooling would allow carbon precipitation and graphitize on the surface

To test the effect of the carbon exposure time during the growth process, a control experiment was conducted. One sample with 3 minutes exposure while the other with a very long 40 minutes exposure have been fabricate with a similar cooling rate. The sample with 3 minute exposure resulted in defective 1-2 layer graphene while the long 40 minute exposure yielded a high quality 1-2 layer graphene (plots of the corresponding

samples shown in Figure 3-16). The most important observation here is that the Raman spectra of the 40 minute exposed sample is similar to that of the 5 minute exposure with similar cooling rate (Figure 3-15), ruling out any influence of exposure time greater than 8 minutes. This is mainly because the solubility of carbon in austenitic steel is very minimal at 950°C,¹⁷⁰ and the graphene growth is concluded to happen only when the sample is cooling down.

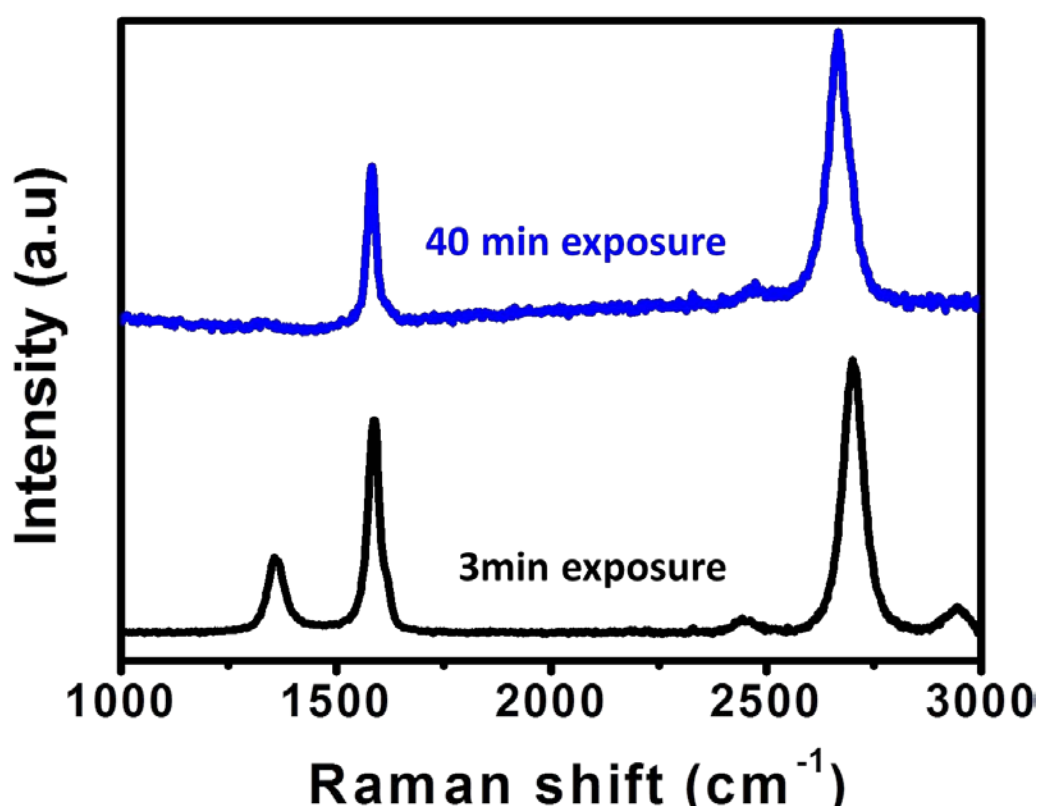


Figure 3-17: Raman spectra of two samples with similar cooling rates, one with very long, 40 minute exposure to Hexane vapors during the growth process at 950°C and the other with 3 minutes exposure. The duration of carbon exposure does not define the number of layers formed in case of stainless steel substrates

3.5. Direct synthesis of Graphene covered 3D metallic substrates

Though graphene has attained due attention by current research community, owing to its exceptional two-dimensional properties, many applications call for structures with a 3D architecture. Having a third dimension has several advantages, the major one being increased surface area. It is not practical to deposit a two dimensional material such as graphene on to high aspect ratio three dimensional structures efficiently. One alternative is to create three dimensional structure out of metals such as copper, nickel or stainless steel through established chemical routes and later grow graphene on to them using CVD technique. Such a two-step approach has several problems to it. One, the fine 3D structures cannot survive the high processing temperature required for graphene growth. Two, having a uniform exposure of carbon precursor into high aspect ratio 3D structures is not efficient and would result in shadow effects. Finally, if chemical etchants are used, they would leave behind other contaminants which can affect the quality of graphene. In this work, a one step process has been developed wherein, etching of metallic substrates to form 3D structures has been done together with graphene growth on it. This process yields a clean uniform coating of graphene directly on micron sized mesh like metallic structures.

3.5.1. Fabrication procedure

For fabricating the porous 3D structures, a metallic thin foil (either copper or stainless steel, depending on the requirement) is inserted into the quartz tube of the chemical vapor deposition (CVD) furnace described in section 3.1. Perfluorohexane (aka- C_6F_{14} or tetradecafluorohexane, hereby called PFH) (99% purity and sealed under argon,

from Sigma Aldrich) is taken in the flask at Input I5. PFH is highly sensitive to air, as it has high solubility of oxygen, which can hinder the graphene growth. Hence it is stored in a glove box and small quantities transferred in a sealed flask as needed. Input I6 is not used and is left closed. The growth recipe is graphically depicted in Figure 3-17 and is as follows. The furnace was pumped down to the base pressure and then heated to a temperature of 950°C while flowing Ar/H₂ gas to maintain the pressure at 10 Torr (S1 set to I2, V1 open and V3 closed). Once the desired temperature is reached, hydrogen was stopped and the furnace was flushed with pure argon for a minute and then turned off (S1 is tuned to I1). Vapors of PFH are then passed for 10 to 12 minutes (V1-close, V3, V4 open). The pressure in the tube is maintained at 600 mTorr (regulate R2). Longer or shorter exposure time would result in variations of the size and shape of the resultant surface features. The furnace was then cooled down and as the temperature reaches 800°C, PFH flow is stopped while purging the tube with pure argon flow (V3 close and V1 open).

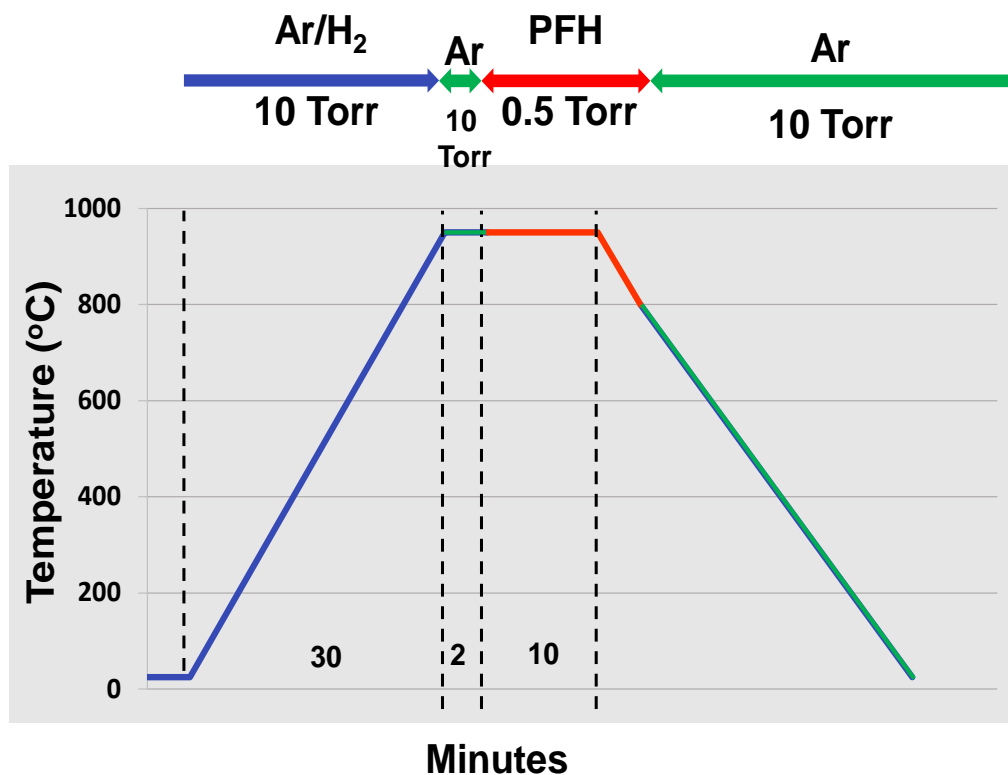


Figure 3-18: Recipe for synthesis of graphene covered 3D etched metallic structures.
Care is taken not to mix PFH vapors with hydrogen at high temperatures

3.5.2. Characterization

PFH has a composition of C₆F₁₄, and has high concentration of fluorine in the structure. Fluorine being highly reactive element has been extensively used in etching technologies. Reactive Ion Etching used widely in the semiconductor industry uses ionized fluorine atoms using high power plasma to etch patterned features on various kinds of substrates, including silicon, oxides and metals.¹⁸⁶ In a similar way, here, the vapors of PFH when passed through the high temperature zone of the CVD tube, undergoes pyrolysis and breaks down into individual fluorine and carbon atoms. Absence of oxygen or hydrogen in the tube avoids any instantaneous reactions. The fluorine ions

then being highly reactive would attack and etch out the surface of the substrate. At the same time, carbon atoms having a favorability to form graphene does so on the surface. The process is schematically depicted in Figure 3-18. The etching process is dominant at crystal imperfections in the substrate and is non uniform and as a results forms three dimensional structures. Both copper and stainless steel have been used in this process to form porous structures.

Scanning electron images of porous copper structure formed by 8 minute exposure of PFH are shown in Figure 3-19. A honeycomb like structure is formed due to the fluorine etching. The ordered pores formed can be attributed as a result of the rolling process used in the industrial production of copper foils. As thicker metal blocks are rolled into thin foils, a directional stress is created resulting in soft and hard regions in the metal. When exposed to fluorine, the softer regions etch faster resulting in the honeycomb like structure. In the image with higher magnification, graphene layer can be seen blanketed on the copper substrate.

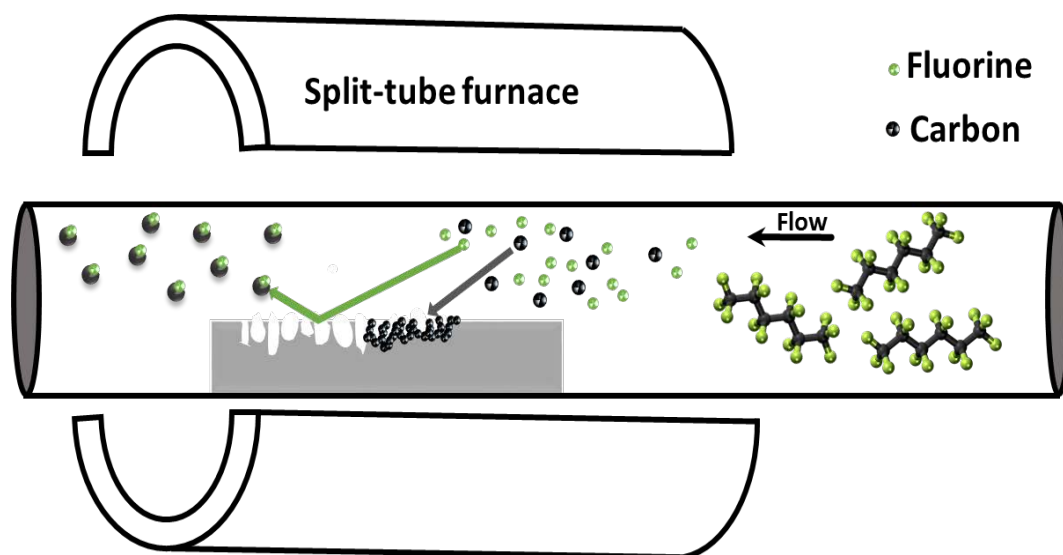


Figure 3-19: schematic representation of the mechanism of formation of 3D patterns on metallic substrate. Fluorine ions in pyrolyzed PFH are responsible for etching while carbon atoms form graphene on the surface

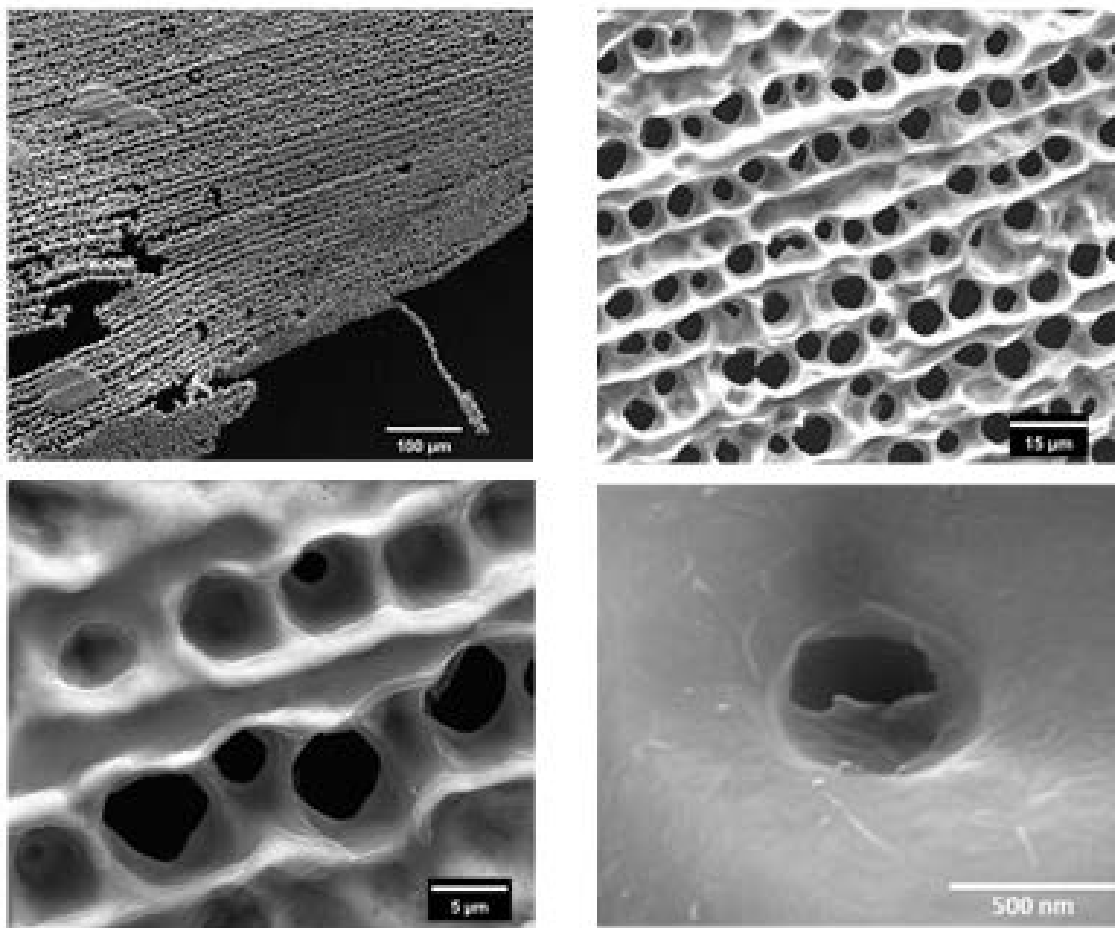


Figure 3-20: Porous copper with graphene coating formed by CVD using PFH as the precursor

The Raman spectrum of the structure is shown in Figure 3-20 and has the signature of pristine graphene with 2 to 3 layers with large disorder peak at ~ 1200 . The disorder in the crystal structure can be presumed to be a result of the 3D nature of the structure. Figure 3-21 shows the survey analysis of the surface of the structure using XPS. No traces of fluorine were observed in the structure, while 4% oxygen was detected on the surface. Copper, which is the substrate for the sample had a negligible trace on the surface, the reason being the blanketing of 2 to 3 layered graphene.

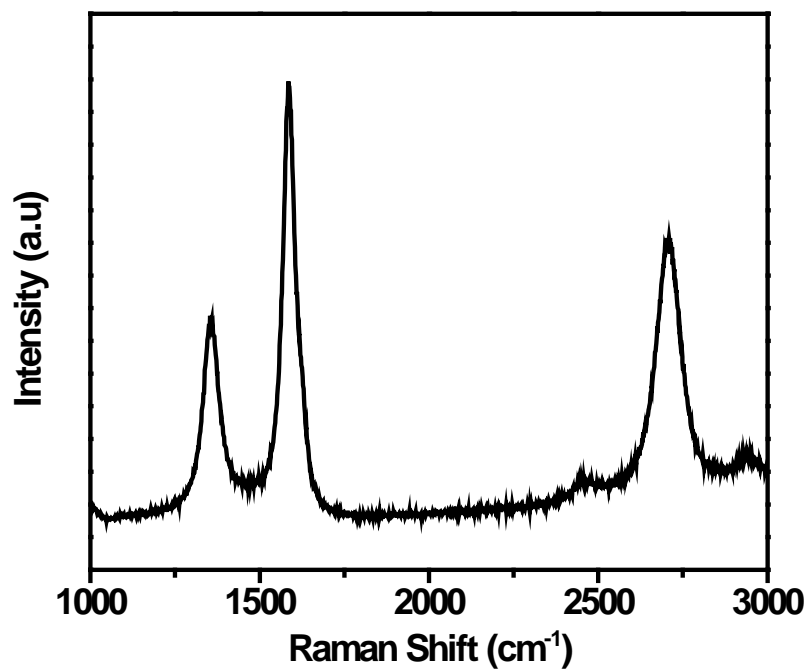


Figure 3-21: Raman spectra of graphene covered 3D copper substrate

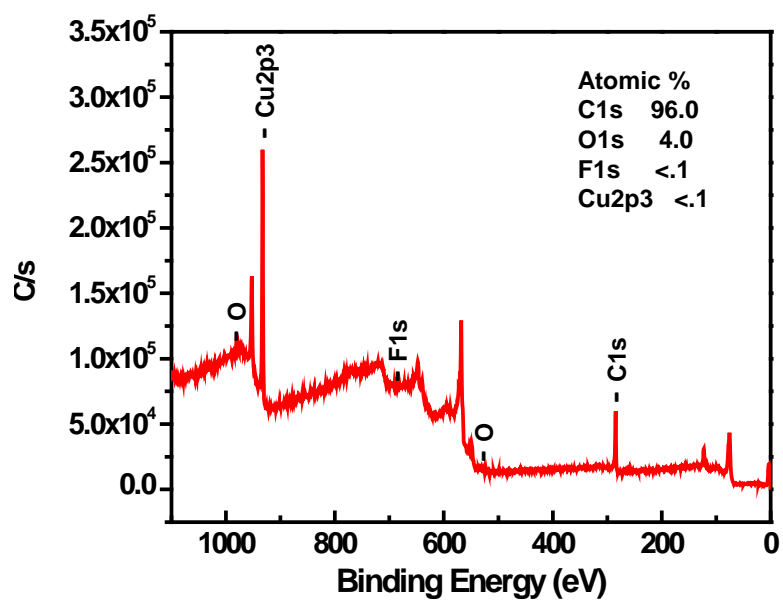
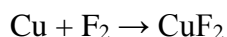
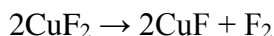


Figure 3-22: X-ray photoemission spectroscopy analysis of the surface of 3D copper substrate

In the process of synthesizing the porous copper structures, a second by-product is also obtained. The chemical interaction of fluorine with copper is defined as follows: Copper and fluorine react at temperatures of 400 °C to form Copper (II) fluoride. It occurs as a direct reaction.



Copper fluoride in turn loses the fluorine at temperatures close to 950 °C in a two-step process.



As the vapors of PFH flows from the source side to the vacuum side in the CVD furnace, it pyrolysis and reacts with the copper foil and the thus formed copper fluoride is carried through the tube, where it further heats up. When it gets in contact with the walls of the quartz tube, the fluoride undergoes reduction reaction on experiencing high temperature, forming copper nanoparticles. These copper particles agglomerate on the walls of tube eventually turning into a thin foam like structure. The Scanning electron images of this foam, peeled off from the walls of the furnace is shown in Figure 3-22. The structure consists of discrete blobs of interconnected copper nanoparticles. High resolution images reveal graphene layer covering these particles.

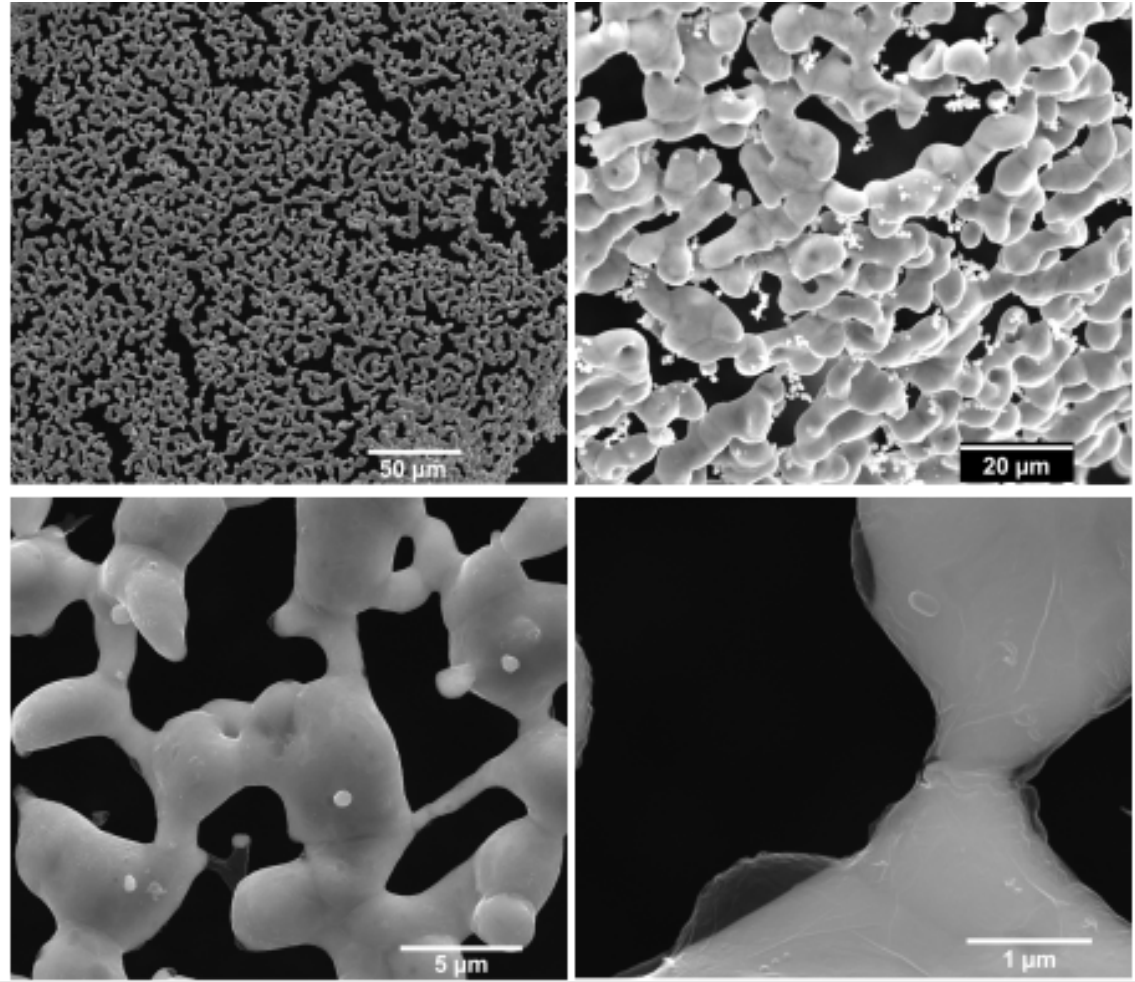


Figure 3-23: Scanning electron micrograph images of interlinked copper particles, formed as a byproduct while synthesizing 3D copper structures

Using this technique, porous stainless steel structures were also developed. The surface of the structure obtained thru a growth with 12 minutes exposure of PFH is shown in the SEM Micrographs of Figure 3-23. Compared to that of copper, the rate of etching of stainless steel is much slower, and doesn't etch through the thickness of the foil. The high magnification image in (a) shows that the etching is more prominent at the grain boundaries forming ridges. While the grains are also etched with random porosity. On closer observation of high magnification images in panel (b) and (c), it can be

deduced that the pores are in fact in a mesh like pattern instead of vertical holes. The pores in the structure have a range of sizes with a typical diameter ranging from 500nm to 2 μm . Figure 3-23(d) shows a close-up of a single pore and the blanketed graphene on the surface can be clearly distinguished. The image in Figure 3-23(f) is an SEM micrograph of the porous stainless steel cut and showing the cracked edge. It can be seen that the steel is converted into a porous structure only until $\sim 10\mu\text{m}$ in depth from the surface. The bulk of the foil is unaffected.

In Figure 3-24, the Raman profile of the surface of the porous stainless steel is compared to that of graphene grown on planar stainless steel (fabrication in Section 3.4). The similar intensity and positions of the G and 2D peaks indicate that both the structures have 2 to 3 layered graphene on them. A low intensity D peak is observed at $\sim 1275\text{cm}^{-1}$ in case of the 3D structure, this defect induced peak can be attributed to the disorder introduced in the graphene lattice due to the curvatures of the pores.

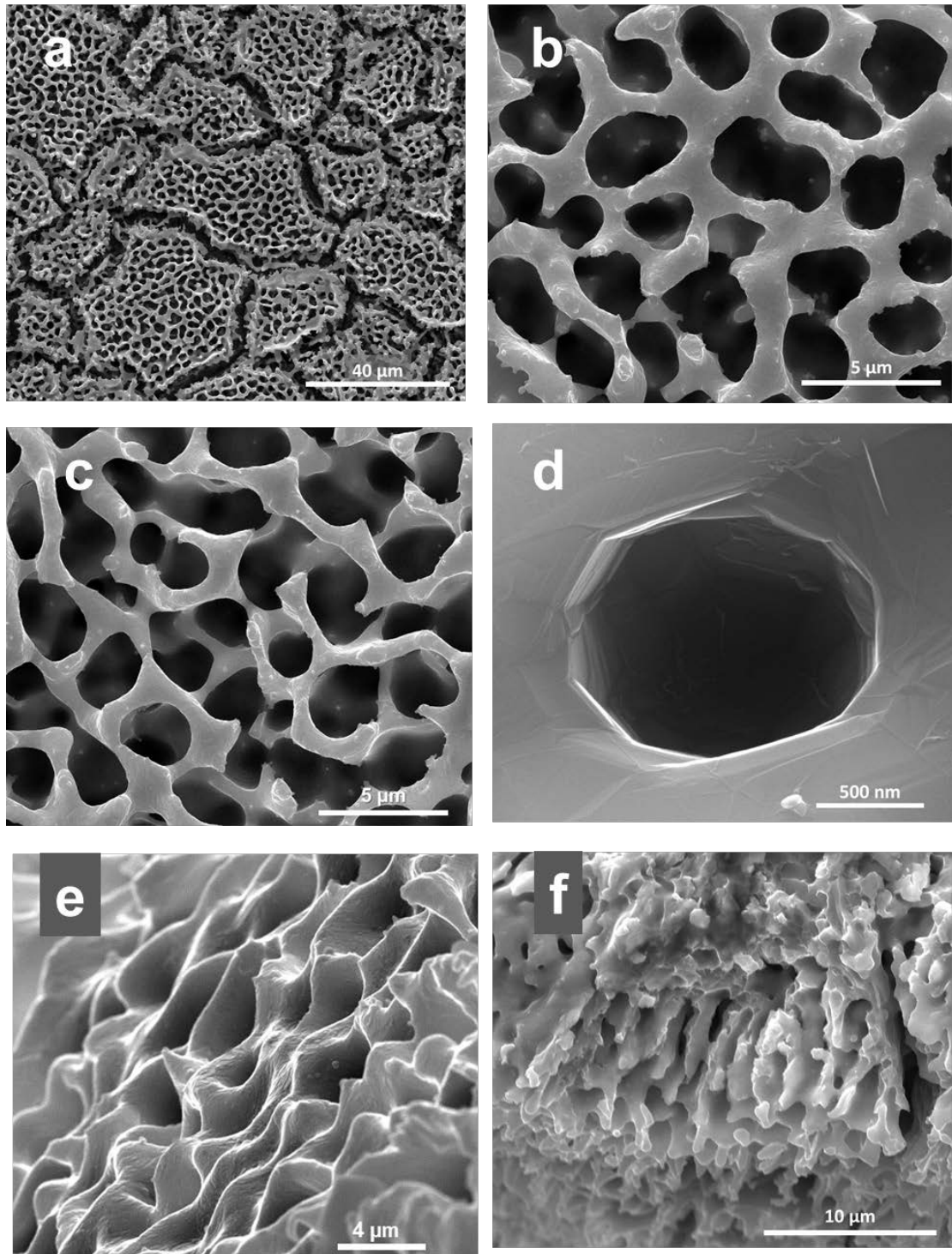


Figure 3-24: Scanning electron micrographs of 3D porous stainless steel foils. (a-c) Surface profile (d) magnification of single pore with graphene visible on the surface (e) sample viewed at an angle (f) cross section of a cracked sample, the porous nature is observed until a depth of $\sim 10\ \mu\text{m}$

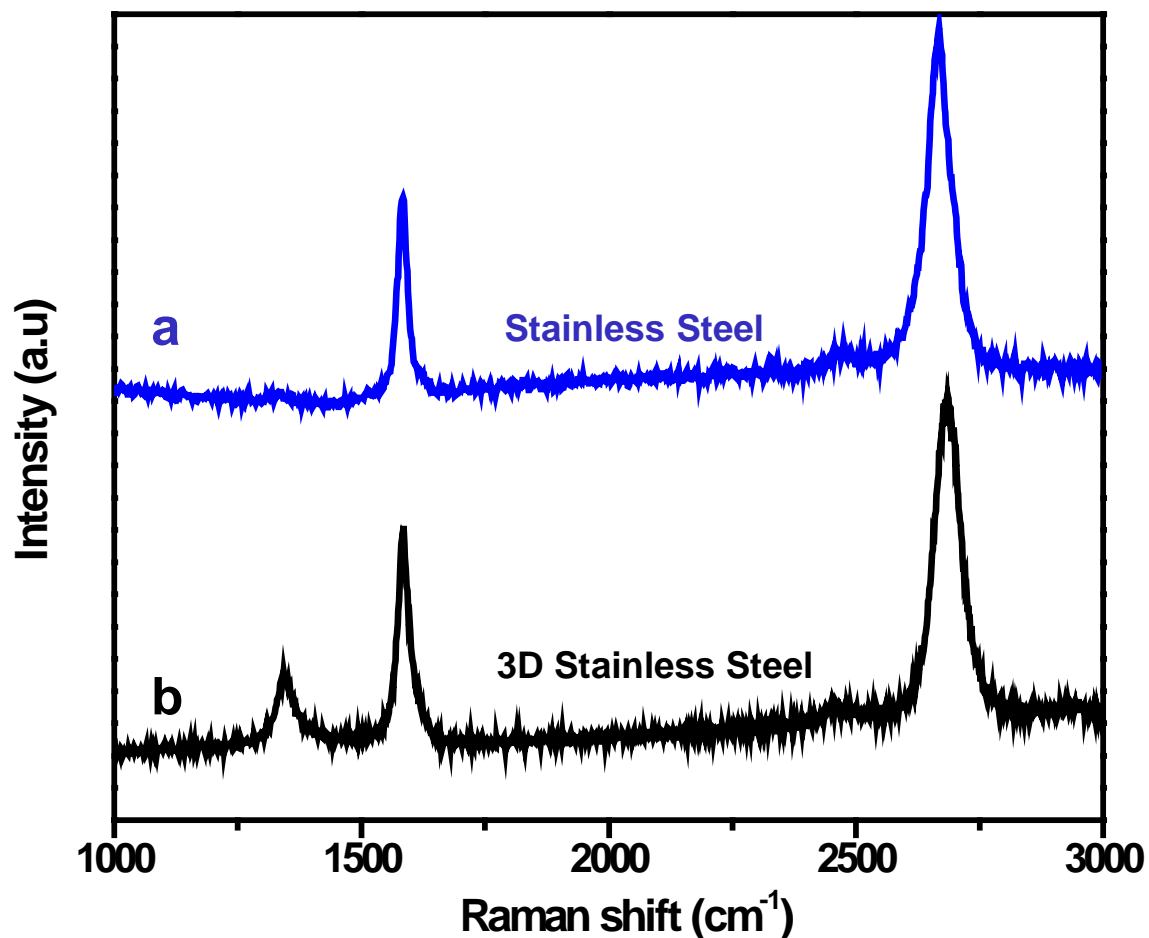


Figure 3-25: Raman spectra of graphene on 3D stainless steel compared to that of graphene on planar stainless steel

3.6. Conclusions

Chemical Vapor Deposition technique which has been extensively used in synthesizing nanomaterials has been employed to fabricate various graphene based materials. A customized experimental setup has been built wherein certain degree of flexibility in choosing different kinds of carbon sources has been incorporated. Liquid precursor techniques have been developed to fabricate variations of one to few layer

graphene over a large, continuous area. Building up on the reported technique of using hexane vapors as the carbon precursor in a low-pressure CVD technique to fabricate high quality graphene on copper foils, modifications in the process have been explored by changing the liquid precursors and the metallic substrates. Acetonitrile has been used as the precursor to fabricate Nitrogen-doped graphene onto copper foils. A 5% atomic doping has been realized using this technique, with a majority of nitrogen atoms in the pyridine form followed by pyrrolic and graphitic dopants. Apart from copper substrates which follows the physical adsorption mechanism to form graphene on the surface, diffusion and perspiration mechanism of graphene growth on Stainless Steel substrates has been explored. Highly defect free graphene has been realized with precise layer control achieved by controlling the cooling rate during the synthesis. Finally, apart from depositing two-dimensional graphene on to planar substrates, a novel concept has been developed wherein the metallic substrate has been converted into a 3D porous structure while concurrently covering the surface with continuous graphene layers. The process greatly increases the accessible surface area at the nanoscale.

Chapter 4

Graphene as a material of use in ultrathin energy storage devices

Though carbon is commonly used in both Li-ion batteries and supercapacitors technologies, enhancing its capacity through nanostructuring and chemical modification is of current research focus.^{98,103,187} Several carbon nanostructures such as CNT, nanofibers, graphene and their hybrid structures have been used as active electrode materials.^{98,108,187,188} Also, other high capacity materials such as metal oxides, polymers etc. have been used with a carbon support backbone to stabilize their performance.^{116,189} Some of the major performance issues of using carbon as an electrode material are (1) its high interfacial resistance with the current collector (effecting the power density) (2) Low specific energy density (per gram) (3) Low Areal energy due to current battery/supercapacitor design constrains.¹⁹⁰

Interfacial resistance issue

The majority of battery electrodes are fabricated by painting electrode slurries onto metallic foils. This always results in substantial contact resistance, which is amplified over cycling as the electrode peels off from the current collector. In case of graphene, initial research exploration used reduced graphene oxide powders which had similar contact issues.⁵ This added resistance in the system effects the power densities and cuts back its high rate capability. To overcome this issue, minimizing the electrical mismatch between the active material and the underlying substrate is critical.¹⁹¹ Direct growth of electrode material onto current collectors can intrinsically solve this problem.

Specific energy density issue

Compared to other active electrode materials, carbon has theoretically low energy density. This is governed, in case of lithium ion batteries, by the chemistry of the reaction with lithium ions. The nominal interaction of graphitic carbon with lithium forms a LiC_6 compound, thereby accommodating one lithium ion by 6 carbon atoms. It has been theoretically speculated that by introducing defects in the graphitic structure, this chemical dynamics can be tuned, and forming LiC_2 compound is feasible.¹⁰³ Selectively introducing these defects can be achieved by engineered doping. Atomic level doping of carbon structures with nitrogen, sulfur etc. have been attempted and reported to enhance the lithiation performance.¹⁹² Such an approach towards graphene would need to be taken up with caution, as the ultrathin structure would lose other favorable properties, such as conductivity, if the level of doping increases an optimum threshold.

Areal energy enhancement issue

Conventional two dimensional (2-D) thin film battery electrodes have been fabricated on planar current collectors. One of the major drawbacks with 2-D thin film Li-ion batteries is the low energy per unit area delivered due to low electrode mass loading per unit area. Low mass loading issues are common in any low density materials such as carbon, however this issue will be severe in case of nano-carbons due to their ultra-low tap density. In recent years, there has been a realization that improved battery performance can be achieved by reconfiguring the electrode materials currently employed in 2-D batteries into 3-D architectures.¹⁹³ The general strategy of this approach is to design cell structures that maximize power and energy density yet maintain short ion transport distances. While many possible architectures can achieve this goal, a defining characteristic of 3-D batteries is that transport between electrodes remains one-dimensional (or nearly so) at the microscopic level, while the electrodes are configured in complex geometries (i.e., nonplanar) in order to increase the energy density of the cell within the footprint area. A 3-D matrix of electrodes (in a periodic array or an aperiodic ensemble) is necessary to meet both the requirements of short transport lengths and large energy capacity. Improvements in energy per unit area and high-rate discharge capabilities are two of the benefits that may be realized by these 3-D cells. Hence, redesigning current collectors would result in high surface area and hence high areal energy density.

We hypothesize that direct fabrication of graphene electrode materials on current collector substrates would minimize the interfacial resistance and enhance overall power capabilities of energy device. Further, atomic level doping of foreign atoms such as

nitrogen in the carbon structure would enhance the capacity (energy density) of the electrode materials itself by providing additional sites for lithium ion storage and finally by using 3D architectures enhancement in areal energy can be achieved.

Further, as already discussed, research in the lithium ion battery anode area is two forked, one to enhance the capacity of carbon based electrodes and the other is to stabilize the performance of high capacity materials. Theoretically, materials such as silicon have an order of magnitude higher gravimetric capacity towards lithium.¹⁹⁴ However, in practice these materials have several stability issues arising from their high capacity. Volume expansion as a result of lithium intercalation damages the structural integrity of the electrode over cycling, losing physical contact with the underlying current collector, driving it towards failure. Also, lack of conductivity further hinders the performance when the electrode material loses direct contact with the current collector. As a possible solution for stabilizing these high capacity materials, a 3D host structure which can support the mechanical integrity can be employed. A conducting matrix which can hold the material after several cycles of charge/discharge and have the room for volume expansion would be an ideal solution.

In order to test these hypotheses, Li-ion battery and supercapacitor applications of one to few layers of graphene and nitrogen doped graphene that are directly grown on current collector substrates (synthesis is already discussed in Chapter 3) have been discussed in this chapter. Further, the concept of building autonomous energy devices has been demonstrated by integrating a graphene based energy storage devices with that of a ZnO based energy harvesting device. Parts of this chapter have also been reported in the two publications, Reddy et al. (2010)¹⁷⁵, and Gullapalli et al. (2011)¹⁷⁶

4.1. Lithium ion battery applications

4.1.1. Cell fabrication

To test the performance of the graphene materials, CR2032 coin-type cells were fabricated in an argon filled glove box. In a typical cell fabrication, graphene based electrodes were used as working electrodes, lithium metal as the counter/reference electrode and 1 M solution of LiPF_6 in 1:1 (v/v) mixture of ethylene carbonate (EC) and dimethyl carbonate (DMC) (obtained from Solvionic Inc.) is used as the electrolyte with fiber glass membranes (Whatman) as the separator. Galvanostatic charge–discharge cycles were conducted using ARBIN BT 2010 Battery Analyzer at room temperature. Cyclic voltammetry analysis were done using an Autolab potentiostat.

4.1.2. Electrochemical properties of graphene grown on planar current collectors

As mentioned above, the conductivity between graphene and current collector plays an important role in increasing its rate capability. Direct growth of graphene onto current collectors is expected to address this issue. To test this, graphene grown directly onto stainless steel substrates (universal current collector for both anode and cathode) described in Section 3.4 have been analyzed for their usability in lithium ion batteries. Stainless steel foils were cut into required size before depositing graphene onto the surface. Two to three layered graphene is deposited on the substrates by controlling the growth parameters and test cells were assembled.

Galvanostatic charge/discharge measurements conducted at constant current of $10\ \mu\text{A}/\text{cm}^2$ between 3.2 V and 0.02 V are shown in Figure 4-1 (A). The first cycle showed a discharge capacity of approximately $0.2\ \text{mAh}/\text{cm}^2$ with a large plateau at about 0.7 V. Considerable loss in capacity was observed in the second cycle ($\sim 0.15\ \text{mAh}/\text{cm}^2$) due to the SEI (solid electrolyte interface) formation, very commonly observed in carbon based electrodes. The plateau at 0.7 V in the first discharge curve can be attributed to the formation of an SEI film, on the surface of graphene, associated with electrolyte decomposition and formation of lithium organic compounds.^{108,195} In the subsequent cycles, the discharge plateau disappeared and a reversible capacity of $0.05\ \text{mAh}/\text{cm}^2$ was observed after 50 cycles of charge/discharge (Figure 4-1 (B)). After the first cycle, the Columbic efficiency remained very stable throughout the cycles, indicating that the formed surface film remained intact. Good electrical contact between the electrode and the current collector was realized by the direct growth of graphene on Stainless Steel foil.

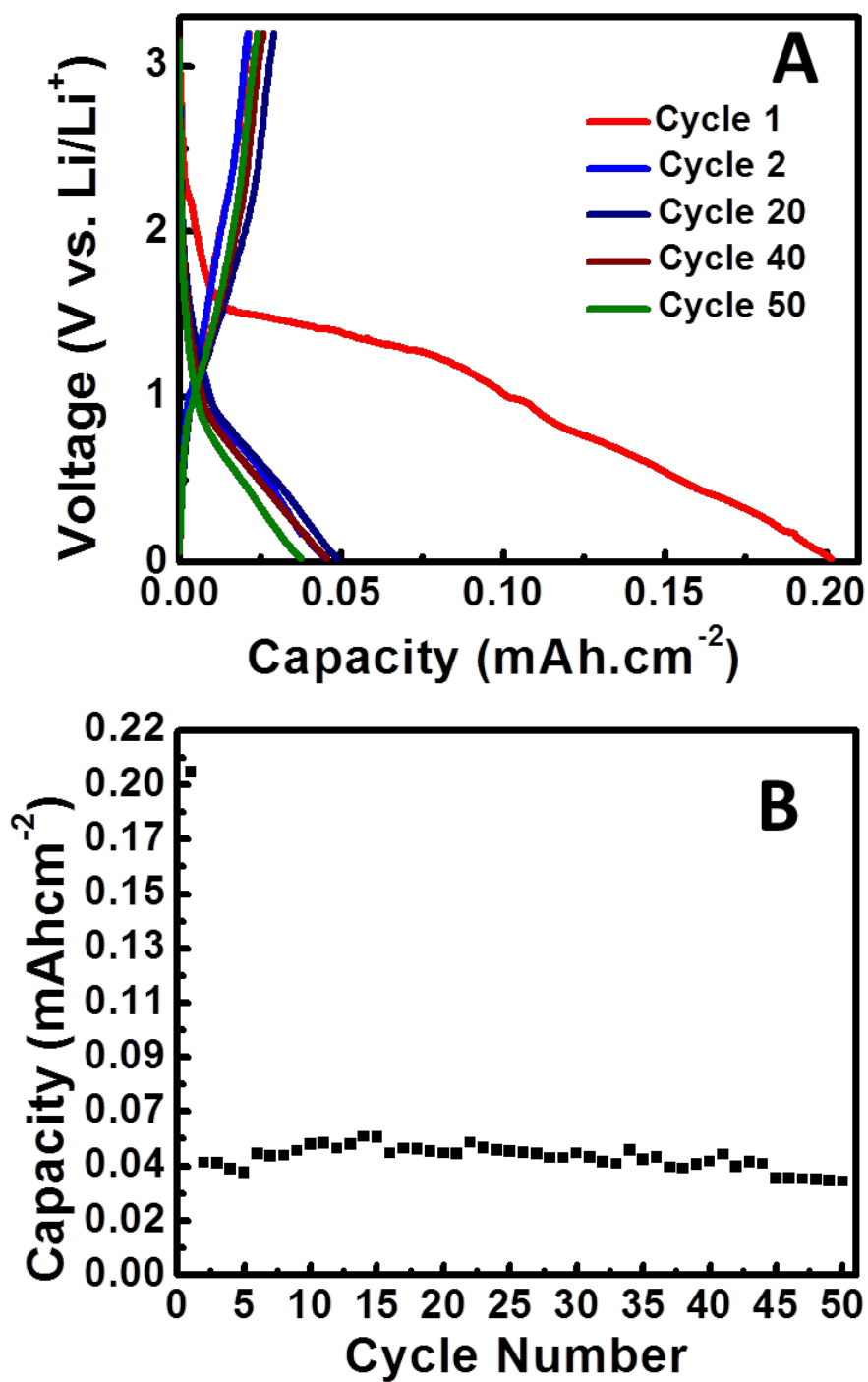


Figure 4-1: (A) Charge discharge profiles of graphene directly grown on stainless steel substrates (B) Discharge capacity of the cell observed over a number of cycles

To confirm the stability of the graphene at higher rates, variable rate analysis was conducted. Figure 4-2 plots the discharge capacity of a cell cycled initially at a slower scan rate with a current rate of 2Acm^{-1} . After the capacity is stabilized after 5 cycles of charge discharge, the current rate was increased in steps for every 5 consecutive cycles. The battery though lost capacity due to a faster discharge rate, displayed stability over cycles. Finally the full nominal capacity of the battery is restored when the current rate is returned to the nominal rate. This confirms that the structure of the electrode is not damaged due to high rate of operation resulting in better stability.

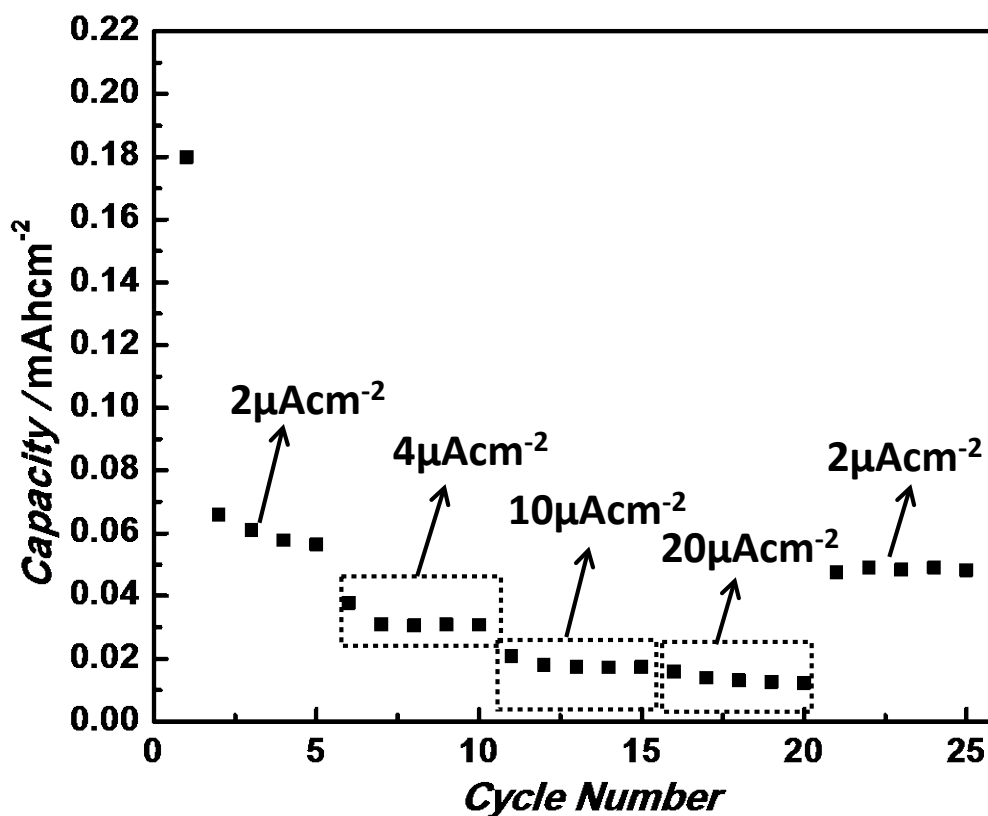


Figure 4-2: Rate capability studies of graphene on stainless steel

4.1.3. Effect of nitrogen doping on the electrochemical properties of graphene

In order to compare the advantages of having nitrogen doping in graphene, its performance is compared to that of pristine graphene films, both synthesised on copper substrates (synthesis described in sections 3.3 and 3.2 respectively). Test cells with both the electrodes were prepared and cycled at a rate $5\mu\text{A}/\text{cm}^2$ between 3.2 V and 0.02 V vs Li/Li⁺. Figure 4-3(A) shows the specific capacity vs cycle number plots for the graphene and the N-doped graphene. Pristine and N-doped graphene shows reversible discharge capacities of $0.03\text{ mAh}/\text{cm}^2$ and $0.05\text{ mAh}/\text{cm}^2$ respectively. This correlates to an increase of 25% in the reversible capacity as a result of 5 at% nitrogen doping. This increase can be attributed to a combination of different topological defects induced in the N-doped graphene electrode. Firstly, a large number of surface defects are induced onto the graphene films by N-doping which leads to the formation of a disordered carbon structure which further enhances Li intercalation properties.¹⁸⁷ As observed in the XPS data, the N-doped graphene also has a high percentage of pyridinic N atoms present in it. The pyridinic N-atoms could also be involved in the improvement of reversible capacity of the N-doped graphene electrode compared to the pristine graphene electrode.¹⁹² Electrical contact between the electrode and current collector plays an important role in the power capability of the Li-ion battery. Good electrical contact between the electrode and current collector was realized by the direct growth of graphene on copper foil.

Figure 4-3(B) shows the detailed high rate cycling results for the N-doped graphene electrode. Galvanostatic charge/discharge experiments were conducted at various currents to investigate the rate capability of the electrode material. Stable nominal capacity was attained at a current rate of $1\mu\text{A}/\text{cm}^2$ corresponding to a C-rate of C/60.

Subsequent cycles were cycled at higher current rates as shown in Figure 4-3(B). Even at very high current rates of operation, such as $100 \mu\text{A}/\text{cm}^2$, excellent capacity retention of 60% of the nominal capacity was observed. On returning to the low current rate of $1 \mu\text{A}/\text{cm}^2$ the nominal capacity ($\sim 0.06\text{mAh}/\text{cm}^2$) is retained, which is comparable with previously reported values of carbon based thin film electrodes.¹⁹⁶ The results of high rate electrochemical studies prove that the N-doped graphene electrode could have both high rate capability and enhanced capacity due to structural doping.

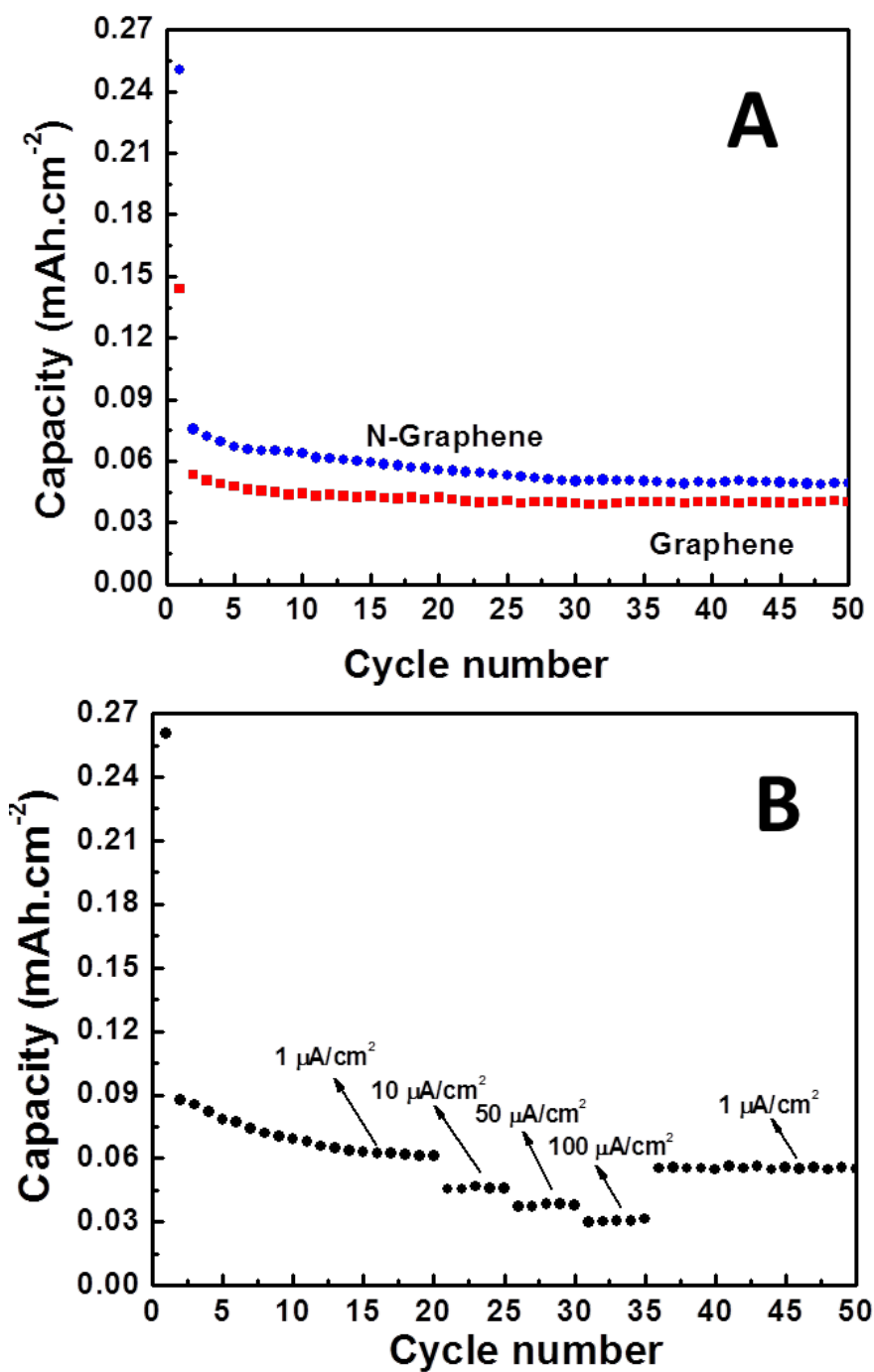


Figure 4-3: (A) Comparison of discharge capacities of nitrogen doped graphene and pristine graphene, directly grown on copper foils. (B) High rate capability test for Nitrogen doped graphene

4.1.4. Graphene on 3D metallic substrates as anodes for Li-ion battery

In order to compute the enhancement in the areal capacity as a result of having a 3D nature for the electrode, the porous stainless steel structures with graphene on the surface, synthesised as per the procedure in section 3.5 were tested. A lithium half-cell was constructed and its cyclic stability over continuous charge discharge has been studied. The rate capability plots of the battery is shown in Figure 4-4 (A). Compared to the 2D counterpart of graphene on planar stainless steel (Discussed in Section 4.1.2), the 3D structure had enhanced capacity at a higher operating current rate. Comparing the capacity at similar current rate of $16\text{A}/\text{cm}^2$, the planar structure had a capacity of $\sim 0.02\text{mAh}/\text{cm}^2$ while the 3D structure had a stable capacity of $\sim 0.07\text{mAh}/\text{cm}^2$. This enhancement can directly be credited to the increased accessible surface area of the electrode. Higher rate capability was also tested in a similar way and excellent structural stability of the electrode towards higher rates was confirmed. (Figure 4-4(B)). The 3D configuration has in fact confirmed the hypothesis of high-energy, high-power combination as a result of better electrode accessibility by the electrolyte.

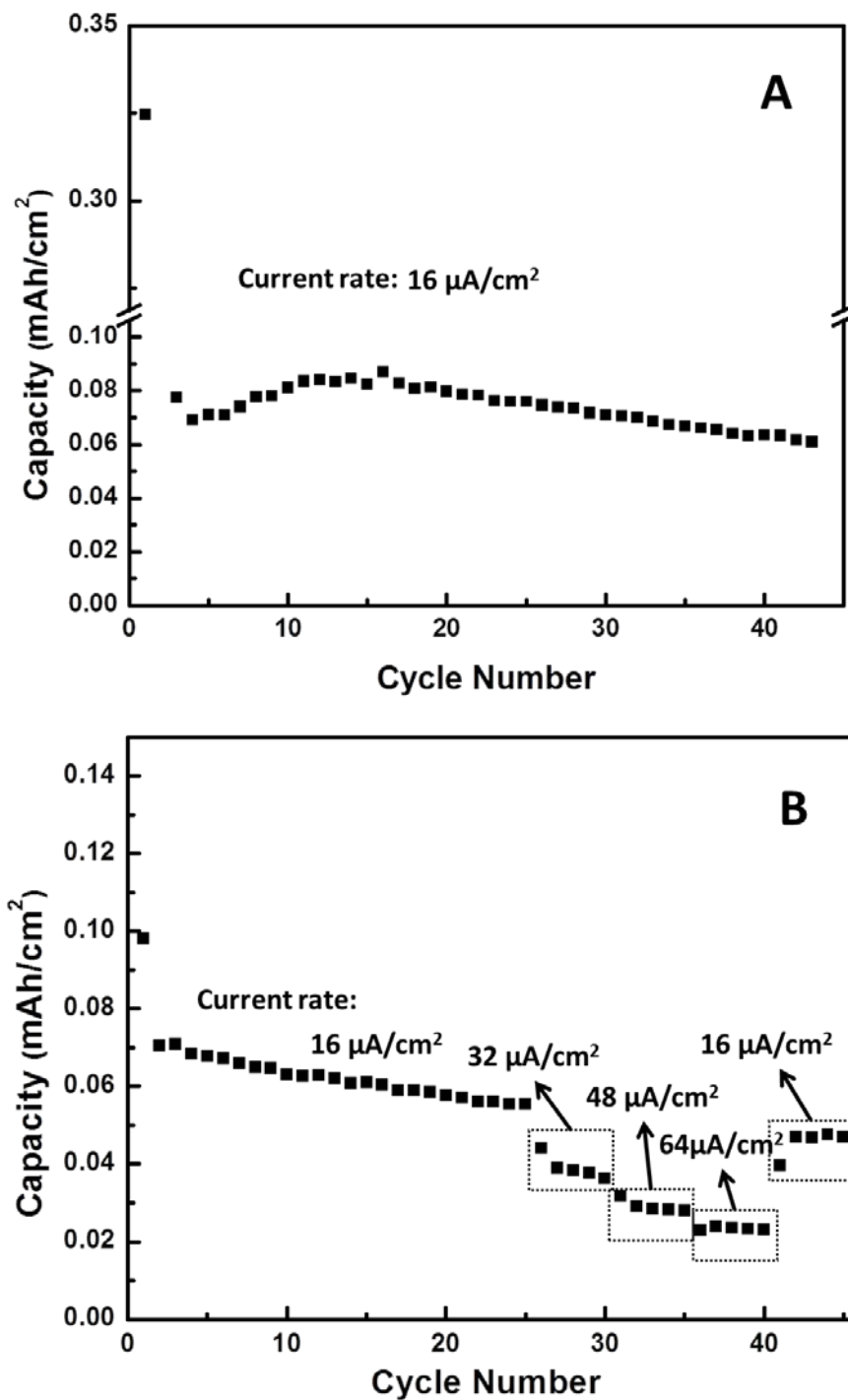


Figure 4-4: (A) Rate-capability studies of graphene covered porous SS substrates. (B) Discharge capacity versus cycle number for various current rates. Good capacity retention is observed for high current rates and the nominal capacity is regained upon returning to lower current rates.

4.1.5. 3D metallic substrates as current collectors for Li-ion

To stabilize the performance of high capacity materials, 3D electrode configurations have been proposed. Porous stainless steel structures have precisely this property, if the pores are filled with the active material, and hence can be hypothesised to be efficient current collectors. Moreover, the presence of graphene on the structure increases the conductivity of the electrode material. To test this hypothesis, in this thesis, one such high capacity electrode material (Silicon Nitride) has been deposited into the pores and its electrochemical properties compared to that of planar configuration.

It is envisioned that the use of 3D porous graphene covered stainless steel current collectors could stabilize adverse effects caused due to high volume expansion of SiN_x electrode materials. For this purpose, Silicon Nitride has been deposited into the pores of the structure using Plasma enhanced vapor deposition (PECVD) technique. Battery performance of the structure is gauged in comparison to a planar structure where similar thickness electrode material is deposited on to the surface of a plain stainless steel foil.

Deposition and Characterization of SiN_x

Plasma enhanced CVD (using commercial instrument -Trion Orion II PECVD) technique was employed to deposit 500 nm thin films of Silicon Nitride by the ionization of Silane (SiH_4). The deposition parameters include a chamber pressure of 600 mTorr and temperature of 400°C. A 15% Silane gas mixture in balance nitrogen is used as the silicon-nitrogen source, and flown at a rate of 70 SCCM. A deposition time of 20 minutes with the RF power set to 75% was used.

The surface morphology of the films have been studied using Scanning electron Microscope and the micrographs shown in Figure 4-5. While a continuous thin film like structure is formed on the planar 2D stainless steel (Figure 4-5(A, B), an area is scraped to have a contrast of the material), the deposition on the 3D structures is more of a particulate form (Figure 4-5(C-F)). This is presumed to be a result of the surface stresses due to the 3D architecture and is commonly observed in similar depositions.¹⁹⁷ The pores of the etched stainless steel substrates are loosely filled with the SiN_x while leaving voids in between. This can be advantageous for accommodating the high volume expansion of the electrode while cycling.

To characterize the chemical breakdown of the deposited material, X-Ray photoemission spectroscopy studies were conducted on them. Figure 4-6 (A) is the survey analysis of the surface, with the major peaks that have been identified labelled with their corresponding atomic compound. Figure 4-6 (B) is the elemental analysis of Silicon, with the peaks resolved into its constituent components. It has been mapped that the structure has three distinct phases, a high concentration of nitride, and two low intensity of oxide forms of silicon.

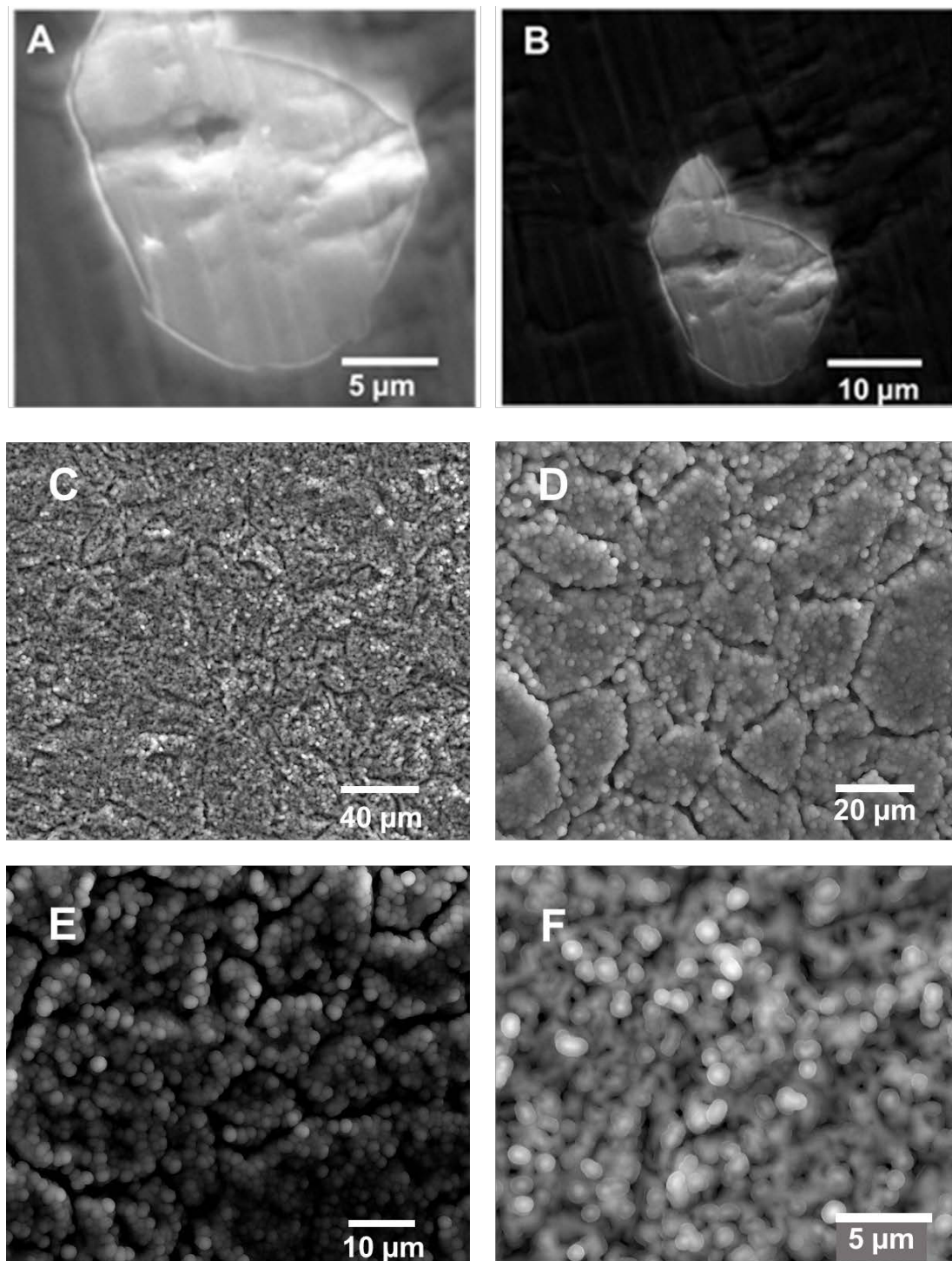


Figure 4-5: Scanning electron micrographs of SiN_x deposited (A,B) onto Planar stainless steel{an area scraped to identify the layer} (C-F) onto 3D stainless steel substrates

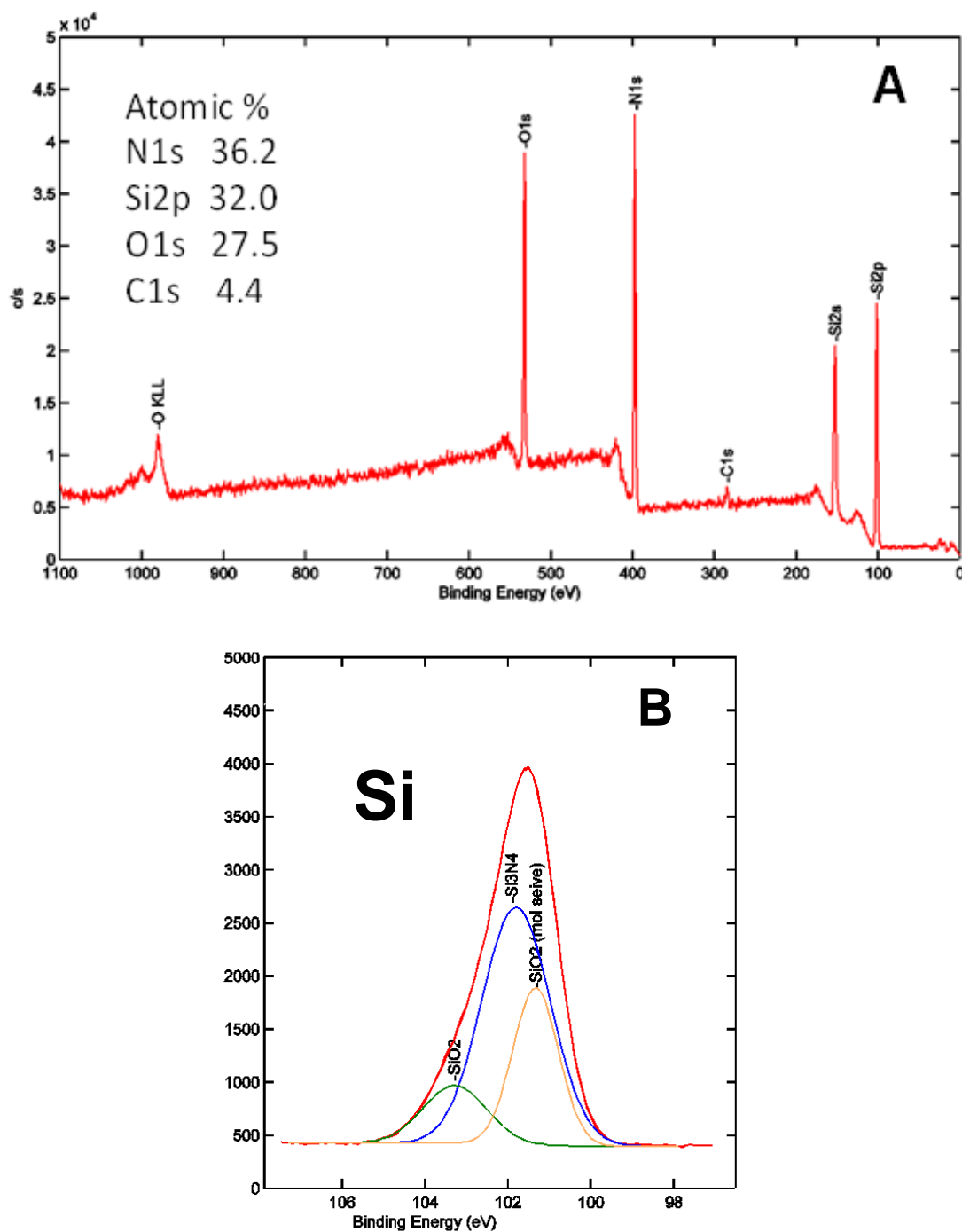


Figure 4-6: X-Ray Photoemission spectroscopy analysis of the SiN_x deposited onto the 3D stainless steel substrate. (A) Survey analysis with the major peaks labeled, atomic concentrations in the inset (B) Elemental analysis of Silicon, with the peak deconvoluted

Electrochemical performance of SiN_x

Figure 4-7(A) has the galvanostatic charge discharge profiles of 3D SiN_x electrode cycled between 0.05V and 1.5V. As it can be seen from the profiles, a clear lithiation plateau on both charge and discharge cycles is an indication of reversible lithiation of SiN_x electrode. Figure 4-7(B) is cyclic stability test results of 3D SiN_x electrode observed for 45 cycles at constant applied current. Though both 2D and 3D electrodes show almost similar capacities in the first cycle, drastic drop in the specific capacity of 2D electrodes is observed over cycling. As clearly seen from figure, 3D SiN_x electrode has retained considerable capacity over cycling compared to that of 2D planar electrodes. Hence, 3D graphene covered metallic substrates could be an ideal current collector for high volume expansion and low conducting electrode materials.

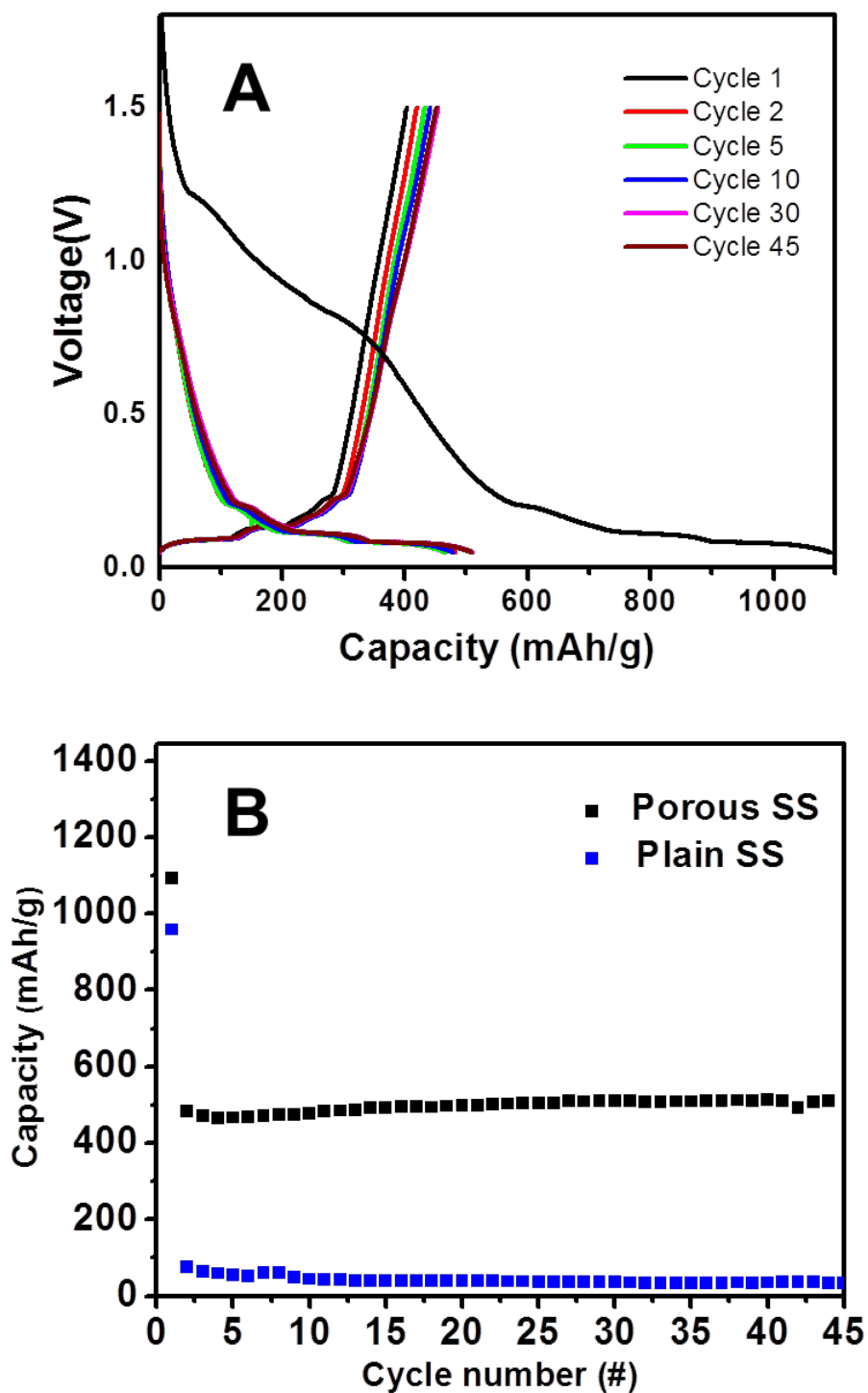


Figure 4-7: (A) Charge discharge profiles of the SiN_x electrode on 3D stainless steel.
(B) Comparison of discharge capacities of SiN_x deposited onto 3D stainless steel substrates and planar stainless steel

4.2. Supercapacitor behavior of graphene based structures

Carbon based materials have been the forerunners for the design of high performance supercapacitors, mainly due to their superior electrical conductivity and their ease of forming a double layer with the electrolyte interface. As surface area is one of the key property of the electrode material controlling the overall capacitance and thereby the energy density of supercapacitor, 3D engineered graphene electrodes are expected to deliver superior electrochemical properties compare to their planar counterparts. The performance of both 2D and 3D graphene electrodes has been analyzed by constructing symmetric supercapacitor cells using room temperature ionic liquids (RTIL) as electrolyte. Due to their wide electrochemical stability window and thermal stability, RTIL's have been chosen for this study. 1-Butyl-1,2,3-dimethylimidazolium bis(trifluoromethylsulfonyl)imide (BMMI-TFSI) which has been reported to have good performance towards graphene based supercapacitors has been used.¹⁹⁸

Cyclic voltammetry analysis was performed on both graphene on planar stainless steel and graphene on 3D patterned stainless steel. The measurements were done at both room temperature and 120°C. As the electrolyte is stable at high temperatures, and using thermally stable stainless steel as the current collector, the capacitor is expected to withstand high temperatures, which can be very advantageous for certain applications. The CV measurements were done at varying scan rates of 100mv/s to 1v/s and between the voltage windows of -2.5V to 2.5V. Figure 4-8 shows the resultant plots of the analysis.

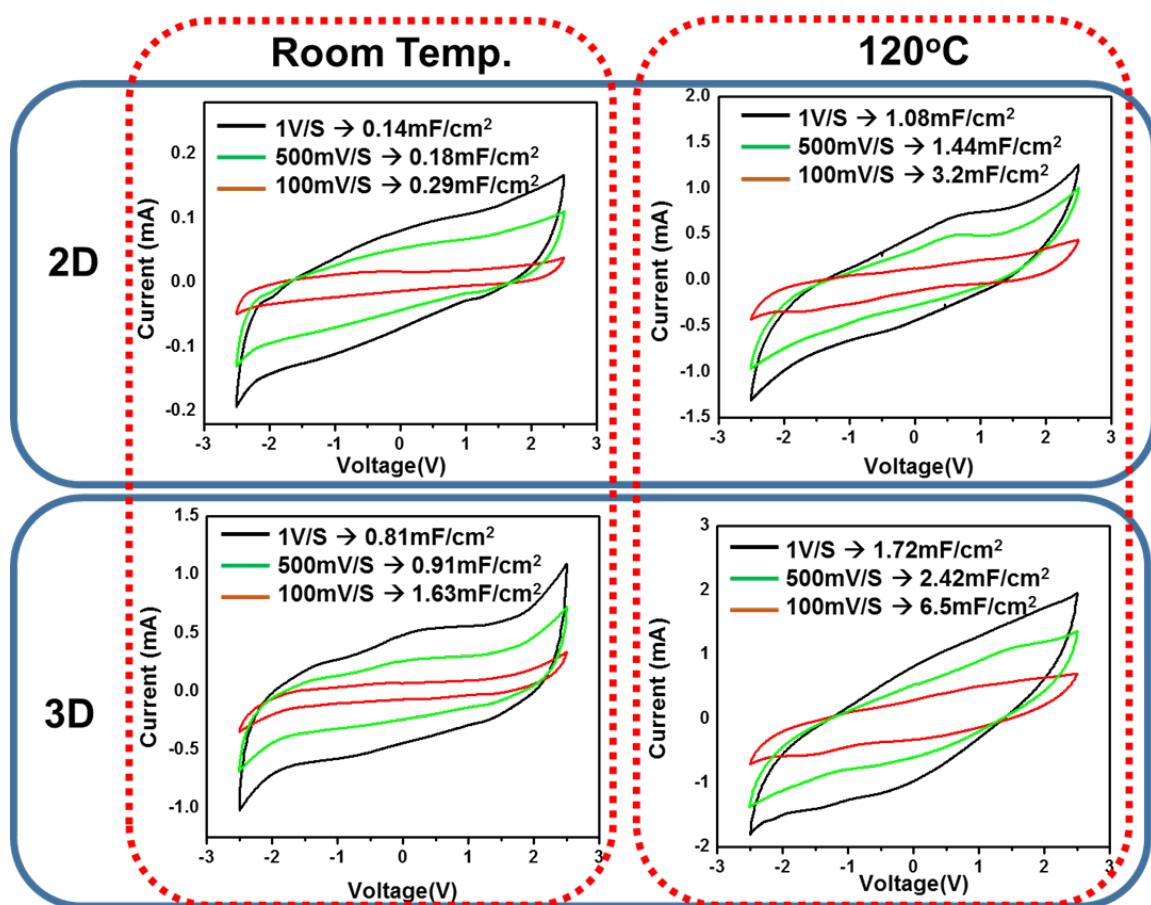


Figure 4-8: Cyclic voltammetry plots of supercapacitors fabricated out of graphene coated 2D and 3D stainless steel substrates. The capacitors were tested at different scan rates and at room temperature and 120 °C

It has been observed that in all conditions, a stable hysteresis curve is observed, without any sharp peaks. This confirms the double layer capacitance mechanism in the cell, and negates the existence of any electrochemical reactions. Also, as the electrode is in direct contact with the current collector, the capacitors had good charge retention even at very high voltage rates (even up to 1V/s). By computing the area of hysteresis, the net capacity of the system can be deduced¹⁹⁹ and the normalized values of the corresponding conditions have been included in the insets of the plots. It can be observed in every cell,

the nominal capacity decreases with an increase in scan rate, which is a commonly observed phenomenon, and is a result of the kinetics of ion diffusion. Moreover, capacities in case of high temperatures are observed to be higher in comparison to that of room temperature. This is a result of the reduction in the viscosity of the electrolyte, resulting in faster ion diffusion. Finally, in the case of 3D electrodes, a 5X enhancement has been observed at room temperature, when compared to that of planar Stainless steel electrodes, while still retaining the high rate capability. This can be attributed directly to the larger surface area of the 3D structure.

4.3. Energy storage-Harvester integration

In order to build autonomous energy device, energy storage devices discussed in previous sections (batteries and supercapacitors) has to be integrated with energy harvesting device (discussed in chapter Chapter 2). In order to build such an integrated hybrid device, energy outputs from individual components has to be matched. Specific capacities and rate capabilities of energy storage devices have to be matched with energy and power densities of energy harvesting device. Among the two energy storage devices studied (batteries and supercapacitors), supercapacitors are found to be better match with piezoelectric/pyroelectric based energy harvesters due to their high power densities. In order to realize the concept of building autonomous energy device, graphene based supercapacitors were integrated with ZnO based piezoelectric energy harvesters. The ability of energy harvested from ZnO-paper to charge a supercapacitors has been put to test. Having a flexible nature for both the harvester and graphene based supercapacitor facilitates easy formfitting into virtually any shape. Multiple layers of flexible harvesters

and capacitors can be used to increase the net energy of the device. Though a complete integrated device would require proper packaging and needs to include other support electronics such as current/voltage limiters for over charge/surge protection, an initial feasibility study is taken up in this thesis.

4.3.1. Design of experimental setup

To test the hypothesis of charging a capacitor with the ZnO-paper patch in a practical scenario, a vibrational beam setup has been designed. The setup involves mounting of a piezoelectric harvester device, made of 4 patches of ZnO-paper composite connected in series. The packaged device is attached to a $50 \times 0.7 \text{ mm}^2$ cross-section aluminium strip with a thin layer of epoxy, ensuring good adhesion for maximum strain transfer. A supercapacitor fabricated out of CVD grown graphene has also been attached to the beam, next to the piezoelectric device. To balance the energy mismatch between the harvester and the storage unit, a miniature capacitor is required. Hence instead of the conventional coin cell setup, an already reported in-plane configuration for the capacitor (Yoo et al.(2011))²⁰⁰ has been used. To fabricate this, 2 to 3 layered graphene is transferred on to a rigid insulating substrate and a gap is created by carefully scraping with a sharp razor blade. A solution of Thermoplastic polyurethane (TPU) with RTIL (BMMI-TFSI) has been dropped on the gap and acts as an electrolyte for the capacitor. Gold pads were sputter coated on either sides of the gap and act as current collectors to which wires are soldered to. A piezoelectric actuator (from Mide Technology Corporation, MA) is also attached to the aluminium beam and is used to excite the beam at different frequencies. The piezoelectric actuator was actuated using a dSPACE Data Acquisition and control unit in conjunction with a power amplifier. The capacitor is

connected in parallel to the harvester and the voltage is measured across the capacitor terminals using a potentiostat/galvanostat (Metrohm Autolab). The metal beam can also be heated with a heat gun and the temperature monitored using a probe thermocouple. The experimental setup is schematically described in Figure 4-9 (A) and a photograph of the same is shown in Figure 4-9 (B).

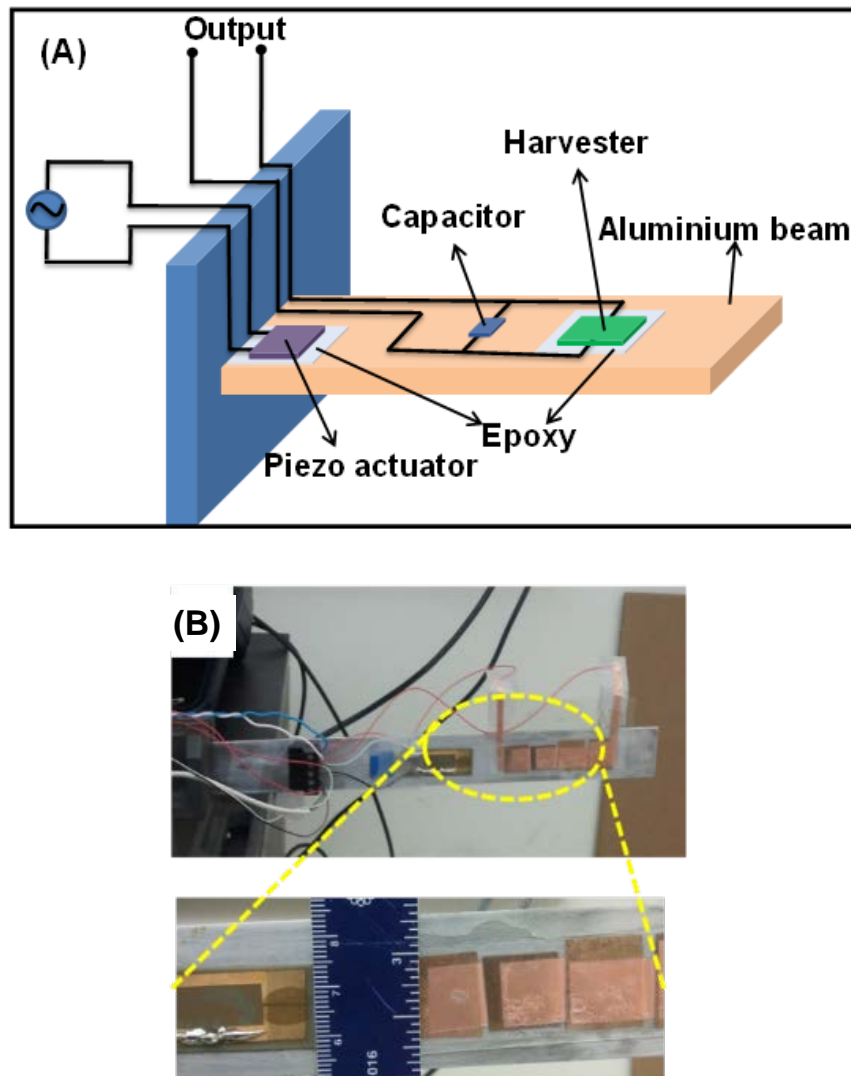


Figure 4-9: (A) Schematic of experimental setup for testing the integration of harvesting and storage units. (B) Photograph of the setup

4.3.2. Results and discussion

The metal beam is vibrated with a sinusoidal signal at a frequency of 10 Hz while monitoring the voltage on the capacitor. The observed voltage profile is plotted in Figure 4-10. The voltage is observed to increase from zero as the beam is continuously vibrated. After 30 minutes of continuous vibration, the voltage on the capacitor reached close to 1.8V (higher voltage is avoided keeping in consideration the stability of TPU-RTIL electrolyte). At this point, the vibration is turned off while continuously measuring the voltage. At the instance vibration is stopped, the raise in voltage is observed to stop and started to fall instead. The fade in the voltage is a characteristic of self-discharge mechanism of the capacitor, and is amplified by the losses due to the external wiring.

Similar tests were conducted on the setup at higher temperatures by heating the beam with a hot air gun and temperature monitored with a probe thermocouple. The temperature of the beam is maintained with up to a 5°C variation. The voltage profiles at temperatures of 80°C and 100°C are also included in the plot of Figure 4-10. The maximum voltage reached at higher temperatures is lower than that of room temperatures, and can be speculated to be due to losses in the capacitor, and interconnects.

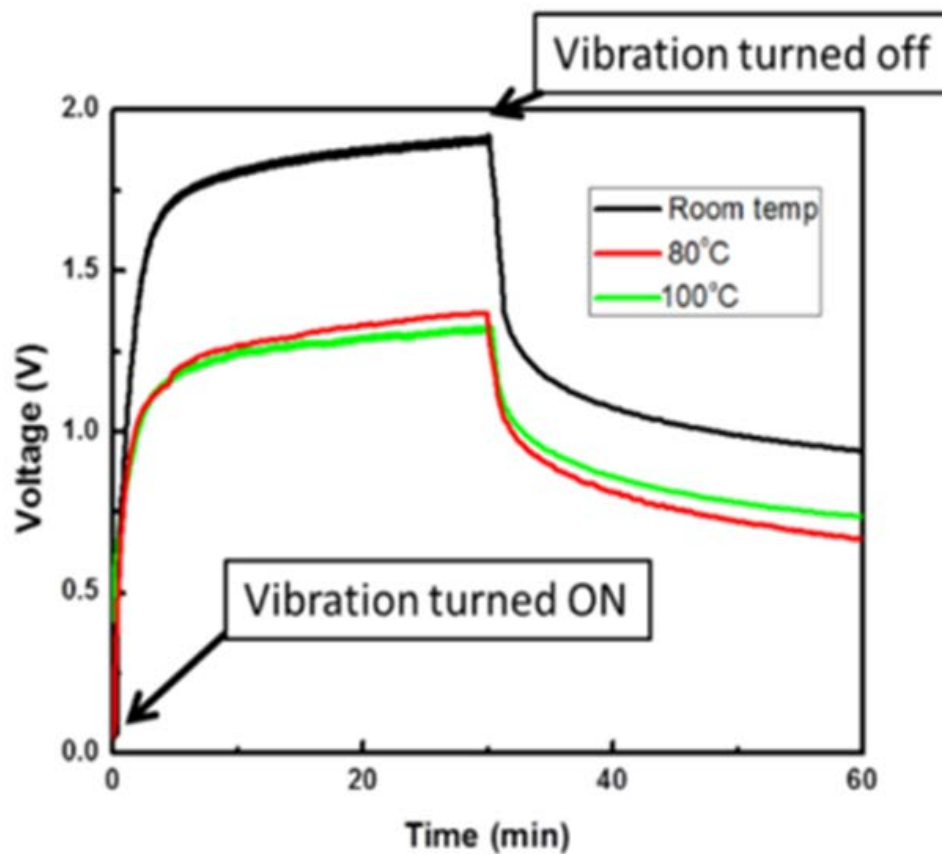


Figure 4-10: Voltage profile across the supercapacitor while charging it using the energy generated from the harvester, at various temperatures. The capacitor has a self-discharge mechanism once the vibration is turned off.

4.4. Conclusions

While graphitic carbon is known to be a material of use in lithium ion batteries and supercapacitors, the use of graphene grown directly on metallic substrates using CVD technique has been explored. By having graphene in direct contact with the metallic substrate used as the current collector, high rate capabilities have been achieved for both lithium ion battery and supercapacitors. Moreover use of stainless steel as the

substrate opens up doors for the devices to withstand harsh conditions and chemistries compared to traditional copper or nickel. Next, to enhance the capacity of such a system, two different approaches have been taken up. First, to increase the theoretical capacity of the material itself, the influence of dopants in the structure is explored. 5 at.% Nitrogen doping of 2 to 3 layered graphene is found to have a 25% enhancement in its capacity when used in a lithium ion battery. Second, to increase the areal energy density which is rather low owing to the 2D nature of the electrode material, a 3D configuration is explored. Graphene covered porous stainless steel structures have been used to test such a 3D architecture. Compared to 2D, this resulted in a higher rate capability and a fivefold increase in the capacity. Extending this, the usability of such 3D structures as current collectors for high capacity materials has also been proved. The architecture is shown to stabilize the capacity of silicon nitride electrodes over cycling. Finally, the concept of integration of energy harvesting and storage units is also demonstrated by charging a graphene based supercapacitor with the energy harvested from the vibrations of a metallic beam.

Chapter 5

Summary

In summary, with a broad goal of developing an autonomous energy device, capable of harvesting energy from the ambient and storing it for later use, material configurations have been explored. For the energy harvesting part, piezoelectric phenomenon has been employed with an intention to harvest multiple sources of energy. To address the challenges of using brittle ceramic piezoelectric, a simple, low cost, scalable process has been developed to synthesise a truly flexible form of piezoelectric composite material. By using the matrix of ‘paper’ as the structural backbone, ZnO nanostructures were fabricated completely encapsulating the cellulose fibers while still retaining its flexibility. The composite material has a convoluted piezoelectric property, like a bulk polycrystalline ceramic material. This robust material has been demonstrated to harvest multiple forms of energy; capable of producing an output voltage and power up to 80 mV and 50 nW cm⁻², respectively. Furthermore, it is shown that by integrating a certain number of devices (in series and parallel) the output voltage and the concomitant

output power can be significantly increased. Also, being sensitive to the strain applied to it, this ZnO-paper composite has also been used for strain sensing applications. The material is capable of measuring the strain experienced by a host structure when subjected to both static as well as dynamic loading.

For the energy storage part, the thesis has been focused on designing materials for ultrathin lithium ion batteries and supercapacitors. Carbon, being a very important material for electrochemical energy storage, its ultimate thinnest form, Graphene, has been explored. To realize an ultrathin carbon electrode, with good rate capability and stability, graphene has been directly grown on metallic current collectors.

Chemical Vapor Deposition technique which has been extensively used in synthesizing nanomaterials has been employed to fabricate pristine and doped form of graphitic layers onto copper and stainless steel structures. The mechanism of graphene growth on stainless steel has been introduced and studied in detail.

The efficiency improvement achieved by having graphene in direct contact with the current collector and also by having dopants in the lattice is systematically studied. Nitrogen doping into graphene has been done, using a modified liquid precursor CVD technique employing acetonitrile as the source. A 5% doping in graphene grown directly on copper resulted in a 25% increase in its capacity to hold lithium ions, with the capacity retained over cycling of charge discharge. Moreover use of stainless steel as the substrate opens up doors for the devices to withstand harsh conditions and chemistries compared to traditional current collectors like copper and aluminum.

Apart from depositing two-dimensional graphene on to planar substrates, a novel concept has been developed wherein the metallic substrate is converted into a 3D porous structure while concurrently covering the surface with continuous graphene layers. Fluorine atoms used as part of carbon precursor have been used to etch out the metal selectively. The process greatly increases the accessible surface area at the nanoscale. Compared to 2D planar configuration, this 3D structures resulted in a higher rate capability and a fivefold increase in the capacity when used as electrodes both in a lithium ion battery as well as in electrochemical double layer supercapacitor. Stainless steel being chemically stable at high temperatures, the capacitor has been demonstrated to have stable operability at high temperatures.

Extending this, the usability of such 3D structures as current collectors for high capacity materials has also been proved. The architecture is shown to stabilize the capacity of silicon nitride electrodes over cycling. The structure of SiN_x deposited on to planar stainless steel into a thin film loses its recyclable capacity after the first cycle due to large volume expansion of the material. When filled into the pores of the 3D structure, the encapsulating metal holds the silicon structure after cycling and a nominal capacity is retained over numerous cycles. Finally, the concept of integration of energy harvesting and storage units is also demonstrated. A vibrating beam setup is built to excite the ZnO-paper based harvester and store the energy generated into a graphene based supercapacitor device.

References

1. Systems, C. of S. P., Technology, B. on A. S. and, Sciences, D. on E. and P. & Council, N. R. *Meeting the Energy Needs of Future Warriors*. (National Academies Press, 2004).
2. Battery Supplies Ran Dangerously Low in Iraq. at
<http://www.nationaldefensemagazine.org/archive/2003/September/Pages/Batter_Supplies3776.aspx>
3. Kymissis, J., Kendall, C., Paradiso, J. & Gershenfeld, N. Parasitic power harvesting in shoes. in *Second International Symposium on Wearable Computers, 1998. Digest of Papers* 132–139 (1998). doi:10.1109/ISWC.1998.729539
4. Harvesting energy while walking | Article | The United States Army. at
<<http://www.army.mil/article/60272/>>
5. Karami, M. A. & Inman, D. J. Powering pacemakers from heartbeat vibrations using linear and nonlinear energy harvesters. *Appl. Phys. Lett.* **100**, 042901 (2012).
6. Platt, S. R., Farritor, S., Garvin, K. & Haider, H. The use of piezoelectric ceramics for electric power generation within orthopedic implants. *IEEEASME Trans. Mechatron.* **10**, 455–461 (2005).
7. Mercier, P. P., Lysaght, A. C., Bandyopadhyay, S., Chandrakasan, A. P. & Stankovic, K. M. Energy extraction from the biologic battery in the inner ear. *Nat. Biotechnol.* **30**, 1240–1243 (2012).
8. Pfenniger, A., Obrist, D., Stahel, A., Koch, V. M. & Vogel, R. Energy harvesting through arterial wall deformation: design considerations for a magneto-hydrodynamic generator. *Med. Biol. Eng. Comput.* **51**, 741–755 (2013).

9. Mitcheson, P. D., Yeatman, E. M., Rao, G. K., Holmes, A. & Green, T. C. Energy Harvesting From Human and Machine Motion for Wireless Electronic Devices. *Proc. IEEE* **96**, 1457–1486 (2008).
10. Dagdeviren, C. *et al.* Conformal piezoelectric energy harvesting and storage from motions of the heart, lung, and diaphragm. *Proc. Natl. Acad. Sci.* 201317233 (2014). doi:10.1073/pnas.1317233111
11. Cadei, A., Dionisi, A., Sardini, E. & Serpelloni, M. Kinetic and thermal energy harvesters for implantable medical devices and biomedical autonomous sensors. *Meas. Sci. Technol.* **25**, 012003 (2014).
12. Sue, C.-Y. & Tsai, N.-C. Human powered MEMS-based energy harvest devices. *Appl. Energy* **93**, 390–403 (2012).
13. Karami, M. A. & Inman, D. J. Powering pacemakers from heartbeat vibrations using linear and nonlinear energy harvesters. *Appl. Phys. Lett.* **100**, 042901 (2012).
14. Romero, E., Warrington, R. O. & Neuman, M. R. Energy scavenging sources for biomedical sensors. *Physiol. Meas.* **30**, R35 (2009).
15. Albano, F. *et al.* Design of an implantable power supply for an intraocular sensor, using POWER (power optimization for wireless energy requirements). *J. Power Sources* **170**, 216–224 (2007).
16. Khalil, I. S. M., Dijkslag, H. C., Abelman, L. & Misra, S. MagnetoSperm: A microrobot that navigates using weak magnetic fields. *Appl. Phys. Lett.* **104**, 223701 (2014).
17. Staples, M., Daniel, K., Cima, M. J. & Langer, R. Application of micro-and nano-electromechanical devices to drug delivery. *Pharm. Res.* **23**, 847–863 (2006).
18. Lavan, D. A., McGuire, T. & Langer, R. Small-scale systems for in vivo drug delivery. *Nat. Biotechnol.* **21**, 1184–1191 (2003).

19. Ferrari, M. Cancer nanotechnology: opportunities and challenges. *Nat. Rev. Cancer* **5**, 161–171 (2005).
20. Tao, S. L., Lubeley, M. W. & Desai, T. A. Bioadhesive poly (methyl methacrylate) microdevices for controlled drug delivery. *J. Controlled Release* **88**, 215–228 (2003).
21. Chapman, D. & Trybula, W. Meeting the challenges of oilfield exploration using intelligent micro and nano-scale sensors. in 1–6 (IEEE, 2012).
22. Seren, H. R., Zhao, X., Chen, C., Wang, C. & Zhang, X. Enabling a Microfluidic RFID Readout System via Miniaturization and Integration.
23. Guo, H. & Sun, Z. Channel and Energy Modeling for Self-Contained Wireless Sensor Networks in Oil Reservoirs. (2014).
24. Al Braik, M., Nasr, H. & Saghir, F. New wireless sensor network monitors water-injection wells off Abu Dhabi. *Oil Gas J.* **106**, (2008).
25. Gysling, D. L. & Bostick III, F. Changing paradigms in oil and gas reservoir monitoring-the introduction and commercialization of in-well optical sensing systems. in 43–46 (IEEE, 2002).
26. Lee, J.-H., Pidaparti, R. M., Atkinson, G. M. & Moorthy, R. S. Design of an Implantable Device for Ocular Drug Delivery. *J. Drug Deliv.* **2012**, e527516 (2012).
27. Liu, J., Agarwal, M., Varahramyan, K., Berney IV, E. S. & Hodo, W. D. Polymer-based microsensor for soil moisture measurement. *Sens. Actuators B Chem.* **129**, 599–604 (2008).
28. Waggoner, P. S. & Craighead, H. G. Micro- and nanomechanical sensors for environmental, chemical, and biological detection. *Lab. Chip* **7**, 1238–1255 (2007).

29. Amirtharajah, R. & Chandrakasan, A. Self-powered Low Power Signal Processing. in , *1997 Symposium on VLSI Circuits, 1997. Digest of Technical Papers* 25–26 (1997). doi:10.1109/VLSIC.1997.623784
30. Bayrashev, A., Robbins, W. P. & Ziaie, B. Low frequency wireless powering of microsystems using piezoelectric–magnetostrictive laminate composites. *Sens. Actuators Phys.* **114**, 244–249 (2004).
31. Beeby, S. *et al.* Micromachined silicon generator for harvesting power from vibrations. (2004).
32. Beeby, S. P., Tudor, M. J. & White, N. Energy harvesting vibration sources for microsystems applications. *Meas. Sci. Technol.* **17**, R175 (2006).
33. Cavallier, B. *et al.* Energy harvesting using vibrating structures excited by shock. in **2**, 943–945 (2005).
34. Caillat, T., Fleurial, J.-P., Snyder, G. & Borshchevsky, A. Development of high efficiency segmented thermoelectric uncouples. in 282–285 (IEEE, 2001).
35. Despesse, G. *et al.* Fabrication and characterization of high damping electrostatic micro devices for vibration energy scavenging. in 386–390 (2005).
36. El-Hami, M. *et al.* Design and fabrication of a new vibration-based electromechanical power generator. *Sens. Actuators Phys.* **92**, 335–342 (2001).
37. Fleurial, J.-P. *et al.* *Miniaturized thermoelectric power sources*. (SAE Technical Paper, 1999).
38. Glynn-Jones, P. & White, N. Self-powered systems: a review of energy sources. *Sens. Rev.* **21**, 91–98 (2001).
39. Meninger, S., Mur-Miranda, J. O., Amirtharajah, R., Chandrakasan, A. & Lang, J. H. Vibration-to-electric energy conversion. *IEEE Trans. Very Large Scale Integr. VLSI Syst.* **9**, 64–76 (2001).

40. Boisseau, S., Despesse, G. & Ahmed, B. in *Small-Scale Energy Harvesting* (ed. Lallart, M.) (InTech, 2012). at <<http://www.intechopen.com/books/small-scale-energy-harvesting/electrostatic-conversion-for-vibration-energy-harvesting>>
41. Tvedt, L. G. W., Nguyen, D. S. & Halvorsen, E. Nonlinear behavior of an electrostatic energy harvester under wide-and narrowband excitation. *Microelectromechanical Syst. J. Of* **19**, 305–316 (2010).
42. Torres, E. O. & Rincón-Mora, G. Electrostatic energy harvester and Li-ion charger circuit for micro-scale applications. in **1**, 65–69 (IEEE, 2006).
43. Le, C. P., Halvorsen, E., Søråsen, O. & Yeatman, E. M. Microscale electrostatic energy harvester using internal impacts. *J. Intell. Mater. Syst. Struct.* 1045389X12436739 (2012).
44. Halvorsen, E. *et al.* An electrostatic energy harvester with electret bias. in 1381–1384 (IEEE, 2009).
45. Beeby, S. P. & O'Donnell, T. in *Energy Harvesting Technologies* 129–161 (Springer, 2009).
46. Wiegele, T. G. Micro-turbo-generator design and fabrication: a preliminary study. in *Energy Conversion Engineering Conference, 1996. IECEC 96., Proceedings of the 31st Intersociety* **4**, 2308–2313 vol.4 (1996).
47. Holmes, A., Hong, G. & Pullen, K. R. Axial-flux permanent magnet machines for micropower generation. *J. Microelectromechanical Syst.* **14**, 54–62 (2005).
48. Peirs, J., Reynaerts, D. & Verplaetsen, F. A microturbine for electric power generation. *Sens. Actuators Phys.* **113**, 86–93 (2004).
49. Zwyssig, C., Kolar, J. W., Thaler, W. & Vohrer, M. Design of a 100 W, 500000 rpm permanent-magnet generator for mesoscale gas turbines. in *Industry Applications Conference, 2005. Fourtieth IAS Annual Meeting. Conference Record of the 2005* **1**, 253–260 Vol. 1 (2005).

50. Williams, C. B. & Yates, R. B. Analysis of a micro-electric generator for microsystems. *Sens. Actuators Phys.* **52**, 8–11 (1996).
51. Sodano, H. A. Comparison of Piezoelectric Energy Harvesting Devices for Recharging Batteries. *J. Intell. Mater. Syst. Struct.* **16**, 799–807 (2005).
52. Erturk, A. & Inman, D. J. *Piezoelectric energy harvesting*. (John Wiley & Sons, 2011).
53. Kim, H., Tadesse, Y. & Priya, S. in *Energy Harvesting Technologies* 3–39 (Springer, 2009).
54. Howells, C. A. Piezoelectric energy harvesting. *Energy Convers. Manag.* **50**, 1847–1850 (2009).
55. Sebald, G., Guyomar, D. & Agbossou, A. On thermoelectric and pyroelectric energy harvesting. *Smart Mater. Struct.* **18**, 125006 (2009).
56. IEEE Standard on Piezoelectricity. *ANSI/IEEE Std 176-1987 0_1–* (1988).
doi:10.1109/IEEESTD.1988.79638
57. Gandhi, M. V. *Smart materials and structures*. (Chapman & Hall, 1992).
58. Jaffe, B. *Piezoelectric Ceramics*. (Elsevier, 2012).
59. Yan, H. & Kim, E. S. Corrugated diaphragm for piezoelectric microphone. in **2**, 503–506 (IEEE, 1996).
60. Hillenbrand, J. & Sessler, G. M. High-sensitivity piezoelectric microphones based on stacked cellular polymer films (L). *J. Acoust. Soc. Am.* **116**, 3267–3270 (2004).
61. De Reus, R., Gulløv, J. O. & Scheeper, P. R. Fabrication and characterization of a piezoelectric accelerometer. *J. Micromechanics Microengineering* **9**, 123 (1999).
62. DeVoe, D. L. & Pisano, A. P. Surface micromachined piezoelectric accelerometers (PiXLs). *Microelectromechanical Syst. J. Of* **10**, 180–186 (2001).

63. Tressler, J. F., Alkoy, S. & Newnham, R. E. Piezoelectric sensors and sensor materials. *J. Electroceramics* **2**, 257–272 (1998).
64. Hwang, W.-S. & Park, H. C. Finite element modeling of piezoelectric sensors and actuators. *AIAA J.* **31**, 930–937 (1993).
65. Sodano, H. A., Inman, D. J. & Park, G. A review of power harvesting from vibration using piezoelectric materials. *Shock Vib. Dig.* **36**, 197–205 (2004).
66. Anton, S. R. & Sodano, H. A. A review of power harvesting using piezoelectric materials (2003–2006). *Smart Mater. Struct.* **16**, R1 (2007).
67. Polla, D. L. & Francis, L. F. Processing and Characterization of Piezoelectric Materials and Integration into Microelectromechanical Systems. *Annu. Rev. Mater. Sci.* **28**, 563–597 (1998).
68. Zhou, J., Xu, N. S. & Wang, Z. L. Dissolving Behavior and Stability of ZnO Wires in Biofluids: A Study on Biodegradability and Biocompatibility of ZnO Nanostructures. *Adv. Mater.* **18**, 2432–2435 (2006).
69. Qi, Y. *et al.* Piezoelectric Ribbons Printed onto Rubber for Flexible Energy Conversion. *Nano Lett.* **10**, 524–528 (2010).
70. Wang, X. *et al.* Matrix-Assisted Energy Conversion in Nanostructured Piezoelectric Arrays. *Nano Lett.* **10**, 4901–4907 (2010).
71. Sosa, H. & Khutoryansky, N. New developments concerning piezoelectric materials with defects. *Int. J. Solids Struct.* **33**, 3399–3414 (1996).
72. Li, S. & Mataga, P. A. Dynamic crack propagation in piezoelectric materials—Part I. Electrode solution. *J. Mech. Phys. Solids* **44**, 1799–1830 (1996).
73. Zhang, T.-Y. & Tong, P. Fracture mechanics for a mode III crack in a piezoelectric material. *Int. J. Solids Struct.* **33**, 343–359 (1996).

74. Qin, Q.-H. & Qin, Q. *Fracture mechanics of piezoelectric materials*. (WIT press Southampton, 2001).
75. Deeg, W. F. The analysis of dislocation, crack, and inclusion problems in piezoelectric solids. (1980).
76. Furukawa, T., Ishida, K. & Fukada, E. Piezoelectric properties in the composite systems of polymers and PZT ceramics. *J. Appl. Phys.* **50**, 4904–4912 (1979).
77. Wang, Z. L. Piezoelectric Nanogenerators Based on Zinc Oxide Nanowire Arrays. *Science* **312**, 242–246 (2006).
78. Gao, P., Ding, Y. & Wang, Z. Crystallographic orientation-aligned ZnO nanorods grown by a tin catalyst. *Nano Lett.* **3**, 1315–1320 (2003).
79. Wang, Z. L. ZnO nanowire and nanobelt platform for nanotechnology. *Mater. Sci. Eng. R Rep.* **64**, 33–71 (2009).
80. Gao, P. X. *et al.* Conversion of zinc oxide nanobelts into superlattice-structured nanohelices. *Science* **309**, 1700–1704 (2005).
81. Wang, Z. L. Zinc oxide nanostructures: growth, properties and applications. *J. Phys. Condens. Matter* **16**, R829 (2004).
82. Wang, Z. L. Nanostructures of zinc oxide. *Mater. Today* **7**, 26–33 (2004).
83. Wang, Z. L. Zinc oxide nanostructures: growth, properties and applications. *J. Phys. Condens. Matter* **16**, R829 (2004).
84. Yang, R., Qin, Y., Dai, L. & Wang, Z. L. Power generation with laterally packaged piezoelectric fine wires. *Nat. Nanotechnol.* **4**, 34–39 (2009).
85. Zhu, G., Yang, R., Wang, S. & Wang, Z. L. Flexible High-Output Nanogenerator Based on Lateral ZnO Nanowire Array. *Nano Lett.* **10**, 3151–3155 (2010).

86. Dong, X. *et al.* Hybrid structure of zinc oxide nanorods and three dimensional graphene foam for supercapacitor and electrochemical sensor applications. *RSC Adv.* **2**, 4364–4369 (2012).
87. Wang, Z. L. & Song, J. Piezoelectric Nanogenerators Based on Zinc Oxide Nanowire Arrays. *Science* **312**, 242–246 (2006).
88. Nishino, A. Capacitors: operating principles, current market and technical trends. *J. Power Sources* **60**, 137–147 (1996).
89. Conway, B. E. *Electrochemical supercapacitors: scientific fundamentals and technological applications*. (Plenum Press, 1999).
90. Nagaura, T. & Tozawa, K. Lithium ion rechargeable battery. *Prog. Batter. Sol. Cells* **9**, 209 (1990).
91. Wakihara, M. & Yamamoto, O. *Lithium Ion Batteries: Fundamentals and Performance*. (John Wiley & Sons, 2008).
92. Scrosati, B. Nanomaterials: Paper powers battery breakthrough. *Nat. Nanotechnol.* **2**, 598–599 (2007).
93. Zheng, H., Li, J., Song, X., Liu, G. & Battaglia, V. S. A comprehensive understanding of electrode thickness effects on the electrochemical performances of Li-ion battery cathodes. *Electrochimica Acta* **71**, 258–265 (2012).
94. Scrosati, B. Recent advances in lithium ion battery materials. *Electrochimica Acta* **45**, 2461–2466 (2000).
95. Van Schalkwijk, W. & Scrosati, B. *Advances in lithium-ion batteries*. (Springer, 2002).
96. Tarascon, J.-M. & Armand, M. Issues and challenges facing rechargeable lithium batteries. *Nature* **414**, 359–367 (2001).

97. Endo, M., Kim, C., Nishimura, K., Fujino, T. & Miyashita, K. Recent development of carbon materials for Li ion batteries. *Carbon* **38**, 183–197 (2000).
98. Kaskhedikar, N. A. & Maier, J. Lithium Storage in Carbon Nanostructures. *Adv. Mater.* **21**, 2664–2680 (2009).
99. Centi, G. & Perathoner, S. The Role of Nanostructure in Improving the Performance of Electrodes for Energy Storage and Conversion. *Eur. J. Inorg. Chem.* **2009**, 3851–3878 (2009).
100. Kim, M. G. & Cho, J. Reversible and High-Capacity Nanostructured Electrode Materials for Li-Ion Batteries. *Adv. Funct. Mater.* **19**, 1497–1514 (2009).
101. Su, D. S. & Schlögl, R. Nanostructured Carbon and Carbon Nanocomposites for Electrochemical Energy Storage Applications. *ChemSusChem* **3**, 136–168 (2010).
102. Dahn, J. R., Zheng, T., Liu, Y. & Xue, J. S. Mechanisms for Lithium Insertion in Carbonaceous Materials. *Science* **270**, 590–593 (1995).
103. Sato, K., Noguchi, M., Demachi, A., Oki, N. & Endo, M. A Mechanism of Lithium Storage in Disordered Carbons. *Science* **264**, 556–558 (1994).
104. Winter, M. & Besenhard, J. O. in *Lithium Ion Batteries* (eds. Wakihara, M. & Yamamoto, O.) 127–155 (Wiley-VCH Verlag GmbH, 1998). at <<http://onlinelibrary.wiley.com/doi/10.1002/9783527612000.ch6/summary>>
105. Yoo, E. *et al.* Large Reversible Li Storage of Graphene Nanosheet Families for Use in Rechargeable Lithium Ion Batteries. *Nano Lett.* **8**, 2277–2282 (2008).
106. Zheng, T., Xing, W. & Dahn, J. R. Carbons prepared from coals for anodes of lithium-ion cells. *Carbon* **34**, 1501–1507 (1996).
107. Balbuena, P. B. & Wang, Y. *Lithium-ion batteries solid-electrolyte interphase*. (Imperial College Press, 2004). at <<http://site.ebrary.com/id/10106582>>

108. Frackowiak, E., Gautier, S., Gaucher, H., Bonnamy, S. & Beguin, F.
Electrochemical storage of lithium in multiwalled carbon nanotubes. *Carbon* **37**, 61–69 (1999).
109. Claye, A. S., Fischer, J. E., Huffman, C. B., Rinzler, A. G. & Smalley, R. E. Solid-State Electrochemistry of the Li Single Wall Carbon Nanotube System. *J. Electrochem. Soc.* **147**, 2845–2852 (2000).
110. Lu, W. & Chung, D. D. L. Anodic performance of vapor-derived carbon filaments in lithium-ion secondary battery. *Carbon* **39**, 493–496 (2001).
111. Gao, B. *et al.* Electrochemical intercalation of single-walled carbon nanotubes with lithium. *Chem. Phys. Lett.* **307**, 153–157 (1999).
112. Wu, G. T. *et al.* Structure and Lithium Insertion Properties of Carbon Nanotubes. *J. Electrochem. Soc.* **146**, 1696–1701 (1999).
113. Kim, H. & Cho, J. Superior Lithium Electroactive Mesoporous Si@Carbon Core–Shell Nanowires for Lithium Battery Anode Material. *Nano Lett.* **8**, 3688–3691 (2008).
114. Hassoun, J., Derrien, G., Panero, S. & Scrosati, B. A Nanostructured Sn–C Composite Lithium Battery Electrode with Unique Stability and High Electrochemical Performance. *Adv. Mater.* **20**, 3169–3175 (2008).
115. Zhang, W.-M., Wu, X.-L., Hu, J.-S., Guo, Y.-G. & Wan, L.-J. Carbon Coated Fe₃O₄ Nanospindles as a Superior Anode Material for Lithium-Ion Batteries. *Adv. Funct. Mater.* **18**, 3941–3946 (2008).
116. Reddy, A. L. M., Shaijumon, M. M., Gowda, S. R. & Ajayan, P. M. Coaxial MnO₂/Carbon Nanotube Array Electrodes for High-Performance Lithium Batteries. *Nano Lett.* **9**, 1002–1006 (2009).
117. Simon, P. & Gogotsi, Y. Materials for electrochemical capacitors. *Nat. Mater.* **7**, 845–854 (2008).

118. Zhang, L. L. & Zhao, X. S. Carbon-based materials as supercapacitor electrodes. *Chem. Soc. Rev.* **38**, 2520–2531 (2009).
119. Aricò, A. S., Bruce, P., Scrosati, B., Tarascon, J.-M. & van Schalkwijk, W. Nanostructured materials for advanced energy conversion and storage devices. *Nat. Mater.* **4**, 366–377 (2005).
120. Stoller, M. D., Park, S., Zhu, Y., An, J. & Ruoff, R. S. Graphene-Based Ultracapacitors. *Nano Lett.* **8**, 3498–3502 (2008).
121. Geim, A. K. & Novoselov, K. S. The rise of graphene. *Nat. Mater.* **6**, 183–191 (2007).
122. Nguyen, P. & Berry, V. Graphene Interfaced with Biological Cells: Opportunities and Challenges. *J. Phys. Chem. Lett.* **3**, 1024–1029 (2012).
123. Zhu, Y. *et al.* Graphene and Graphene Oxide: Synthesis, Properties, and Applications. *Adv. Mater.* **22**, 3906–3924 (2010).
124. Bolotin, K. I. *et al.* Ultrahigh electron mobility in suspended graphene. *Solid State Commun.* **146**, 351–355 (2008).
125. Morozov, S. V. *et al.* Giant Intrinsic Carrier Mobilities in Graphene and Its Bilayer. *Phys. Rev. Lett.* **100**, 016602 (2008).
126. Lee, C., Wei, X., Kysar, J. W. & Hone, J. Measurement of the elastic properties and intrinsic strength of monolayer graphene. *Science* **321**, 385–388 (2008).
127. Balandin, A. A. *et al.* Superior thermal conductivity of single-layer graphene. *Nano Lett.* **8**, 902–907 (2008).
128. Cai, W., Zhu, Y., Li, X., Piner, R. D. & Ruoff, R. S. Large area few-layer graphene/graphite films as transparent thin conducting electrodes. *Appl. Phys. Lett.* **95**, 123115 (2009).

129. Gao, W., Alemany, L. B., Ci, L. & Ajayan, P. M. New insights into the structure and reduction of graphite oxide. *Nat Chem* **1**, 403–408 (2009).
130. Chabot, V., Kim, B., Sloper, B., Tzoganakis, C. & Yu, A. High yield production and purification of few layer graphene by Gum Arabic assisted physical sonication. *Sci. Rep.* **3**, (2013).
131. Hernandez, Y. *et al.* High-yield production of graphene by liquid-phase exfoliation of graphite. *Nat. Nanotechnol.* **3**, 563–568 (2008).
132. Kim, K. S. *et al.* Large-scale pattern growth of graphene films for stretchable transparent electrodes. *Nature* **457**, 706–710 (2009).
133. Li, X. *et al.* Large-Area Synthesis of High-Quality and Uniform Graphene Films on Copper Foils. *Science* **324**, 1312–1314 (2009).
134. Li, X. *et al.* Transfer of Large-Area Graphene Films for High-Performance Transparent Conductive Electrodes. *Nano Lett.* **9**, 4359–4363 (2009).
135. Lin, Y.-M. *et al.* Operation of Graphene Transistors at Gigahertz Frequencies. *Nano Lett.* **9**, 422–426 (2009).
136. Bae, S. *et al.* Roll-to-roll production of 30-inch graphene films for transparent electrodes. *Nat. Nanotechnol.* **5**, 574–578 (2010).
137. Samsung Electronics Discovers Groundbreaking Method to Commercialize New Material for Electronics | Samsung Electronics Official Blog: Samsung Tomorrow. at <<http://global.samsungtomorrow.com/?p=35576>>
138. Raman, R. K. S. *et al.* Protecting copper from electrochemical degradation by graphene coating. *Carbon* **50**, 4040–4045 (2012).
139. Rafiee, J. *et al.* Wetting transparency of graphene. *Nat. Mater.* **11**, 217–222 (2012).

140. Hou, J., Shao, Y., Ellis, M. W., Moore, R. B. & Yi, B. Graphene-based electrochemical energy conversion and storage: fuel cells, supercapacitors and lithium ion batteries. *Phys. Chem. Chem. Phys.* **13**, 15384–15402 (2011).
141. R W Whatmore. Pyroelectric devices and materials. *Rep. Prog. Phys.* **49**, 1335 (1986).
142. Wang, X., Song, J., Liu, J. & Wang, Z. L. Direct-Current Nanogenerator Driven by Ultrasonic Waves. *Science* **316**, 102 –105 (2007).
143. Cha, S. N. *et al.* Sound-Driven Piezoelectric Nanowire-Based Nanogenerators. *Adv. Mater.* **22**, 4726–4730 (2010).
144. Qin, Y., Wang, X. & Wang, Z. L. Microfibre–nanowire hybrid structure for energy scavenging. *Nature* **451**, 809–813 (2008).
145. Liu, J., Fei, P., Zhou, J., Tummala, R. & Wang, Z. L. Toward high output-power nanogenerator. *Appl. Phys. Lett.* **92**, 173105 (2008).
146. Klemm, D., Heublein, B., Fink, H.-P. & Bohn, A. Cellulose: Fascinating Biopolymer and Sustainable Raw Material. *Angew. Chem. Int. Ed.* **44**, 3358–3393 (2005).
147. Fukada, E. History and recent progress in piezoelectric polymers. *Ultrason. Ferroelectr. Freq. Control IEEE Trans. On* **47**, 1277–1290 (2000).
148. Kim, J., Yun, S. & Ounaies, Z. Discovery of Cellulose as a Smart Material. *Macromolecules* **39**, 4202–4206 (2006).
149. Pushparaj, V. L. *et al.* Flexible energy storage devices based on nanocomposite paper. *Proc. Natl. Acad. Sci.* **104**, 13574 –13577 (2007).
150. Gullapalli, H. *et al.* Flexible Piezoelectric ZnO–Paper Nanocomposite Strain Sensor. *small* **6**, 1641–1646 (2010).

151. Kumar, A. *et al.* Flexible ZnO-Cellulose Nanocomposite for Multisource Energy Conversion. *Small* **7**, 2173–2178 (2011).
152. Yu, H., Zhang, Z., Han, M., Hao, X. & Zhu, F. A general low-temperature route for large-scale fabrication of highly oriented ZnO nanorod/nanotube arrays. *J. Am. Chem. Soc.* **127**, 2378–2379 (2005).
153. Lyu, S. C. *et al.* Low temperature growth and photoluminescence of well-aligned zinc oxide nanowires. *Chem. Phys. Lett.* **363**, 134–138 (2002).
154. Saito, N. *et al.* Low-temperature fabrication of light-emitting zinc oxide micropatterns using self-assembled monolayers. *Adv. Mater.* **14**, 418–421 (2002).
155. Lee, C. *et al.* Field emission from well-aligned zinc oxide nanowires grown at low temperature. *Appl. Phys. Lett.* **81**, 3648–3650 (2002).
156. Kamalasanan, M. & Chandra, S. Sol-gel synthesis of ZnO thin films. *Thin Solid Films* **288**, 112–115 (1996).
157. Ohyama, M., Kouzuka, H. & Yoko, T. Sol-gel preparation of ZnO films with extremely preferred orientation along (002) plane from zinc acetate solution. *Thin Solid Films* **306**, 78–85 (1997).
158. Cao, G. *Synthesis, Properties and Applications*. (World Scientific, 2004).
159. Coppa, B. J., Davis, R. F. & Nemanich, R. J. Gold Schottky contacts on oxygen plasma-treated, n-type ZnO(0001 #xaf;). *Appl. Phys. Lett.* **82**, 400–402 (2003).
160. Zaleski Jr., T. E. & Schmidt, S. R. Method and apparatus for monitoring and recording of operating conditions of a downhole drill bit during drilling operations.
161. Schlutz, R. L., De Jesus, O. & Osborne, A. J. Differential sensor measurement method and apparatus to detect a drill bit failure and signal surface operator.
162. Kwon, S.-Y. *et al.* Growth of Semiconducting Graphene on Palladium. *Nano Lett.* **9**, 3985–3990 (2009).

163. Sutter, P. W., Flege, J.-I. & Sutter, E. A. Epitaxial graphene on ruthenium. *Nat. Mater.* **7**, 406–411 (2008).
164. Coraux, J., N'Diaye, A. T., Busse, C. & Michely, T. Structural Coherency of Graphene on Ir(111). *Nano Lett.* **8**, 565–570 (2008).
165. Mattevi, C., Kim, H. & Chhowalla, M. A review of chemical vapour deposition of graphene on copper. *J. Mater. Chem.* **21**, 3324 (2011).
166. Dupuis, A.-C. The catalyst in the CCVD of carbon nanotubes—a review. *Prog. Mater. Sci.* **50**, 929–961 (2005).
167. Homma, Y. *et al.* Role of transition metal catalysts in single-walled carbon nanotube growth in chemical vapor deposition. *J. Phys. Chem. B* **107**, 12161–12164 (2003).
168. Yazyev, O. V. & Pasquarello, A. Effect of metal elements in catalytic growth of carbon nanotubes. *Phys. Rev. Lett.* **100**, 156102 (2008).
169. Pierson, H. O. *Handbook of chemical vapor deposition*. (Noyes Publications, 1999).
170. López, G. A. & Mittemeijer, E. J. The solubility of C in solid Cu. *Scr. Mater.* **51**, 1–5 (2004).
171. Oshima, C. & Nagashima, A. Ultra-thin epitaxial films of graphite and hexagonal boron nitride on solid surfaces. *J. Phys. Condens. Matter* **9**, 1 (1997).
172. Li, X., Cai, W., Colombo, L. & Ruoff, R. S. Evolution of Graphene Growth on Ni and Cu by Carbon Isotope Labeling. *Nano Lett.* **9**, 4268–4272 (2009).
173. Srivastava, A. *et al.* Novel Liquid Precursor-Based Facile Synthesis of Large-Area Continuous, Single, and Few-Layer Graphene Films. *Chem. Mater.* **22**, 3457–3461 (2010).
174. Sun, Z. *et al.* Growth of graphene from solid carbon sources. *Nature* **468**, 549–552 (2010).

175. Reddy, A. L. M. *et al.* Synthesis Of Nitrogen-Doped Graphene Films For Lithium Battery Application. *Acs Nano* **4**, 6337–6342 (2010).
176. Gullapalli, H., Reddy, A. L. M., Kilpatrick, S., Dubey, M. & Ajayan, P. M. Graphene Growth via Carburization of Stainless Steel and Application in Energy Storage. *Small* (2011).
177. Kang, J., Shin, D., Bae, S. & Hong, B. H. Graphene transfer: key for applications. *Nanoscale* **4**, 5527–5537 (2012).
178. Ferrari, A. C. *et al.* Raman Spectrum of Graphene and Graphene Layers. *Phys. Rev. Lett.* **97**, (2006).
179. Shirley, D. High-Resolution X-Ray Photoemission Spectrum of the Valence Bands of Gold. *Phys. Rev. B* **5**, 4709–4714 (1972).
180. *Handbook of comparative world steel standards.* (ASTM International, 2004).
181. Surm, H., Kessler, O., Hoffmann, F. & Mayr, P. Carburized, CVD-Coated, and Gas Quenched Steels: Carbon Profile, Microstructure, and Hardness. *Adv. Eng. Mater.* **2**, 814–818 (2000).
182. Rosenberg, S. J. & Irish, C. R. Solubility of carbon in 18-percent-chromium 10-percent-nickel austenite. *J. Res. Natl. Bur. Stand.* **48**, 40 (1952).
183. Aborn, R. H. & Bain, E. C. The Nature of the Nickel-Chromium Rustless Steels. *Trans. American Soc. Steel Treat.* **18**, 837–73 (1930).
184. Krivobok, V. N. & Grossman, M. A. Influence of Nickel on the Chromium- Iron-Carbon Constitutional Diagram. *Trans. American Soc. Steel Treat.* **18**, 808 (1930).
185. Green, O. V. Discussion. *Trans. American Soc. Steel Treat.* **18**, 877 (1930).
186. Manos, D. M. & Flamm, D. L. *Plasma Etching: An Introduction.* (Elsevier, 1989).

187. Dahn, J. R., Zheng, T., Liu, Y. & Xue, J. S. Mechanisms for Lithium Insertion in Carbonaceous Materials. *Science* **270**, 590–593 (1995).
188. Kumar, A. *et al.* Direct synthesis of lithium-intercalated graphene for electrochemical energy storage application. *ACS Nano* **5**, 4345–4349 (2011).
189. Park, J. H., Ko, J. M. & Ok Park, O. Carbon Nanotube/RuO₂ Nanocomposite Electrodes for Supercapacitors. *J. Electrochem. Soc.* **150**, A864 (2003).
190. Imanishi, N., Takeda, Y. & Yamamoto, O. in *Lithium Ion Batteries* (eds. Wakihara, M. & Yamamoto, O.) 98–126 (Wiley-VCH Verlag GmbH, 1998). at <http://onlinelibrary.wiley.com/doi/10.1002/9783527612000.ch5/summary>
191. Park, M., Zhang, X., Chung, M., Less, G. B. & Sastry, A. M. A review of conduction phenomena in Li-ion batteries. *J. Power Sources* **195**, 7904–7929 (2010).
192. Li, Y. F., Zhou, Z. & Wang, L. B. CN_x nanotubes with pyridinelike structures: p-type semiconductors and Li storage materials. *J. Chem. Phys.* **129**, 104703 (2008).
193. Long, J. W., Dunn, B., Rolison, D. R. & White, H. S. Three-Dimensional Battery Architectures. *Chem. Rev.* **104**, 4463–4492 (2004).
194. Chan, C. K. *et al.* High-performance lithium battery anodes using silicon nanowires. *Nat. Nanotechnol.* **3**, 31–35 (2008).
195. Aurbach, D. & Ein-Eli, Y. The Study of Li-Graphite Intercalation Processes in Several Electrolyte Systems Using In Situ X-Ray Diffraction. *J. Electrochem. Soc.* **142**, 1746–1752 (1995).
196. Li, C.-L., Sun, Q., Jiang, G.-Y., Fu, Z.-W. & Wang, B.-M. Electrochemistry and Morphology Evolution of Carbon Micro-net Films for Rechargeable Lithium Ion Batteries. *J. Phys. Chem. C* **112**, 13782–13788 (2008).

197. Gowda, S. R. *et al.* Three-Dimensionally Engineered Porous Silicon Electrodes for Li Ion Batteries. *Nano Lett.* **12**, 6060–6065 (2012).
198. Borges, R. S. *et al.* Supercapacitor Operating At 200 Degrees Celsius. *Sci. Rep.* **3**, (2013).
199. Stoller, M. D. & Ruoff, R. S. Best practice methods for determining an electrode material's performance for ultracapacitors. *Energy Environ. Sci.* **3**, 1294 (2010).
200. Wu, Z.-S., Parvez, K., Feng, X. & Müllen, K. Graphene-based in-plane micro-supercapacitors with high power and energy densities. *Nat. Commun.* **4**, (2013).